

University of Louisville

ThinkIR: The University of Louisville's Institutional Repository

Electronic Theses and Dissertations

8-2006

Analysis and experiments on flow-induced hemolysis.

Yangsheng Chen 1969-
University of Louisville

Follow this and additional works at: <https://ir.library.louisville.edu/etd>

Recommended Citation

Chen, Yangsheng 1969-, "Analysis and experiments on flow-induced hemolysis." (2006). *Electronic Theses and Dissertations*. Paper 236.
<https://doi.org/10.18297/etd/236>

This Doctoral Dissertation is brought to you for free and open access by ThinkIR: The University of Louisville's Institutional Repository. It has been accepted for inclusion in Electronic Theses and Dissertations by an authorized administrator of ThinkIR: The University of Louisville's Institutional Repository. This title appears here courtesy of the author, who has retained all other copyrights. For more information, please contact thinkir@louisville.edu.

ANALYSIS AND EXPERIMENTS ON FLOW-INDUCED HEMOLYSIS

By

Yangsheng Chen

B.S., Mech. Eng., University of Science and Technology of China, 1992

M.Eng., Mech. Eng., China Aerodynamics Research and Development Center, 1995

M.S., Computer Science, University of Louisville, 2003

A Dissertation

Submitted to the Faculty of the

Graduate School of the University of Louisville

In Partial Fulfillment of the Requirements

For the Degree of

Doctor of Philosophy

Department of Mechanical Engineering

University of Louisville

Louisville, Kentucky

August, 2006

Copyright 2006 by Yangsheng Chen

All rights reserved

ANALYSIS AND EXPERIMENTS ON FLOW-INDUCED HEMOLYSIS

By

Yangsheng Chen

A Dissertation Approved on

July 19, 2006

by the following Dissertation Committee:

**Dr. M. Keith Sharp
Dissertation Director**

Dr. Timothy Edward Dowling

Dr. Ellen G. Brehob

Dr. W. Geoffrey Coburn

Dr. George Pantalos

Dr. Steven C. Koenig

Dr. R. Eric Berson

ACKNOWLEDGMENTS

First and foremost, I would like to thank my mother Xiurong Xiong and my father Baohua Chen, for all of their sacrifices and support. They raised me under hard situations. Their love, support and patience made this possible. I also want to thank my wife Dengzhi Wang for her love, support, encouragement, and lots of discussions (Both of us worked in the field of biomechanics). I want to devote this paper to my newborn baby daughter Amy W. Chen.

I am sincerely grateful to the Grosscurth Fellowship, Research Assistantship provided by the Speed Scientific School and Department of Mechanical Engineering.

I am grateful to my advisor Dr. M. Keith Sharp for the opportunities, financial aid, encouragement, and leadership he has provided over the years.

There are a number of people to whom I owe appreciation for helping with the day to day struggles. John C. Jones gave me lots of help in machine shop, control system design, and computer systems. Dr Robert S. Keynton generously lent me their digital camera for more than two years. Thomas J Roussel helped me adjust the camera system. Scott Cambron fabricated the flow chamber for me. Dr Robert W. Cohn helped me adjust laser system, etc. I also want to thank the staff of the Department of Mechanical Engineering for all their help.

ABSTRACT

ANALYSIS AND EXPERIMENTS ON FLOW-INDUCED HEMOLYSIS

Yangsheng Chen

July 19, 2006

Hemolysis (red cells lysis) caused by fluid stresses in flows within hypodermic needles, blood pumps, artificial hearts and other cardiovascular devices, is one of the major concerns during the design and use of cardiovascular or blood-processing extracorporeal devices. A non-invasive experimental method which does not interfere directly with red blood cells was designed to investigate the red cells' deformations in response to a range of flow conditions. The designed flow chamber and pump system provided a controlled two-dimensional Poiseuille flow with average velocity of up to 4 m/s and a range of fluid stresses up to 5000 dyn/cm². The dimension of deformed cells and positions was measured to obtain the aspect ratio of red cells under stress from images captured by the microscope-laser-camera system. A strain-based blood damage model from Rand's viscoelastic model was built to predict cell strain. The empirical coefficients in the blood damage model were calibrated by the measurements from the experiments.

Flow-induced hemolysis in the blood flow through hypodermic needles was investigated. The flow-induced hemolysis of the needles may be reduced by a modified design of the entrance geometry of the needle. Three groups of 16 gauge needles were compared: one standard group with sharp entrance, another with beveled entrance and a

third with rounded entrance. The CFD analysis combined with the strain-based blood damage model, Heuser *et al.* model and Giersiepen *et al.* model respectively was used to analyze the flow-induced hemolysis of the three needles. The predicted results were compared to the experimental results, which showed the rounded entrance reduced hemolysis by 34%, but the beveled entrance increased hemolysis by 38%. The strain-based blood damage model predicted the reduced hemolysis by 7.4% in rounded needle and the increased hemolysis by 13% in beveled needle. Both Heuser *et al.* model and Giersiepen *et al.* model predicted increased hemolysis in rounded needle.

TABLE OF CONTENTS

	PAGE
ACKNOWLEDGMENTS	iii
ABSTRACT	iv
LIST OF TABLES	viii
LIST OF FIGURES	ix
CHAPTER	
I. INTRODUCTION	1
II. LITERATURE REVIEW	
Application Background	5
Physiological Parameters of Human RBCs	9
Mechanical Properties of Erythrocyte Membrane	11
Complexity of RBC's Deforming Movement in Blood Flow	15
Mechanism of Hemolysis	19
III. EXPERIMENTAL INVESTIGATION OF FLOW-INDUCED HEMOLYSIS AND A STRAIN-BASED BLOOD DAMAGE MODEL	
Purpose of Investigation	24
Experimental Methods	31
Blood Damage Model	44
Results and Analysis	60
Discussion	69
IV. HEMOLYSIS PREDICTION IN THE BLOOD FLOW THROUGH HYPODERMIC NEEDLES	
Purpose of Investigation	72
CFD Simulations	77
Blood Damage Models	91
Results and Analysis	95
Discussion	99
V. SUMMARY AND CONCLUSIONS	104
REFERENCES	107
APPENDICES	
APPENDIX A - Ellipsoid Calculation Formula	112
APPENDIX B - NOMENCLATURE	113

APPENDIX C – Drawing of Flow Chamber	114
APPENDIX D – List of Programs	115
CURRICULUM VITAE	139

LIST OF TABLES

TABLE		PAGE
2.1	Membrane parameters for a typical red blood cell	11
2.2	The viscosity of red cell cytosol	11
3.1	The critical shear stress under various flow conditions	27
3.2	Possible deformation patterns of red cell	46
3.3	Aspect ratio a/b versus area strain	58
3.4	Experimental specifications	63
4.1	Average velocity through the needles	80
4.2	Index of hemolysis of experiments and models	96
4.3	Number of hemolytic streamlines for Strain-based model	96

LIST OF FIGURES

FIGURE	PAGE
2.1 Schematic of the anatomical placements of the electromechanical TAH	6
2.2 An electromechanical TAH	6
2.3 Human red blood cells fixed while immersed in shear flow in concentric cylinder viscometer	8
2.4 Scanning electron micrograph of human red blood cells	10
2.5 Schematic of erythrocyte membrane	12
2.6 Symbolic representation of red cell membrane as a solid-liquid composite	13
2.7 Schematic illustration of the deformation of a rectangle membrane material element in the principal axis system	13
2.8 Images of the deformation of RBC at several different shear rate	16
2.9 Tank-treading motion of RBC membrane at time interval of 20ms	17
2.10 2D plot of simulation of flow-induced deformation of red blood cells	18
2.11 3D plot of simulation of flow-induced deformation of red blood cells	19
2.12 Cell lysis mechanism	20
2.13 Rand's mechanical model of the cell membrane	22
3.1 Cone/Plate	30
3.2 Micropipette Experiment	30
3.3 Schematic of experimental system	31
3.4 Flow chamber	33
3.5 Microscope and digital camera	33
3.6 Syringe pump	33
3.7 Schematic diagram of the channel flow	35
3.8 Nd-YAG Laser	37
3.9 Optical fiber	37
3.10 Reduce laser speckle with optical fiber	38

3.11	User interface of QCapture Pro	41
3.12	Controller box with relay	41
3.13	Schematic of timing sequence	42
3.14	Geometry of the prolate ellipsoidal model of the red cell	45
3.15	Free body diagram of the force equilibrium in the x direction	47
3.16	Free body diagram for the force equilibrium in the z direction	49
3.17	Membrane tensions of red cell from numerical simulation under simple shear flow	50
3.18	Schematic of stages of red cell's deformation	51
3.19	Aspect ratio a/b versus area strain	58
3.20	Picture of moving cells and scale	61
3.21	Orientations of stretched cells	62
3.22	3D plot of aspect ratio versus shear stress and exposure time	64
3.23	Comparison of predicted and measured aspect ratio versus shear stress with three optimized parameter values fit to cell image data	66
3.24	Comparison of predicted and measured aspect ratio versus exposure time with three optimized parameter values fit to cell image data	66
3.25	Comparison of predicted and measured aspect ratio versus shear stress with one parameter value fit to a hemolysis threshold	67
3.26	Comparison of predicted and measured aspect ratio versus shear stress with one parameter value fit to a hemolysis threshold	67
3.27	Comparison of hemolysis threshold models to data	68
4.1	CAD geometry of standard needle	77
4.2	CAD geometries of the tips of 3 needles	78
4.3	Schematic of the initial computation domain for the standard needle	79
4.4	Schematic of part of the computational grid for standard needle	81
4.5	The contour plots of velocity magnitude (m/s) on the symmetric mid-plane	83
4.6	The contour plots of τ_s (dyn/cm ²) on the symmetric mid-plane	84
4.7	The contour plots of velocity magnitude (m/s) on cross-section plane	85
4.8	The contour plots of τ_s (dyn/cm ²) on cross-section plane	86

4.9	Schematic of the sample plane	87
4.10	Schematic of sample points on half plane and the streamlines	88
4.11	Time history of τ_s along an example streamline, without smoothing	89
4.12	Time history of τ_s along an example streamline, with smoothing	90
4.13	The Schematic of the cell breaking into small pieces	97
4.14	Index of hemolysis of the needles	99
4.15	Scatter plots of IH_i on cross-section plane from strain-based model	101
4.16	Time history of τ_s along streamline with lysis	102

CHAPTER I

INTRODUCTION

Hemolysis is defined as the release of hemoglobin from red cells into plasma due to the damage of the cells' membranes. Lokhandwalla & Sturtevant [2001] categorized the factors of cell lysis into thermal/radiation, mechanical, and chemical. The membrane rupture of human red cells can be caused by fluid stresses in flows within hypodermic needles, blood pumps, artificial hearts and other cardiovascular devices. This type of rupture belongs to the mechanical lysis category. Hemolysis can interfere with common blood tests and cause pain and discomfort during dialysis sessions. Hemolysis is also a central design issue for blood pumps, artificial hearts and other cardiovascular devices. Developers of cardiovascular devices often expend considerable time and effort in the testing of their prototypes to avoid such problems because there isn't currently sufficient understanding of how flow-induced cell damage occurs. Therefore, it is difficult to accurately predict hemolysis.

The overall purpose of this work is to develop a hemolysis prediction model that can be used in CFD analysis of cardiovascular devices. The first tasks, which comprise this PhD project, are the initial formulation of a model, development of an experimental method for investigating flow-induced deformation of red cells by which the model is calibrated, and evaluation of the model by application to flows in hypodermic needles.

This project consists of an experimental investigation of the deformation of red cells under fluid stress including a strain-based blood damage model and an analysis of hemolysis of human blood flow through three kinds of needles. The paper is organized with the following structure:

Chapter II is a literature review. It introduces the significant findings from the research about red cell damage in artificial devices. The characteristics of red blood cells are listed briefly, which include the distribution of dimensions, the mechanical parameters of membranes and the viscosity of red cell cytosol. The membrane structure of red cells linked to the mechanical characteristic of membranes and a mechanical model of membranes, developed by Evans, *et al.*, is introduced with more details. The research on the deforming movement of red cells in flow is introduced to increase the understanding of the behaviors of red cells. The progress of research on the mechanism of hemolysis is presented, which has special interest to the research work in this paper.

In Chapter III, a non-invasive experimental system is designed to measure cell deformation in response to a range of flow conditions. The measurements are used to develop a constitutive model correlating cell deformation and damage to fluid stresses. The experimental system created an observable, controlled two-dimensional Poiseuille flow under a microscope. Cells in the flow chamber moved at velocities of up to 4 m/s and experienced fluid stresses of up to 5000 dyn/cm². An Nd-YAG laser was used to provide pulsed illumination, and a digital camera was used to collect the images. The speckle effect of the laser pulse was eliminated with an optical fiber. The captured pictures of the deformed moving red cells were measured to obtain the aspect ratio and distance from the wall of each cell, which, along with the bulk flow rate in the channel,

allowed determination of the fluid stresses exerted on each cell. To construct a strain-based blood damage model to predict cell strain, equilibrium equations were developed to relate fluid stresses to cell membrane tension and viscoelastic membrane stress/strain response was used. Measurements of aspect ratio as a function of shear stress and duration of shear for blood samples from seven different donors were used to calibrate the cell deformation model. Hemolysis prediction was incorporated into the model with a threshold value of the strain at which cell rupture occurs. Multiple regression with previous hemolysis measurements for several flow conditions was used to optimize the empirical coefficients in the blood damage model.

In Chapter IV, flow-induced hemolysis in 16 gauge needles was investigated with CFD and compared to experimental results. Two modified needles with beveled and rounded entrances, respectively, were compared to a standard needle with sharp entrance to determine the least hemolytic design. Solid models geometries of the three needles were imported into GAMBIT to establish flow domain boundaries and computational grids were generated. Pressure boundary conditions approximated those of vacuum sample collection tubes. After simulation of the steady state velocity field by FLUENT, a grid of stream-tubes filling the flow cross section were defined and the time history of scalar stress along streamlines central to each streamtube were calculated. The strain-based cell membrane failure model developed in Chapter III and two empirical blood damage models were applied to predict hemolysis on each streamline. The total hemolysis was calculated by weighting the result along each streamline by the flow rate through each streamtube. The performance of each model was compared to the experiments, which showed that the rounded entrance produced significantly less

hemolysis than the standard, while the beveled entrance produced more. Among three models of the strained-based model, the Giersiepen *et al.* model, and Heuser, *et al.* model, the computational results showed that only the strain-based blood damage model could predict the correct trend of hemolysis of the needles.

Chapter V is a summary of the analysis and experiments and the conclusions.

CHAPTER II

LITERATURE REVIEW

Application Background

Prosthetic devices have been widely used in many circulatory support situations, such as ventricular assist devices (VAD), total artificial hearts (TAH), blood pumps, prosthetic valves, blood oxygenators, cardiopulmonary bypass pumps, etc. In the USA approximately 40,000 patients require heart transplantation each year. However there are only 2,000 donor hearts available annually [Piccione 2001]. Without heart transplantation, the lives of patients with heart disease depend on VAD devices. VAD devices can be used as a medium-term bridge to transplantation. One of the anatomical placements of the electromechanical TAH and VAD and associated components [Nobuhisa, *et al.* 1999] is shown in Fig. 2.1. Fig. 2.2 [Nobuhisa, *et al.* 1999] shows a compact size electromechanical TAH and VAD. These devices are featured with magnetically suspended no-contact bearings and will be more durable and help patients feel more comfortable.

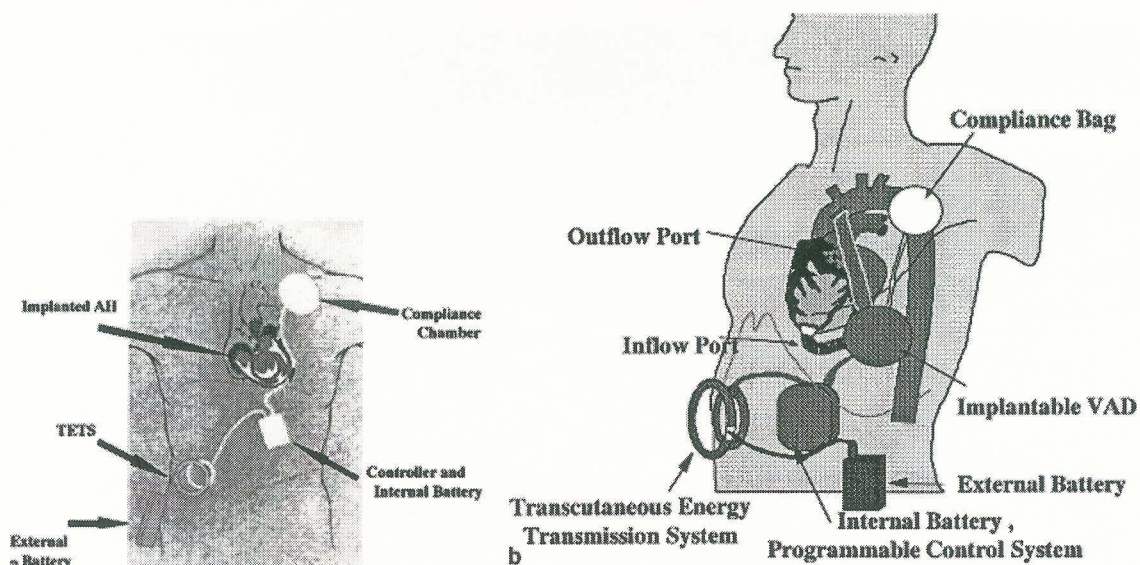


FIGURE 2.1 Schematic of the anatomical placements of the electromechanical TAH (a) and the VAD (b) and associated components [Nobuhisa, *et al.* 1999]

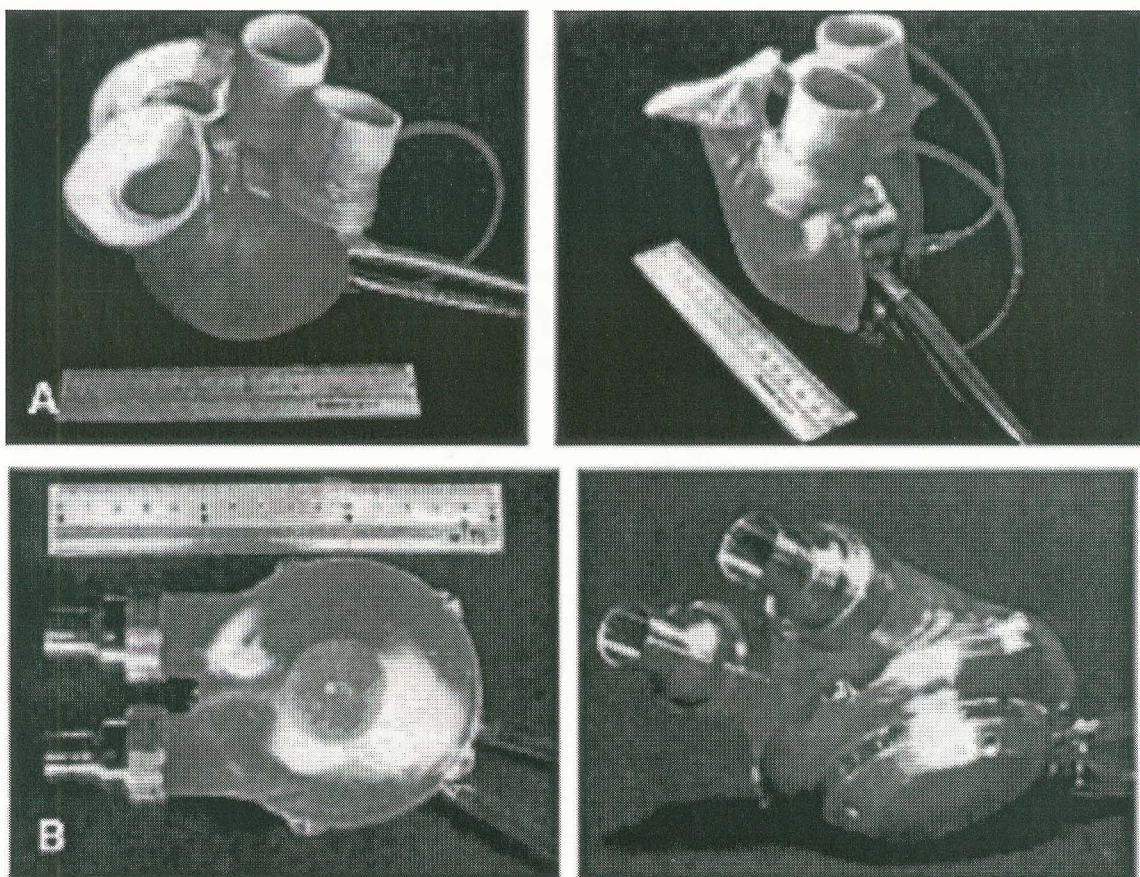


FIGURE 2.2 An electromechanical TAH (A) and a VAD (B) [Nobuhisa, *et al.* 1999]

Because the working fluid in VAD and TAH devices is blood from the human body, it is a huge challenge to design VAD and TAH devices that meet all the physical and physiological requirements. Two of the major concerns during the design and use of cardiovascular or blood-processing extracorporeal devices are blood damage (hemolysis) and blood aggregation (thrombosis). The blood damage caused by artificial devices is mainly from the flow-induced trauma to red cells (Red Blood Cells, i.e. RBCs). A major deterrent in the continuous usage of the TAH device in a recipient is severe hemolysis [Yukio, *et al.* 2003]. This blood damage must be taken into consideration especially for compact VAD & TAH devices, because the compact size will result in higher flow speed and higher fluid stress to keep the same flow rate through the devices. The blood trauma caused by these artificial devices may exceed the haemostatic mechanism of the human body, and result in abnormal physiological conditions. One of the results of the red cells damage induced in blood flow is the release of hemoglobin into plasma. High concentrations of plasma free hemoglobin (PFH) are toxic, and can result in renal dysfunction and other organ failure.

In Figure 2.3, the broken RBCs are shown under shear flow in a concentric cylinder viscometer [Sutera & Mehrjardi 1975]. In Figure 2.3a, the red cells are a bulbous shape at the shear stress of 100 dyn/cm². Figure 2.3b shows the cells fixed at 2,000 dyn/cm² shear stress. As the stress increased, the ellipsoidal shape became predominant. Figure 2.3c is taken at 3,500 dyn/cm², and it can be seen that there are some fragments. In Figure 2.3d, which is at 4,500 dyn/cm², more and smaller fragments are evident.

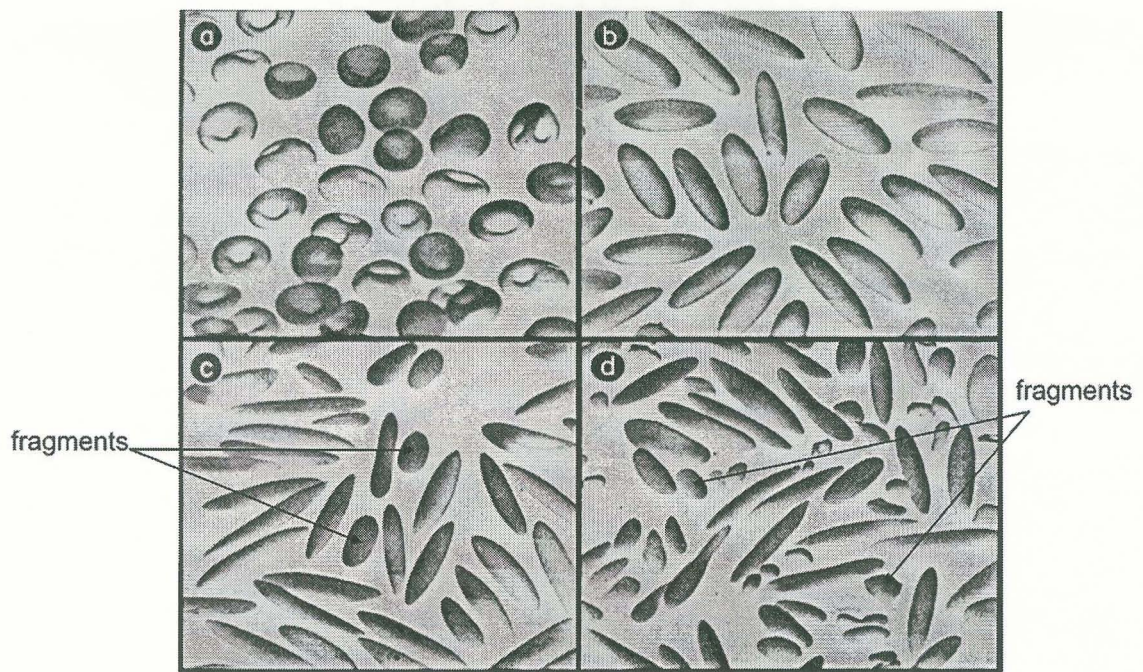


FIGURE 2.3 Human red blood cells fixed while immersed in shear flow in concentric cylinder viscometer. Applied shearing stress: a. 100, b. 2,000, c. 3,500, d. 4,500 dyn/cm² (4 min) [Sutera & Mehrjardi 1975]

Hemolysis also results in a shortened red blood cell lifetime in the circulation. Therefore, hemolysis is an important and widely measured indicator of device performance and optimum design for the evaluation of artificial devices such as artificial hearts [Westaby, *et al.* 1998], centrifugal blood pumps [Ahmed, *et al.* 1999], phlebotomy cannulae [Sharp 1998], and shock wave lithotripsy [Lokhandwalla & Sturtevant 2001]. Many in vitro hemolysis tests are required for the evaluation of a design.

During the design of an artificial device, an experimental optimum design is often obtained on a trial-and-error basis. This approach is extremely costly both in materials and time. Therefore, more understanding on the mechanism of damage of erythrocyte will help guide the optimum design of artificial devices and reduce the cost.

Physiological Parameters of Human RBCs

Red cells are suspended in human blood flow. The following values of human blood are from Perry and Gertrude [1987].

Average volume: 5000 mL

Average red cell volume: 2000 mL

Hematocrit: 46% (male), 41% (female)

Red cell count ($\times 10^6/\mu\text{L}$ blood): 5.1 (male), 4.5 (female)

Reticulocyte count (0.5 to 1.5 per 100 RBCs): > 4% is abnormal

Hemoglobin: 15 g/100mL, 750 g in circulating red cells,

2.5 mg free hemoglobin in 100 mL normal plasma

A normal human red cell looks like a biconcave disk at rest. At 300 mosmol (unit of osmolarity), the solution is isotonic (net flow of liquid into the RBC equals net flow out). Its thickness is $1.4 \mu\text{m} \sim 2.8 \mu\text{m}$ from the center to the rim [Richard, *et al.* 2002]. Its mean surface area is $130 \mu\text{m}^2$ with a deviation of $15.8 \mu\text{m}^2$, and its mean volume is $96 \mu\text{m}^3$ with a deviations of $16.1 \mu\text{m}^3$ [Fung, *et al.* 1981]. The range of size within a population is a gaussian distribution. Fig. 2.4 shows the normal biconcave shape of red blood cells at rest.

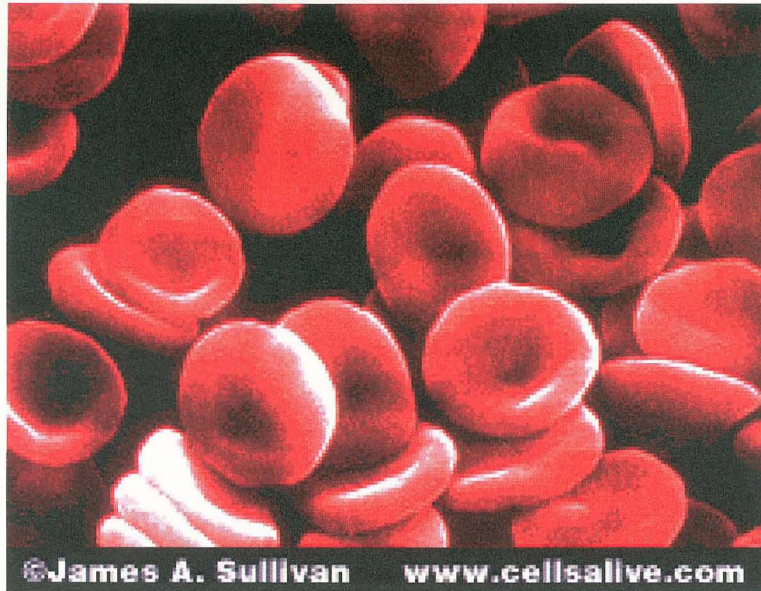


FIGURE 2.4 Scanning electron micrograph of human red blood cells

The average sphericity of red cells is 0.77. The sphericity Sph is defined as following with maximum value of 1.0:

$$Sph = \frac{4\pi}{(4\pi/3)^{2/3}} \cdot \frac{V^{2/3}}{A} \quad (2.1)$$

where V is the volume, A is the surface area.

The following red cells values are from the Handbook of Bioengineering of Perry and Gertrude [1987].

Density: 1.10 g/cm^3

Diameter (dry film): $7.7 \text{ }\mu\text{m}$

Average thickness: $1.95 \text{ }\mu\text{m}$

Mean corpuscular hemoglobin concentration (g/100 mL RBCs):

30.2 (male), 30.2 (female)

Lifetime: 100 to 130 days

Normal daily destruction: $2 \times 10^{11} \approx 0.83\%$

Reticulocyte lifetime: 1 to 2 days

The membrane's parameters of RBCs in Table 2.1 are from Waugh & Hochmuth [2002].

TABLE 2.1 Membrane parameters for a typical red blood cell (37°C) [Waugh & Hochmuth, 2002]

Membrane area modulus	480 mN/m
Membrane shear modulus	0.006 mN/m
Membrane viscosity	0.00036 mN·s/m
Membrane bending expansivity	0.2×10^{-18} J
Thermal area expansivity	0.12%/°C
$\frac{1}{V} \frac{dV}{dT}$ (<i>V</i> - volume, <i>T</i> - temperature)	-0.14%/°C

The interior of a red cell is a concentrated solution of hemoglobin (the oxygen-carrying protein) and behaves as a Newtonian fluid [Cokelet & Meiselman 1968]. The hemoglobin concentration is about 290~390 g/l in a normal population of cells. Table 2.2 shows the viscosity of red cell cytosol [Waugh & Hochmuth 2002].

TABLE 2.2 The viscosity of red cell cytosol (37°C) [Waugh & Hochmuth 2002]

Hemoglobin Concentration (g/l)	Measured Viscosity (mPa·s)	Best Fit Viscosity (mPa·s)
290	4.1-5.0	4.2
310	5.2-6.6	5.3
330	6.6-9.2	6.7
350	8.5-13.0	8.9
370	10.8-17.1	12.1
390	15.0-23.9	17.2

Mechanical Properties of Erythrocyte Membrane

The one-dimensional schematic of erythrocyte membrane structure is shown in Fig. 2.5 [John, *et al.* 1999]. It includes two significant layers: 1) lipid bilayer and 2) underlying spectrin network (also called membrane skeleton). The red cell membrane has unique viscoelastic properties resembling a fluid in some respects and a solid in others. It

provides viscous resistance to deformation, but responds elastically to area strain. The viscous resistance to deformation is provided by the lipid bilayer, which separates plasma from cytoplasm, and acts like a two-dimensional fluid in Fig. 2.6 [Evans, *et al.* 1977]. The membrane skeleton offers most of the elastic response to two-dimensional deformation, as well as bending in the third dimension. The Kelvin solid model can be used to represent the combined viscoelastic response of the membrane, where the total shear stress is comprised of a viscous and an elastic component. Physically, the viscous component comes from the fluid-like behavior of the lipid bilayer, and the elastic component arises from the stretching of the membrane skeleton. The multiple layer structure of the erythrocyte membrane causes many damaging mechanisms of the membrane, such as: 1) failure of only the bilayer when the membrane skeleton is intact, 2) failure of only the bilayer when the membrane skeleton has been damaged, and 3) a simultaneous failure of both the bilayer and membrane skeleton.

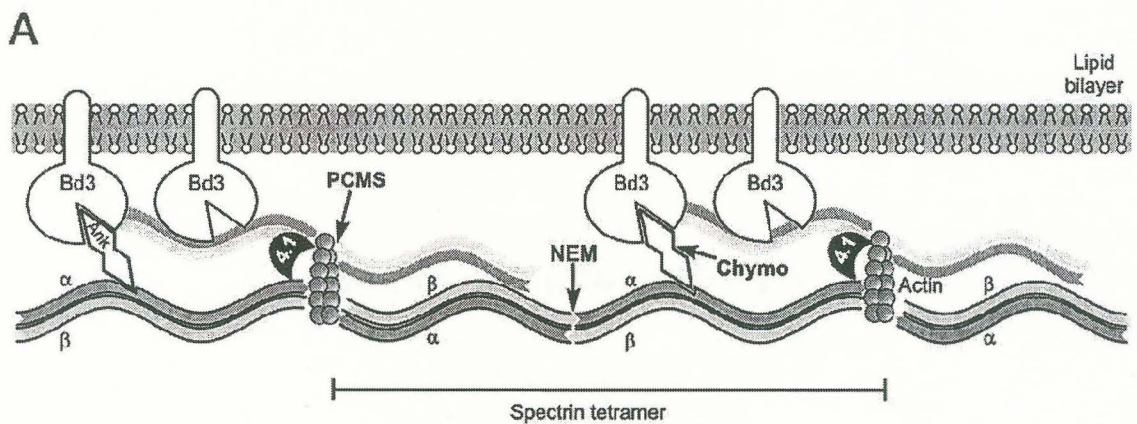


FIGURE 2.5 Schematic of erythrocyte membrane [John, *et al.* 1999]

In the above illustration, λ_1 and λ_2 are the principal extension ratios for the deformation. T_1 and T_2 are the principal tensions (force/length) defined as follow:

$$T_1 = \mu_m \frac{\lambda_1^2 - 1}{2} + \eta_m \frac{\dot{\lambda}_1}{\lambda_1} + \hat{T} \quad (2.2)$$

$$T_2 = \mu_m \frac{\lambda_2^2 - 1}{2} + \eta_m \frac{\dot{\lambda}_2}{\lambda_2} + \hat{T} \quad (2.3)$$

where μ_m is the shear modulus, η_m is the coefficient of viscosity for the membrane surface in shear flow, and \hat{T} is the biaxial tension causing area dilation of a cell surface.

$\dot{\lambda}_i$ represents $\frac{d\lambda_i}{dt}$, $i=1$ or 2 , t is the time. The values for normal RBC are $\mu_m = 0.0061 \pm 0.0012$ dyn/cm and $\eta_m = (6 \pm 2) \times 10^{-4}$ poise-cm [Hochmuth, *et al.* 1979], and they are temperature dependent. For $\lambda_i < 3$, μ_m and η_m are dependent on the cytoskeleton and don't appear to be influenced by membrane lipid properties.

Because the red cell membrane greatly resists area dilation, the deformation can be assumed to occur at constant element surface area (i.e. treat the membrane skeleton as locally incompressible layer). Then $\lambda_1 \cdot \lambda_2 \approx 1$, i.e. $\frac{\dot{\lambda}_1}{\lambda_1} + \frac{\dot{\lambda}_2}{\lambda_2} = 0$, and $\lambda_2 = \lambda_1^{-1}$. Then,

$$T_2 = \mu_m \frac{\lambda_1^{-2} - 1}{2} - \eta_m \frac{\dot{\lambda}_1}{\lambda_1} + \hat{T} \quad (2.4)$$

Therefore,

$$T_1 - T_2 = \mu_m \frac{\lambda_1^2 - \lambda_1^{-2}}{2} + 2\eta_m \frac{\dot{\lambda}_1}{\lambda_1} \quad (2.5)$$

$$T_1 + T_2 = 2\hat{T} + \mu_m \frac{(\lambda_1 - \lambda_2)^2}{2} \quad (2.6)$$

So,

$$\hat{T} = \frac{T_1 + T_2}{2} - \mu_m \frac{(\lambda_1 - \lambda_2)^2}{4} \quad (2.7)$$

This equation will be used in the blood damage model in Chapter III.

Complexity of RBC's Deforming Movement in Blood Flow

The deformation and movement of red cells in blood flow are very complicated. Red cells show various patterns of deformation under different flow conditions. A red cell of 8 μm in diameter can deform to traverse the 3~4 μm diameter capillaries of the microcirculation. It also displays various rheologic behaviors when suspended in larger vessels [Conrad, *et al.* 1985]. Figure 2.8 shows the change of the shape of a red cell under different shear rates [Secomb 2003], where the untreated human red cell was suspended in a high viscosity medium (13cP), and subjected to a linear shear flow set up in a counter-rotating cone-and-plate chamber. The flow direction is from top to bottom, and the velocity gradient is perpendicular to the page. As the shear rate increased, the shape of the red cells changed from a biconcave disk, to an ellipsoid, and then to an elongated spindle-like shape with the long axis approximately aligned with the flow direction.

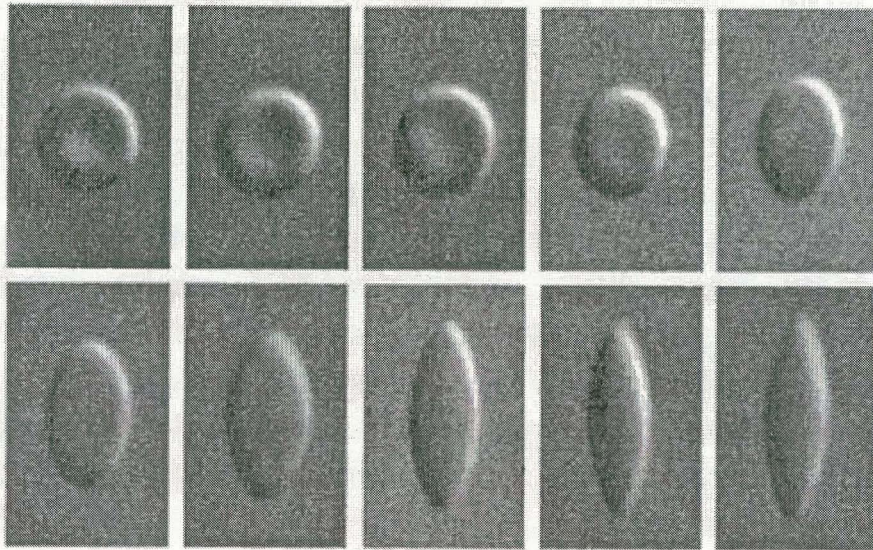


FIGURE 2.8 Images of the deformation of RBC at several different shear rates (starting with upper left image: 0, 8.7, 18, 35, 70, 140, 270, 530, 1100, and 2200 s^{-1}) [Secomb 2003]

The viscosity of the internal and external phases of RBC also impacts the rheologic behaviors. Observation with the Rheoscope [Conrad, *et al.* 1985] showed that: 1) if the viscosity of the external phase was low, red cells tend to tumble and behave unstably in the shear field; 2) above a critical level of external phase viscosity, the cells became stable and elongated in the direction of shear; 3) when stable orientation was achieved, the cell membrane rotated about the cytoplasm in a fashion termed “tank-treading” (both the degree of cell deformation and the frequency of membrane rotation - tank-treading frequency i.e. TTF, increased with increasing shear rate); 4) at constant levels of shear rate, the extent of red cell deformation increased as the external medium became more viscous. Fig. 2.9 shows the steady tank-treading motion of the membrane around the interior at shear rate 270 s^{-1} , and the motion is evident from the motion of the marker particles [Fisher & Schmid-Schonbein 1977] and [Secomb 2003]. To prepare the marker, polystyrene beads ($1.0 \text{ }\mu\text{m}$, Dow Chemical Co., Indianapolis, IN) were added to

the cell suspensions. These beads adhered to the red cell membrane in the absence of plasma proteins [Tran-Son-Tay, *et al.* 1984]. While the distribution of beads among cells was uncontrolled, an adequate number of cells with no more than two beads attached were usually obtained.

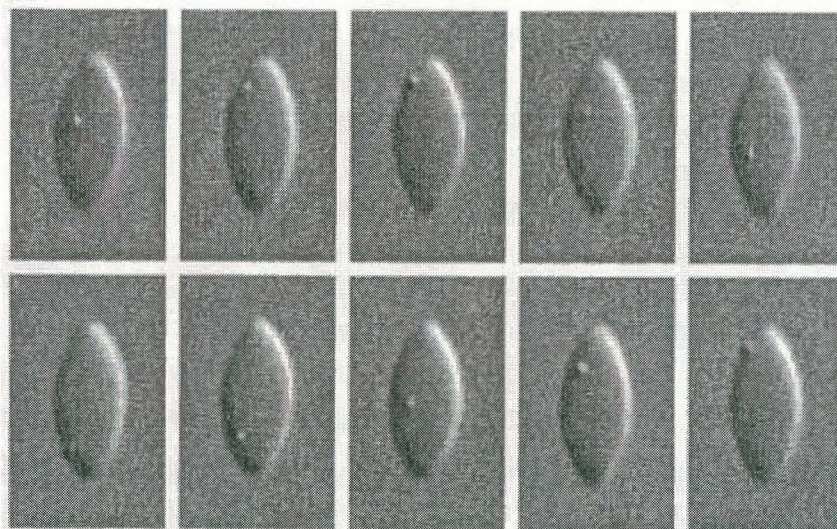


FIGURE 2.9 Tank-treading motion of RBC membrane at time interval of 20ms [Secomb 2003]

Another large category of research which may relate to red cell behavior is the research of capsules. A capsule consists of an internal deformable substance that is enclosed by a semi-permeable membrane. The main role of the membrane is to confine the encapsulated material and control the substance exchange across the capsule. Natural capsules are cells; artificial capsules include various industrial powder, biological particles, and drugs. Artificial capsules have applications in a broad range of industries, including the pharmaceutical, cosmetics, and food industries. Capsule technology also has applications in artificial organs and cell therapy where living cells are encapsulated for the treatment of disease such as diabetes and liver failure [Barthes-Biesel 2003]. Such research may help to study the behavior of red cells in large scale and capillary blood

flow. There are many theoretical works and numerical simulations concerning the deformation of capsules. Normally, artificial capsules are uniform in size, and have membranes with known characteristics. But the membrane structure of red cells is much more complicated than these of artificial capsules. Fig. 2.10 & 2.11 depict the numerical simulation of the deformation motion of red cells [Pozrikidis 2003 and Ramanujan & Pozrikidis 1998], in which the cells were modeled as deformable liquid capsules enclosed by an elastic membrane resistant to shearing and bending deformation. The period of overall rotation of cells from numerical results showed good agreement with the experimental observations of Goldsmith and Marlow [1972] for red cells suspended in plasma.

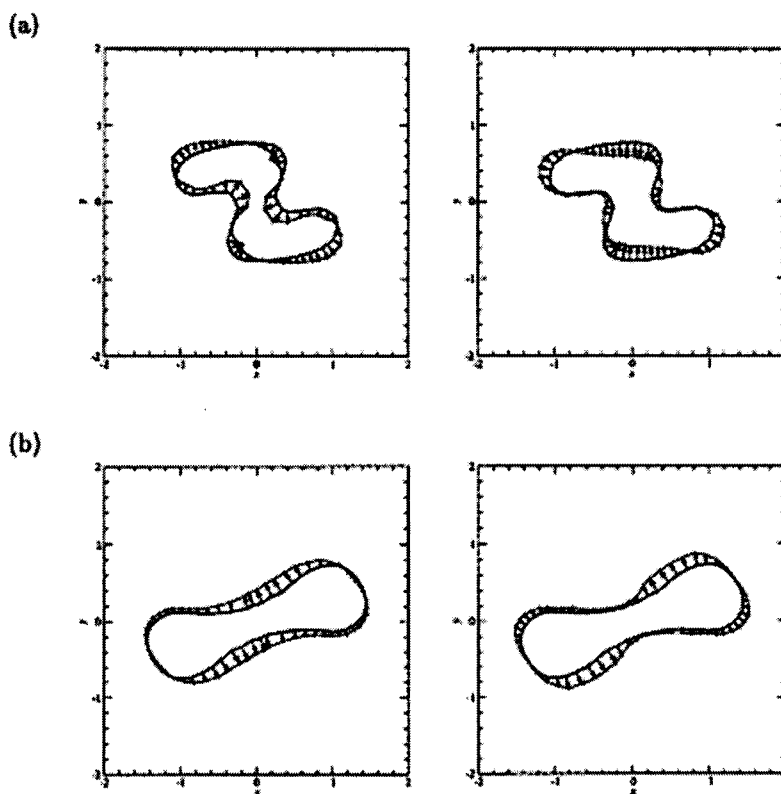


FIGURE 2.10 2D plot of simulation of flow-induced deformation of red blood cells [Pozrikidis 2003 and Ramanujan & Pozrikidis 1998]

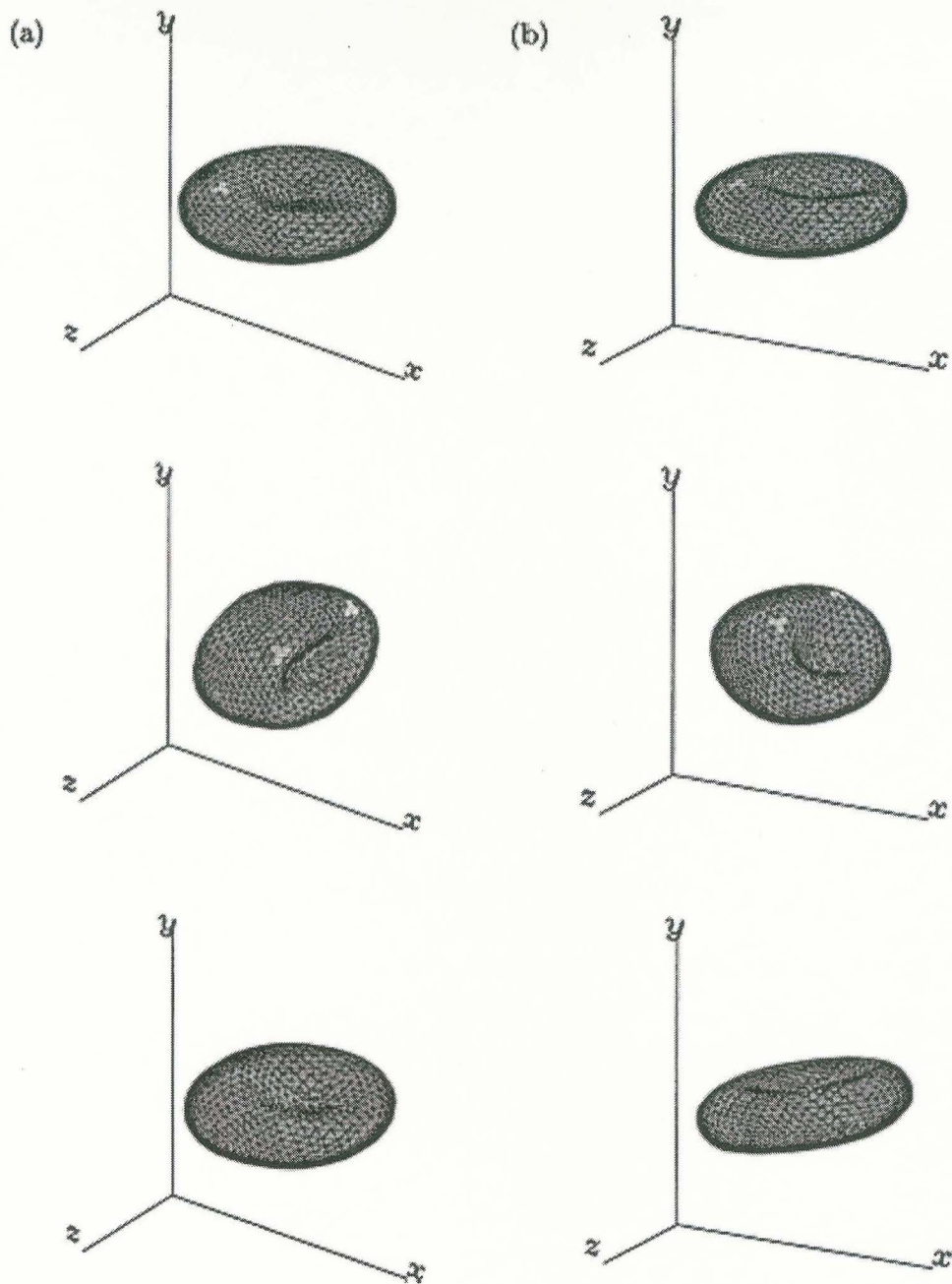


FIGURE 2.11 3D plot of simulation of flow-induced deformation of red blood cells [Pozrikidis 2003 and Ramanujan & Pozrikidis 1998]

Mechanism of Hemolysis

The mechanism of hemolysis is complicated and difficult to describe with a single criterion. There are numbers of physical factors related to red cell damage

including: foreign materials, injurious wall contact, flow through apertures, high shear stress, turbulent flow, accelerating flow, pressure gradients, and blood-gas interfaces etc. Lokhandwalla & Sturtevant [2001] summarized the mechanism of cell lysis in Fig. 2.12. The category of fluid dynamic forces represents fluid forces acting on the cell membranes, which are due to inertia of the fluid particles and the tangential viscous stresses. The cell's deformation and lysis can be categorized into two modes: 1) inertial mode (the cell membrane is very weak compared with the inertial forces) and 2) viscous mode (the cell membrane is strong compared with the inertial forces). Both modes include steady flow and unsteady flow situations. Inertial mode dominates in very short exposure time, such as bubble flow and shockwave flow. Most of the flows in cardiovascular devices are viscous mode.

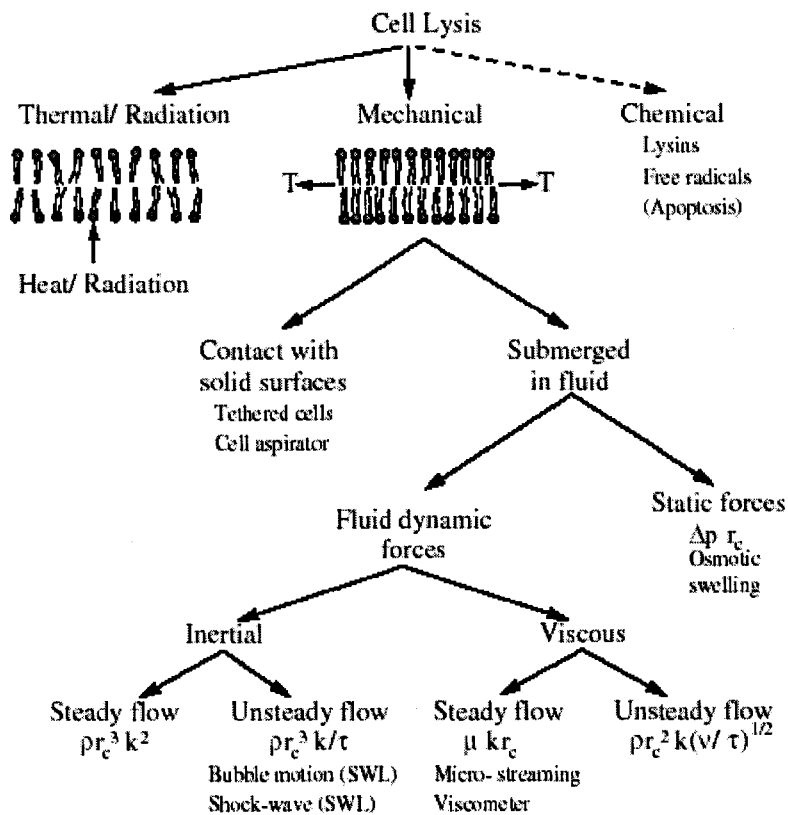


FIGURE 2.12 Cell lysis mechanism [Lokhandwalla & Sturtevant 2001]

Fluid shear (the bulk shear stress of the flow) is one of the important factors for the development of artificial devices. Many investigations of mechanical hemolysis have been carried out in vitro. Blackshear [1972] defined three classes of mechanical hemolysis: 1) surface-induced, i.e. dependent on the extent of the surface and proportional to the square of the shear rate in the boundary layer, 2) in-bulk, medium stress (1,000-2,000 dyn/cm²), 3) in-bulk, high stress (order of 40,000 dyn/cm²). The research in this paper will focus on mechanical lysis of medium and high in-bulk stress.

A simple experiment to show membrane characteristics is osmotic swelling which induces the lysis of cells. It has been observed that during osmotic swelling the cell volume increase significantly (75%), whereas its area remained almost constant (increases by only 7%) [Evans & Fung 1972]. Lysis is expected to happen when an increase of surface area of RBC is greater than some threshold value [Rand 1964]. The critical area strain for lysis appeared to be about 6.4 percent. Above this threshold, pores in the cell membrane grew large enough to allow cell contents to escape or the cell membrane to break into fragments. For brief exposure to high stress, pores might reseal before cell contents have escaped.

Rand [1964] built a viscoelastic model for red cell membranes. The model consisted of the following: A purely elastic element represented by a spring Y_2 ; A purely viscous component represented by a dash-pot η_2 ; A parallel arrangement of a spring Y_1 and a dash-pot η_1 ; all of which are laid in series (Fig. 2.13). The response of strain S of the above combination to a step function of applied stress F is solved by Laplace transformation:

$$S = F \left[\frac{1}{Y_2} + \frac{1}{Y_1} \left(1 - \exp \frac{-Y_1}{\eta_1} t \right) + \frac{t}{\eta_2} \right] \quad (2.8)$$

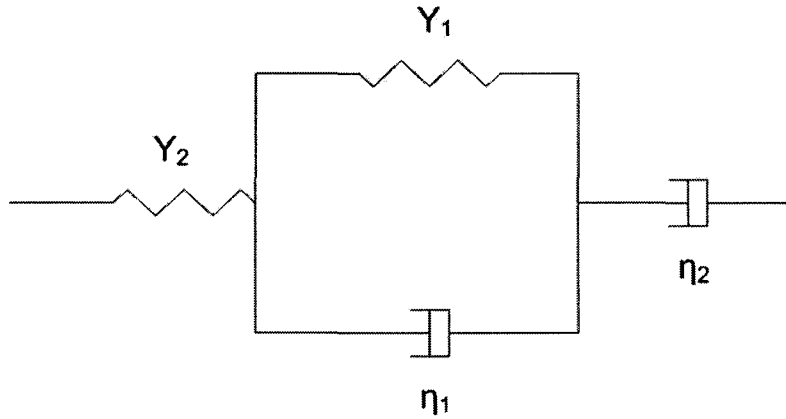


FIGURE 2.13 Rand's mechanical model of the cell membrane

Rand's model concluded (based on above mechanical models) that the critical biaxial local tension σ_c at lysis depended upon the duration of the imposed stress:

$$\frac{1}{\sigma_c} = \frac{1}{S_c h} \left[\frac{1}{Y_2} + \frac{1}{Y_1} \left(1 - \exp \frac{-Y_1}{\eta_1} t \right) + \frac{t}{\eta_2} \right] \quad (2.9)$$

where S_c is linear strain ($\lambda-1$), h is membrane thickness, and Y_2 is Young's modulus.

Most data supports this model whether lysis is caused by osmosis, fluid shear, or flow of cells through small openings. For a short duration (less than 1 second) of biaxial membrane tension, lysis occurs at principle membrane tensions $T_1 = T_2 = 30$ dyn/cm. For a longer duration (larger than 10 seconds) of biaxial membrane tension, $T_1 = T_2 < 15$ dyn/cm can cause lysis. For uniaxial tension, lysis occurs at $T_1 = 60$ dyn/cm for brief stress.

But the above analysis only relates the red cell lysis to the local membrane tension. It is still difficult to show a relationship between red cell lysis and flow stress because of the complicated deformation of red cells. The fluid shear stress at which

critical uniaxial membrane tension occurred depended on cell size, shape, and motion [Williams 1973]. Currently there is no generalized correlation between external fluid stress and membrane stress. There were some power-law regression models applied to the design of artificial devices. They were purely empirical models to relate the index of plasma free hemoglobin to the shear stress and exposure time. One blood damage model proposed by Heuser, *et al.* [1980] is as follows:

$$\Delta Hb / Hb = 1.8 \times 10^{-6} \times t^{0.765} \times \tau^{1.991} \quad (2.10)$$

where Hb is total hemoglobin content, ΔHb is the released hemoglobin content, t is the exposure time, τ is the shear stress.

Another blood damage model proposed by Giersiepen, *et al.* [1990] is as follows:

$$\Delta Hb / Hb = 3.62 \times 10^{-5} \times t^{0.785} \times \tau^{2.416} \quad (2.11)$$

These regression models are very convenient to estimate the blood damage, and several reports show they are effective. But in this paper (Chapter IV), numerical simulations show that these models can not correctly predict the trend of hemolysis of three kinds of hypodermic needles in another project. To predict the hemolysis of our particular needles, a strain-based blood damage model from Rand's viscoelastic model was constructed and optimized from the microscope images of red cells under stress.

CHAPTER III

EXPERIMENTAL INVESTIGATION OF FLOW-INDUCED HEMOLYSIS AND STRAIN-BASED BLOOD DAMAGE MODEL

Purpose of Investigation

As discussed in Chapter II, the cells' deformation among blood flow is very complicated. While these studies have expanded our understanding of red cell behavior in simple flows, the high concentration of cells in whole blood, as well as the complexity of red cell deformation and membrane failure response constitute barriers to direct simulation of cells in suspension in cardiovascular flows. In the short term, continuum models for predicting hemolysis may be useful.

With the advances in computational fluid dynamics (CFD) technology and the increasing affordability of high speed computing, numerical simulation of complex fluid systems has become a feasible tool for engineering design. But in order to analyze hemolysis in blood-handling devices with numerical methods, an accurate blood damage model relating flow conditions to cell rupture is necessary. Sharp & Mohammad [1998] used a curve fit to relate the critical shear stress τ_{sc} for hemolysis with exposure time t in hypodermic needles: $t(\tau_{sc}/1500-1)^2 = 0.01$. Heuser, *et al.* [1980] built a model based on a power-law to estimate the percentage of plasma free hemoglobin from shear stress and exposure time: $\Delta Hb/Hb = 1.8 \times 10^{-6} \times t^{0.765} \times \tau_s^{1.991}$. Giersiepen, *et al.* [1990] provided another

similar empirical model with different coefficients: $\Delta\text{Hb}/\text{Hb}=3.62\times 10^{-5}\text{xt}^{0.785}\text{x}\tau_s^{2.416}$.

These blood damage models are purely empirical.

While these models have been applied to complex flows, they have thus far been validated by experimental measurements of hemolysis only in simple flows. Since these empirical models relate fluid stress conditions directly to bulk blood damage, they lack a logical connection to the deformation of red cells under fluid stress, which is experimentally observable and which might be used for validation purposes. Because they don't include a mechanism of red cell deformation to the point of lysis, it is challenging to incorporate new understanding about red cell behavior into the models to improve them. In this paper, a new hemolysis prediction model is developed that is based on a threshold of membrane strain. The new model provides a foundation incorporating preliminary mechanics of membrane rupture that can be expanded as more insight is gained into the mechanisms of hemolysis in complex flows. In the current model, several simplifications were imposed and three empirical coefficients remain.

One necessary component of the new hemolysis prediction model to be applied to CFD-generated flow fields was a model of membrane response in the ranges of membrane stress and strain that cause membrane failure. Hochmuth, *et al.* [1979] constructed a viscoelastic model for the red cell membrane with experiments in which the cell was stretched with a micropipette and then released. Viscoelastic properties were inferred from the recovery of the cell to its unstressed shape. An improvement was added by Mohandas and Evans [1994] that considered the membrane skeleton locally compressible. On the other hand, Rand [1964] partially aspirated red cells into a micropipette, with the remaining part of the cell forming a sphere outside the pipette, and

measured the time required for the cell to be drawn completely into the bore. The range of exposure time to the resulting biaxial membrane tension was several seconds to 200 seconds. Because these experiments exposed the cells to stress and strain in the ranges relevant to at least partial membrane failure, Rand's model was used for the new hemolysis prediction model. Another necessary component of the new hemolysis prediction model was a relationship between the flow field and red cell membrane stress. Of particular interest is the maximum local membrane stress history sufficient to cause failure of the membrane. However, because direct simulation of this fluid/structure interaction for whole blood flow is beyond the capacity of current technology, a simplifying hypothesis was applied here. Specifically, it was assumed that membrane stresses scale with continuum fluid stresses. This principle, which also underlies the hemolysis prediction models of Heuser, *et al.* [1980] and Giersiepen, *et al.* [1990], ignores the many types of flow-dependent red cell motion and unifies the relationship between membrane and fluid stresses ad hoc for the empirical models, but implies a characteristic cell shape and orientation leading to membrane failure for a more mechanistic model. A candidate cell shape is provided by Sutura & Mehrjardi [1975], who sheared human red cells in a concentric cylinder viscometer with rotating inner cylinder. Cell deformation was fixed with glutaraldehyde after 4 min of shearing and observed under a scanning electron microscope (SEM). Cells were found to deform gradually toward a smooth prolate ellipsoidal shape as shear stress increased from 100 to 2500 dyn/cm². Fragmentation of cells occurred at stresses above 2500 dyn/cm².

Finally, hemolysis data from measured flow fields was necessary to validate the new model. Many experiments have been performed to find the empirical relationship

between shear stress and hemolysis, which has also been shown to depend on exposure time (Table 3.1).

TABLE 3.1 The critical shear stress under various flow conditions

Exposure time: t (s)	Critical shear stress: τ_c (dyn/cm ²)	Geometry	Species	Reference
10 ⁻⁶	10 ⁵	Estimation	human	Hellums & Hardwick [1981]
10 ⁻⁵	4x10 ⁴	Turbulent jet	human	Forstrom [1969]
10 ⁻⁴	5600	Oscillating wire	human and canine	Williams, <i>et al.</i> [1970]
10 ⁻³	4500	Oscillating bubble	human and canine	Rooney [1970]
10 ²	1500	Concentric cylinder	human	Leverett, <i>et al.</i> [1972]
2.4x10 ²	2500	Concentric cylinder	human	Sutera, <i>et al.</i> [1975]

Leverett, *et al.* [1972] observed lysis of human red cells at a fluid shear stress of 1500 dyn/cm² for a duration of 2 min in flow between concentric cylinders. On the other hand, in the experiments of Sutera and Mehrjardi [1975], fragmentation of cells occurred at a stress above 2500 dyn/cm² after about 4 min in the flow of a concentric cylinder viscometer. Most concentric cylinder experiments investigating hemolysis involved exposure time of 100 s or longer. Rooney [1970] observed the threshold of hemolysis for human and canine red cells to be at a critical shear stress of 4500 dyn/cm² for duration of about 10⁻³ s in flows generated by an ultrasonically pulsating gas bubble. Williams, *et al.* [1970] found the threshold of hemolysis of human and canine red cells at a critical shear stress of 5600 dyn/cm² for duration of about 10⁻⁴ s in the flow surrounding a transversely oscillating wire. Forstrom [1969] found a critical shear stress of 40000 dyn/cm² for human red cells for a duration of about 10⁻⁵ s in jet flow. For shockwave flow, exposure time as short as 10⁻⁹ s occurred [Williams, *et al.* 1999 and Lokhandwalla 2001]. Cell lysis

was caused by inertial forces. For a shock wave strength of 40 MPa, the inertial force was 910 dyn/cm^2 lasting for 3×10^{-9} s. Such an inertial force caused area strain of about 10^{-5} , which is not enough for membrane rupture, but enough to induce transient pores that can allow the release of hemoglobin (critical area strain of $10^{-7} \sim 10^{-5}$).

In addition, for a mechanistic model, observations of cell deformation at strains less than the threshold level can be used to calibrate the model. Sutura & Mohammad [1975] used a unique method measuring the deformation of cells with a SEM and the plasma free hemoglobin with a spectrophotometer. Mean length of fixed cells was measured. They observed that the deformation evolved into an ellipsoidal shape as shear stress was increased from 100 to 2500 dyn/cm^2 , and fragmentations of the cells appeared at stress above 2500 dyn/cm^2 . With this method, however, it was necessary to use a fixing agent (glutaraldehyde) which may have influenced cell motion, and, therefore, cell shape. In this project, a high-speed image capturing system was used to collect additional data on red cell deformation in shear flow without the need for fixing chemicals.

The amount of hemoglobin that escapes through the cell membrane depends on the dynamics of membrane failure. In the Rand [1964] model, lysis is predicted to occur when an increase of membrane surface area exceeds a threshold value of 6.4 percent. Above this threshold, pores in the cell membrane may grow large enough to separate the cell into fragments, allowing all cell contents to escape. Alternatively, for brief exposure to high stress, pores may reseal before cell contents have escaped [Lokhandwalla & Sturtevant 2001]. This stress and time dependent hemoglobin release was treated empirically and is left for future work to be mechanistically modeled.

Most previous experiments fell into two categories: a) red cells were suspended in fluid (plasma or other solution) and sheared with device, then hemolysis was determined by measuring free hemoglobin with a spectrophotometer; b) a single cell was manipulated and stretched with micropipettes, and membrane characteristics were calculated. Fig. 3.1 shows the cone/plate device [Shigehiro 1989] used to shear red blood cells. The cone/plate device was widely used in hemolysis analysis because there exists an approximated solution of uniformly distributed shear stress and that makes it easy to estimate the shear stresses experienced by the red cells. Fig. 3.2 shows the micropipette experiment of Rand [1964], in which a portion of a red cell was sucked into a micropipette, and the outside portion was kept as a sphere shape. The time until the membrane was broken was measured. Fig. 3.3 shows the micropipette experiment of Hochmuth [1979], in which the corner of a red cell was sucked into the micropipette and released. The time that it took for the red cell to restore its biconcave shape was measured. Sutura & Mehrjardi's experiment [1975] used a unique method, measuring the deformation of cells with a SEM and the free hemoglobin with a spectrophotometer. With this method, however, it was necessary to use a fixing agent (glutaraldehyde) which may have influenced cell motion, and, therefore, cell shape (Fig. 2.3).

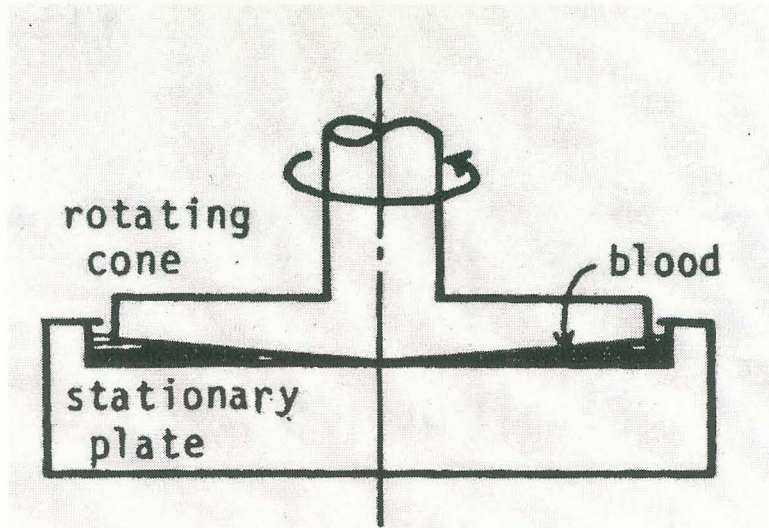
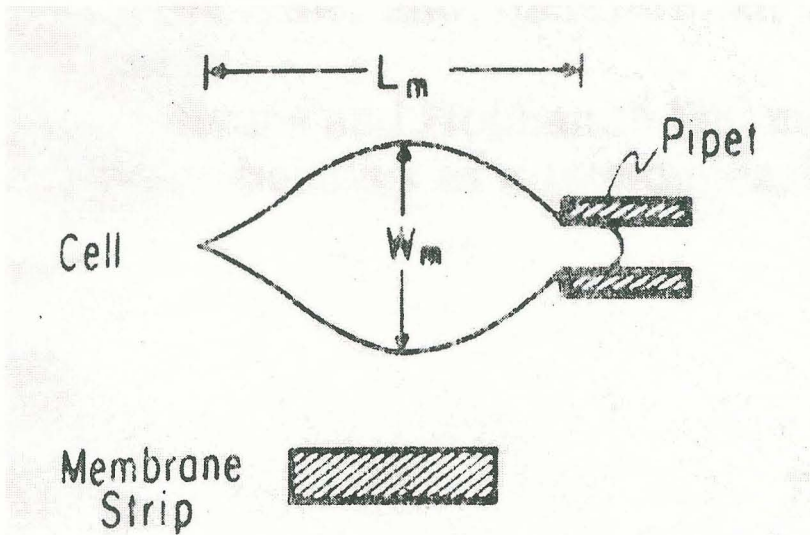


FIGURE 3.1 Cone/Plate [Shigehiro 1989]



[Rand 1964]



[Hochmuth 1979]

FIGURE 3.2 Micropipette Experiment

In summary, in this Chapter, a non-invasive alternative method to investigate cell deformation during flow was introduced. Images of moving cells deformed by a range of fluid stresses in a two-dimensional Poiseuille flow were captured with a microscope-laser-camera system. In addition, a strain-based blood damage model was developed that enabled estimation of the strain and deformation of red cells under fluid stress. The aspect ratios of captured images of red cells were compared to the predictions of the strain-based blood damage model to optimize the empirical coefficients in the model.

Experimental Methods

An experimental system to create an observable, controlled flow under a microscope was constructed (Fig. 3.3). The experimental system comprised a flow system and an image capturing system. The flow system consisted of a flow chamber, an upstream syringe pump (60 ml), and a down stream fluid reservoir. The image capturing system comprised a microscope, a laser strobe system, a digital camera and an image acquisition computer.

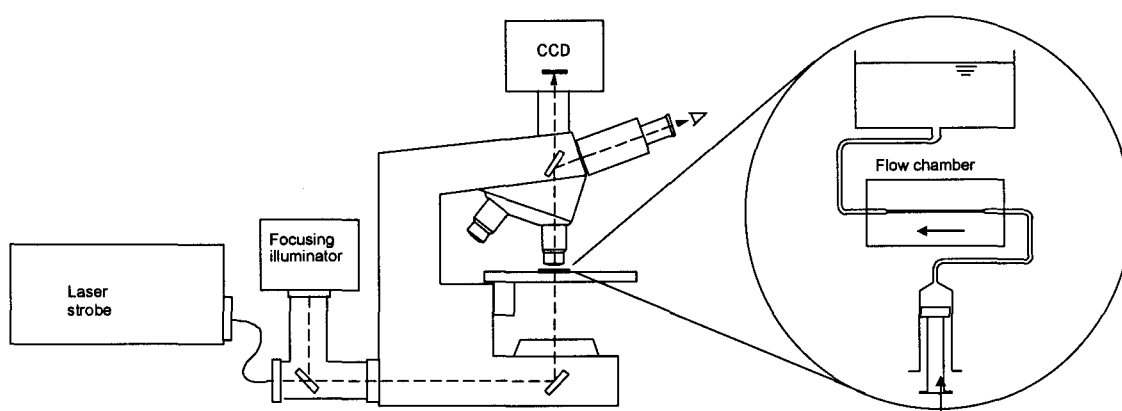


FIGURE 3.3 Schematic of experimental system

The chamber designed to produce two-dimensional Poiseuille flow is shown in Fig. 3.4. The design of the flow chamber is crucial to this experiment. Several methods have been tried to get a better design. One method was to use a polycarbonate spacer covered by two microscope cover slips (Gold Seal Cover Glass, 35 mm x 60 mm, thickness of 0.17 mm) on top and bottom respectively. Silicone oil (Aquarium Sealant, 100% Silicone) was used to seal it. The seal was a challenging problem, especially when the positive pressure was applied to the flow chamber. The cover slips were fragile, and would contaminate the platform of the microscope once broken. If negative pressure was applied, the leakage was not so serious, but the bubbles were sometimes disastrous. Another shortcoming of negative pressure was that the pressure drop was limited to vapor pressure. It was often not enough pressure to generate flow velocity with cell lysis. Finally, we use another method. The channel (0.4 mm wide, 2.4 mm tall, and 40 mm long) was formed from two pieces of polymethyl methacrylate (PMMA), each fabricated by micro-machining, and then bonded together with acrylic cement (Craftics #33 for Acrylic sheet, Acylite Lucite, Plexiglas, www.craftics.com). The total external thickness of the chamber was about 2.6 mm. The drawing of the designed chamber was shown in APPENDIX C. Two 18-gauge stainless steel needles were connected to the chamber as inlet and outlet. The above method created a very strong flow chamber and could withstand large enough pressure to produce a flow of up to 4 m/s without the leaking problem. The only disadvantage of this method is that it is not easy to polish the inner surface of the PMMA chamber to get very high quality microscope pictures. The flow chamber was placed on the stage of a Zeiss Photomicroscope II microscope with an attached digital camera (Fig. 3.5).

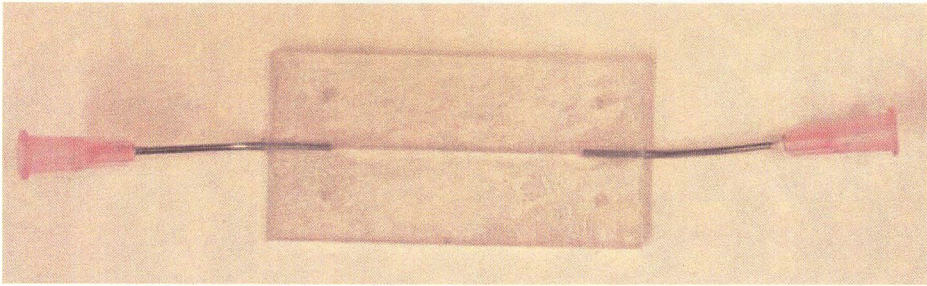


FIGURE 3.4 Flow chamber

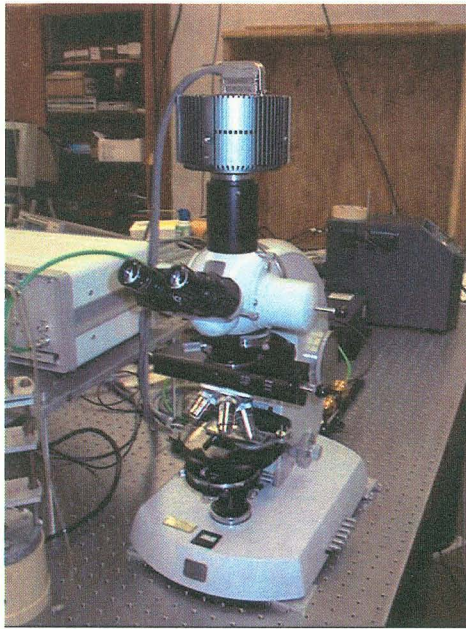


FIGURE 3.5 Microscope and digital camera

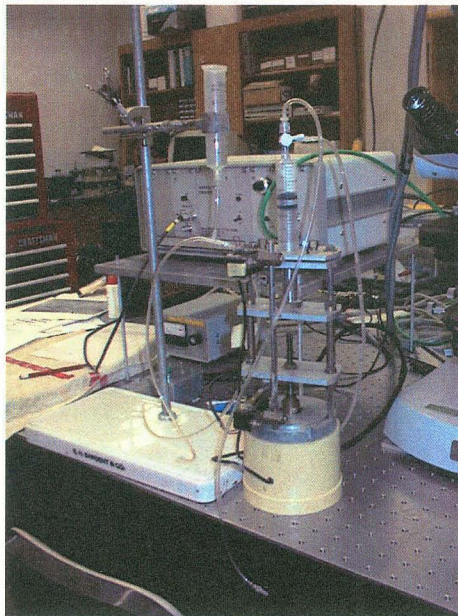


FIGURE 3.6 Syringe pump

The syringe pump (Fig. 3.6) used to produce the flow through the channel was driven by a DC motor, powered by 21.5 volts. As stated above, positive pressure was applied to the channel to avoid vapor bubbles which might be problematic for the microscope image and for estimating the flow rate.

A diluted suspension of red cells was forced by the syringe pump through the flow channel. The volume of flow for each trial was 23 ml. A timer was installed to record the duration of each run so that the volume flow rate could be calculated. The suspending fluid was a solution of Dextran-500 (Fisher Scientific Inc.) in distilled water with 0.9% sodium chloride (Fisher Scientific Inc.), with viscosity of 11.1 cP for all samples except S0, which was mixed to 8 cP. Dextran-500 was supplied with powder. The solution was prepared one night before the experiment to make sure the powder was fully dissolved. The viscosity of the fluid was measured by a Wells-Brookfield cone/plate viscometer. Seven experiments were run, each with red cells from different donors. The flow was steadily laminar, with average velocity of about 3.2-3.9 m/s and Reynolds number Re of 100-200, depending on the viscosity of the dextran solution. The shear stress at the wall τ_w was 4700-5600 dyn/cm^2 depending on the flow rate and fluid viscosity. The time required for a red cell to travel along the whole channel at the mean flow velocity was about 10 ms. A schematic diagram of the channel flow is shown in Fig. 3.7. The actual size of the field of view for the 16x objective was about 0.2 mm long and 0.15 mm wide.

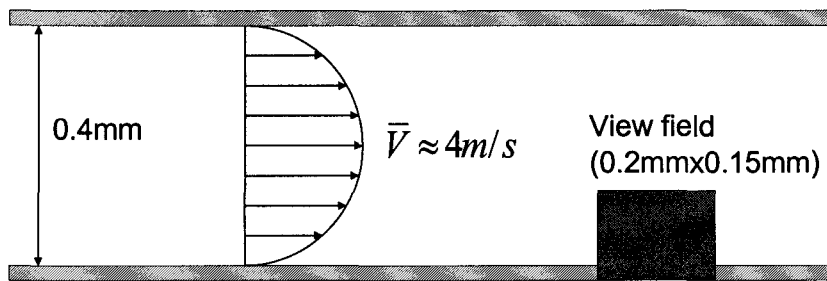


FIGURE 3.7 Schematic diagram of the channel flow

To stop the motion of this high-speed flow, an Nd-YAG laser (Fig. 3.8) with 3 ns pulse width and approximately 20 μJ pulse energy at 543 nm wavelength was used to strobe the field of view. The laser and the microscope system were mounted on a Newport optical table for stability and vibration isolation. The major problem with using a single wavelength laser for illumination was the laser speckles. To reduce laser speckle, an optical fiber (Fig. 3.9) with a 30 m length and diameter of 3 mm was used to modulate the laser light. The optical fiber was purchased from Digi-Key Company (Unjacketed Fiber, dial 3000 μm , part No. IF-C-U3000). The laser light from the Nd-YAG laser entered the optical fiber, and then was expanded and collimated by two convex lenses (one 16x, another 4x) at the exit of the optical fiber before entering the microscope. The optical fiber was covered with an opaque shrink tube. The ends of the optical fiber were polished with sand paper, and were attached to the Newport optical table with a holder. The optical fiber improved the laser illuminated image significantly, as shown in Fig. 3.10. White light illumination yielded best image quality, but the short pulsed light source was necessary to stop the fast motion of the flow. The additional benefit of the optical fiber was that it allowed easier layout and alignment of the optical system.

The Carl Zeiss Photomicroscope II was equipped with a series of 6x, 16x and 40x long working distance objective lens (LW lens). For safety reason, filters for 543 nm light wave were attached to the eyepieces of the microscope to block the laser light from entering the eyes, but it kept the ability to observe the field with white light for the experiment setup. The 16x long working distance objective lens was used in order to get an image of the red cells and flow field that was large enough. The narrow depth of focus of the microscope's 16x long working distance objective lens effectively isolated the plane of focus. A QImage QICAM-12 bit Fast 1394 digital camera (1/2 inch Sony ICX205 CCD, 1392x1040 array, 4.65 μm x 4.65 μm pixel size with 10,000 electron well depth, quantum efficiency of 40% at 543 nm, 12 bit resolution, 10 frames per second) was used to capture images. The camera was mounted to the upper port of the Zeiss Photomicroscope II through a Diagnostic Instruments 1x C-mount adapter tube. The QCapture Pro image acquisition software was provided by the camera company. A stage objective micrometer of 100 divisions in 1mm was used to calibrate the QCapture Pro software to measure the distance in the images.



FIGURE 3.8 Nd-YAG Laser

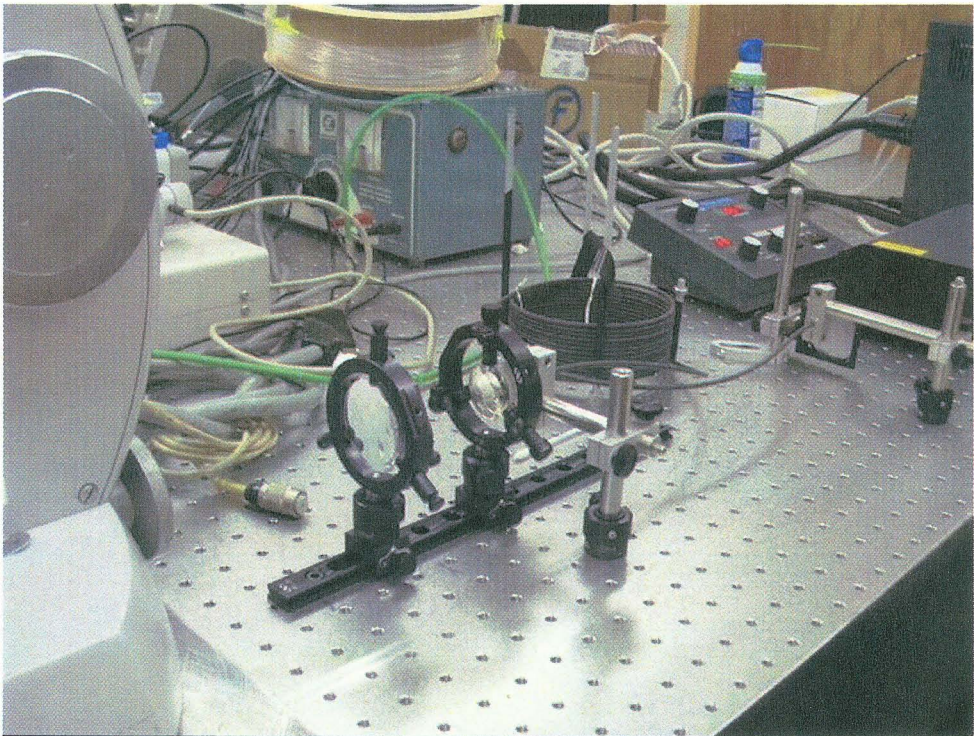
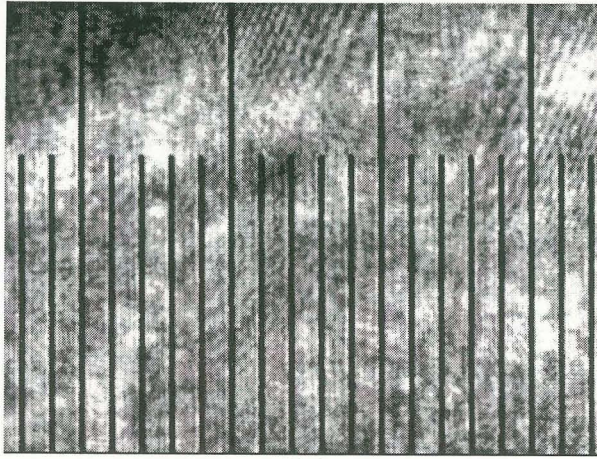
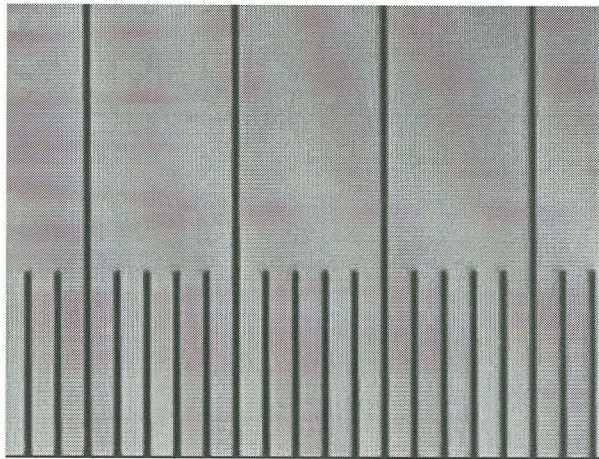


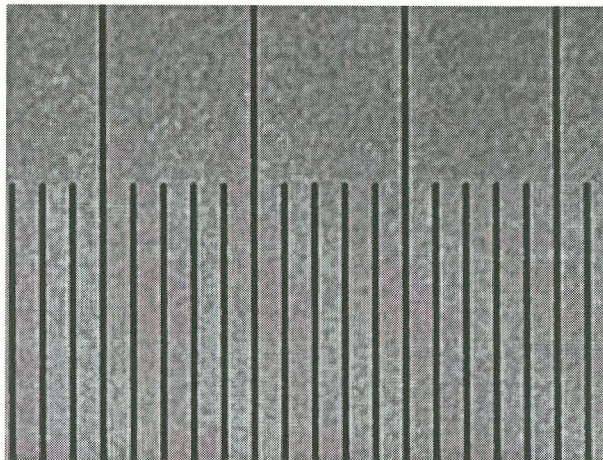
FIGURE 3.9 Optical fiber



(4a)



(4b)



(4c)

FIGURE 3.10 Reduce laser speckle with optical fiber
(4a-laser without optical fiber, 4b-white light, 4c-laser with optical fiber)

For optimal spatial resolution, the Abbe diffraction distance $L=0.53\lambda/NA$ was oversampled by at least two pixels, where λ was wavelength and NA was the numerical aperture of the objective lens. The maximum NA of 1.4 was obtainable in high magnification oil immersion objectives, and the diffraction distance was 206 nm. L could have been reduced by decreasing λ to get a better resolution, but the microscope was optimized for green light (543 nm), and only green laser light was available for this project. The NA's of 6x, 16x, 40x LW lens are 0.20, 0.35, and 0.60 respectively. For green light, their L values were 1439 nm, 822 nm, and 480 nm respectively. The 6x objective lens would provide 2.58x oversampling for spatial resolution ($1439 \text{ nm} \times 2 \times 6 / 4.65 \text{ } \mu\text{m} = 3.71$) with approximately 2x magnification provided by the phototube. This resulted in 3.71 pixels on the camera image plane for the physical object of 1439 nm under the object lens. Similarly, the 16x LW objective lens provided 5.66 oversampling, and the 40x LW objective lens had 8.26 oversampling.

The field of view was $539 \text{ } \mu\text{m} \times 403 \text{ } \mu\text{m}$ for the 6x objective lens ($1392 \times 4.65 \text{ } \mu\text{m} / 2 / 6 = 539 \text{ } \mu\text{m}$, $1040 \times 4.65 \text{ } \mu\text{m} / 2 / 6 = 403 \text{ } \mu\text{m}$), and $202 \text{ } \mu\text{m} \times 151 \text{ } \mu\text{m}$ for the 16x objective lens. The 6x objective lens was utilized during initial trials and setup and to help find the position that we were interested in, and the 16x objective lens was used for the final image acquisition.

The criterion for optimal temporal resolution was that cell displacement in the camera image plane should be less than one pixel during the laser pulse. For the 6x objective lens setup, one pixel temporal displacement would correspond to a cell velocity of 129.2 m/s ($4.65 \text{ } \mu\text{m} / 2 / 6 / 3 \text{ ns} = 129.2 \text{ m/s}$). For cases of 16x and 40x objectives, the

cell velocities were 48.4 m/s and 19.4 m/s. They were well above the expected velocity required to cause hemolysis.

The timing sequence of this system was important for its correct operation. Multiple pictures were taken during each run of the pump. For each picture, the laser was pulsed after the camera shutter was opened. This task was controlled by QCapture Pro (Fig. 3.11). The software was set to take 40 pictures (frames) at its maximum speed of about 0.15s per frame after receiving an external trigger signal. For each picture, the software sent a pulse to the camera to first open its shutter, then sent another pulse to trigger the laser. A timing program written in LabView was used to start the pump first, then after 1 second it sent another pulse to trigger the QCapture Pro operations. A Multifunction DAQ (Data acquisition board, NI PCI 6053E, National Instrument Inc.) was installed in the same image acquisition computer, and a BNC-2090 terminal was used to connect to the DAQ board. The timing program sent signals through the DAQ board. The signal for starting the flow went to a controller box, which included a relay to start the pump (Fig. 3.12). Fig. 3.13 shows a schematic of the timing sequence.

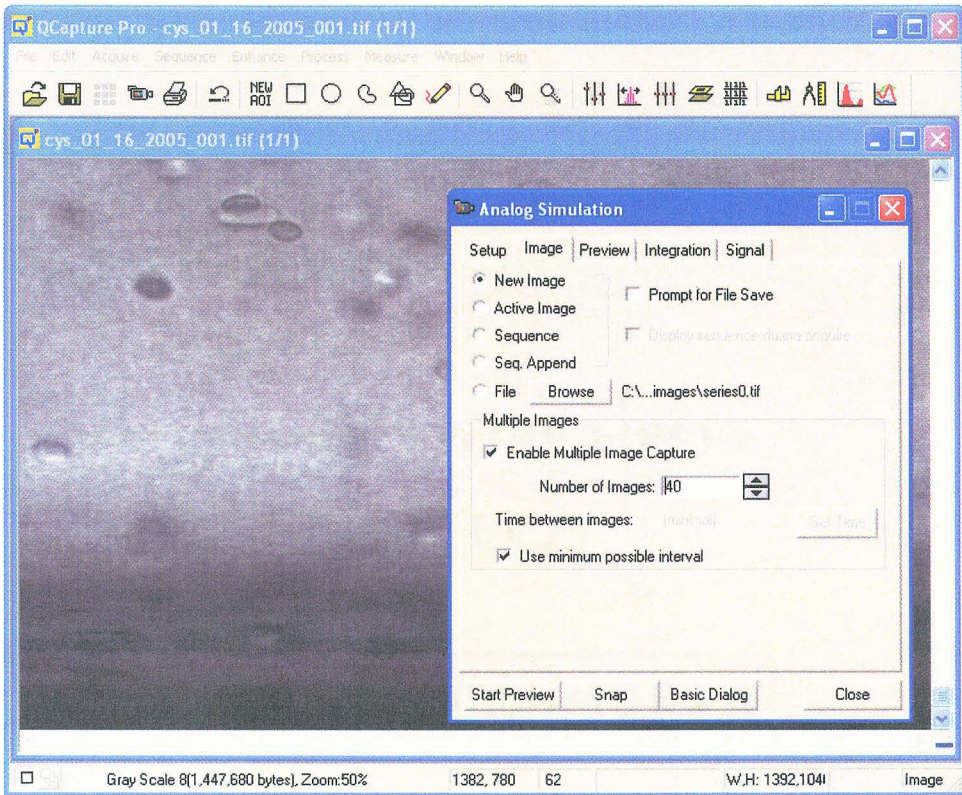


FIGURE 3.11 User interface of QCapture Pro

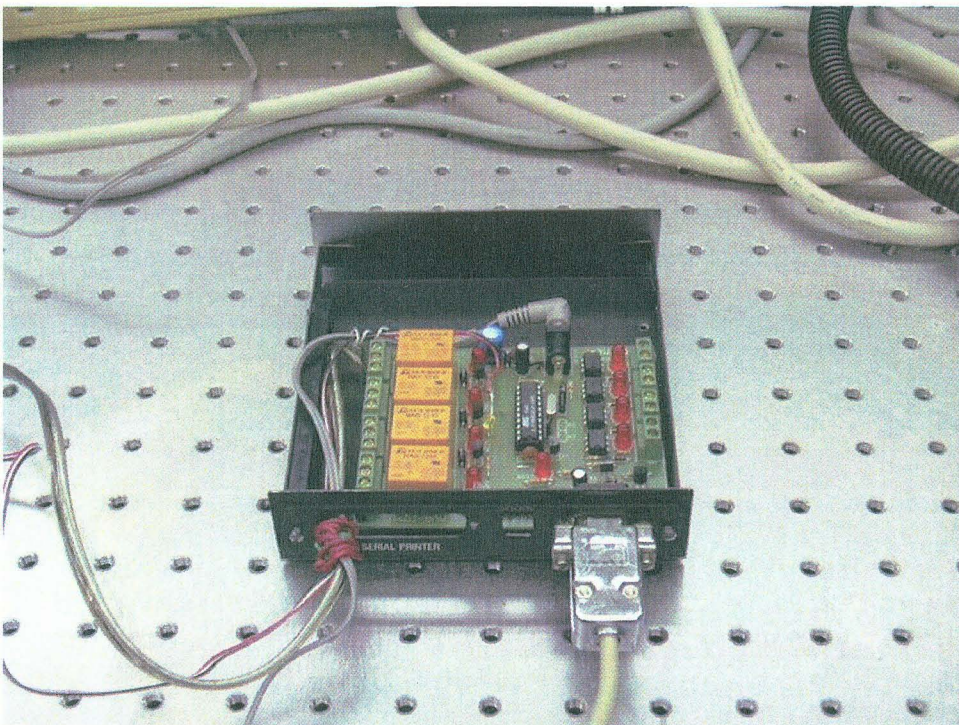


FIGURE 3.12 Controller box with relay

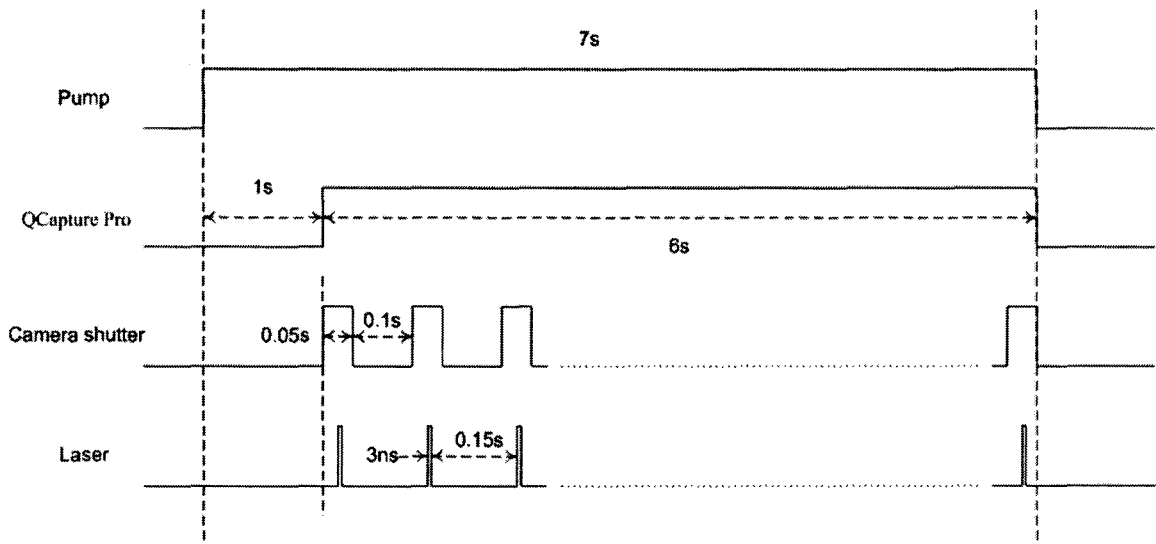


FIGURE 3.13 Schematic of timing sequence

Blood samples were obtained from the American Red Cross and the University Hospital Blood Bank. Red blood cells from seven different donors were compared, numbered as subjects S0-S6. For each experiment, a blood sample of about 2ml was enough to mix with up to 200 ml of dextran solution. Higher concentrations of blood would have reduced the visibility of the red cells in the images, and degraded the quality of the images. After each flow event, the solution for that run was discarded to ensure that the cells were sheared only once. Blood sample S0 was outdated and was tested 42 days after collection. All other samples, S1~S6, were less than 30 days from collection. All samples were anticoagulated with citrate at the time of collection. All experiments were performed at room temperature of about 24-25 °C. After each experiment run, a 10% Regular Clorox bleach solution was used to clean the flow system thoroughly.

The aspect ratio a/b of deformed cells was obtained by measuring the major radius a and the minor radius b of its image. For consistent measurements of cell

dimensions the outer edge of the cell boundaries were used. The shear stress to which it was exposed was determined by

$$\frac{\tau}{\tau_w} = 1 - \frac{y}{h/2} \quad (3.1)$$

where h is the width of the channel, y was the distance of the cell's centroid from the wall of the channel, and τ_w is the fluid shear stress at the wall. The shear stress on the wall is calculated with

$$\tau_w = \frac{2\mu v_0}{h/2} = \frac{3\mu \bar{v}}{h/2} \quad (3.2)$$

where μ is the Newtonian viscosity of the fluid, v_0 is the maximum velocity and \bar{v} is the average velocity of the flow through the channel. \bar{v} is obtained from the volume flow rate divided by the cross sectional area of the channel.

The duration of exposure to shear was estimated for each cell by

$$t = \frac{l}{v} \quad (3.3)$$

where l was the distance from the entrance of channel to the location where the cell was observed and v was the velocity of cell, which was estimated by

$$\frac{v}{v_0} = 1 - \frac{(h/2 - y)^2}{(h/2)^2} \quad (3.4)$$

Blood Damage Model

To facilitate the prediction of hemolysis from numerical solutions of flow fields in cardiovascular devices, an approximate mechanistic model based on cell membrane strain was developed. The model has three major components: 1) a relationship between fluid stresses and cell membrane tension, 2) a constitutive model relating membrane stress and strain, and 3) a strain threshold at which membrane rupture is predicted.

Fluid stress/membrane stress model – The deviatoric fluid stresses surrounding a single red cell were characterized by the local instantaneous values in a continuum

$$\begin{aligned}\tau_{x'x'} &= 2\mu \frac{\partial u}{\partial x'}, \quad \tau_{y'y'} = 2\mu \frac{\partial v}{\partial y'}, \quad \tau_{z'z'} = 2\mu \frac{\partial w}{\partial z'}, \\ \tau_{x'y'} &= \mu \left(\frac{\partial u}{\partial y'} + \frac{\partial v}{\partial x'} \right), \quad \tau_{y'z'} = \mu \left(\frac{\partial v}{\partial z'} + \frac{\partial w}{\partial y'} \right), \quad \tau_{x'z'} = \mu \left(\frac{\partial u}{\partial z'} + \frac{\partial w}{\partial x'} \right).\end{aligned}\tag{3.5}$$

for arbitrary orthogonal coordinate axes x' , y' , z' , velocities u , v and w and viscosity μ . The non-uniform distribution of fluid stresses around the cell was ignored. The six components of the stress tensor were transformed into three principal components $[\sigma_1, \sigma_2, \sigma_3]$. It was assumed for conditions approaching cell membrane rupture that the cell would be stretched into a prolate ellipsoidal shape, which has been observed in pure shear flow [Secomb 2003]. Deforming the cell to its isochoric ellipsoidal shape requires some initial externally applied stress τ_e that does not contribute to area dilation of the cell membrane. Beyond the isochoric limit, further elongation of the ellipsoid requires an increase in membrane surface area to contain constant volume of the cell. For estimation purposes, it was assumed that the major and two minor axes of the cell were aligned with the directions x , y and z of the three principal stresses components. Cell orientation differing from this assumption has been observed. For instance, for pure shear flow, the

major radius of modeled cells is approximately aligned with the first principle axis for low shear [Zhao & Sharp 1999], but has been shown to approach alignment with streamlines as shear increases [Secomb 2003]. The same behavior was observed in the current experiments. However, the expectation is that the order of magnitude scaling between membrane tension and fluid principle stresses will be the same. Fig. 3.14 shows the geometry and alignment of the red cell with major radius a and minor radii b and c .

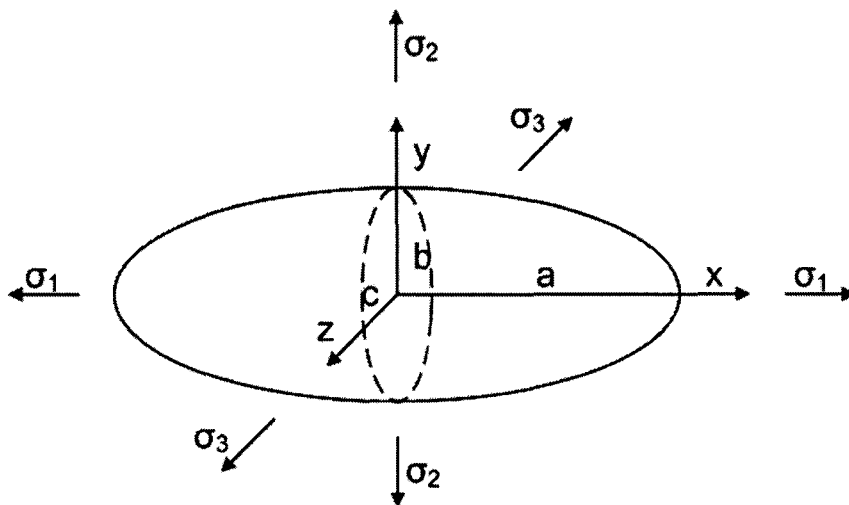
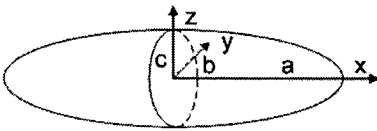
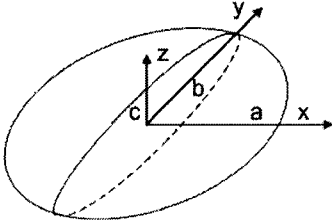
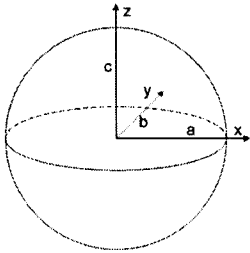


FIGURE 3.14 Geometry of the prolate ellipsoidal model of the red cell

The mass of the single red cell was estimated by $m = \rho V$, where density is $\rho \sim 1000 \text{ kg/m}^3$ and mass is $m \sim 10^{-13} \text{ kg}$. Its three components of acceleration $[\dot{v}_1, \dot{v}_2, \dot{v}_3]$ were defined in the three principal directions.

Hypothesized deformation patterns for the cells experiencing three-dimensional stresses are summarized in Table 3.2.

TABLE 3.2 Possible deformation patterns of red cell

Prolate		Oblate		Sphere	
$\sigma_1 \gg \sigma_2 \sim \sigma_3$	$\sigma_1 > 0, \sigma_2 > 0, \sigma_3 > 0$ $\sigma_1 > 0, \sigma_2 > 0, \sigma_3 < 0$ $\sigma_1 > 0, \sigma_2 < 0, \sigma_3 < 0$ $\sigma_1 < 0, \sigma_2 < 0, \sigma_3 < 0$	$\sigma_1 \sim \sigma_2 \gg \sigma_3$	$\sigma_1 > 0, \sigma_2 > 0, \sigma_3 > 0$ $\sigma_1 > 0, \sigma_2 > 0, \sigma_3 < 0$ (shockwave) $\sigma_1 > 0, \sigma_2 < 0, \sigma_3 < 0$ $\sigma_1 < 0, \sigma_2 < 0, \sigma_3 < 0$	$\sigma_1 \sim \sigma_2 \sim \sigma_3$	$\sigma_1, \sigma_2, \sigma_3 \sim 0$ (low stress for incompressible fluid) $\sigma_1, \sigma_2, \sigma_3 > 0$ (cavitation in compressible fluid)
$\sigma_1 \gg \sigma_2 \gg \sigma_3$	$\sigma_1 > 0, \sigma_2 = 0, \sigma_3 = -\sigma_1$ (shear flow)				
					

In practice, the oblate ellipsoidal shape, which occurs when there are two dominant positive principle stresses, is perhaps most relevant to the case of a shockwave field [Lokhandwalla & Sturtevant 2001] and is likely not important for most cardiovascular flows. The spherical shape, which occurs when all three principle stresses are of the same order, perhaps most frequently applies in the case of cavitation in a compressible fluid. The unstressed biconcave shape, which occurs when all stresses are small, is not of interest for hemolysis. The prolate ellipsoidal shape, which occurs when there is one dominant positive principle stress, may be the most common condition in cardiovascular flows. Even though the prolate ellipsoidal shape ostensibly requires $b \approx c$ and $\sigma_2 \approx \sigma_3$, this shape has been observed for pure shear flow, for which $\sigma_2 = 0$ and $\sigma_3 \approx -\sigma_1$. Therefore, the prolate ellipsoidal shape may occur for a wide range of hemolytic stress conditions and will be assumed in the development of the strain-based model.

To relate cell membrane tension to fluid stresses, dynamic force equilibrium was applied to half a prolate ellipsoidal cell in the dominant principle direction x (Fig. 3.15). T_1 is the average membrane tension on the circumference of the cross-sectional area, Δp is the pressure difference between internal and external fluids. $A_1 = \pi b^2$ is the cross-sectional area, and $L_1 = 2\pi b$ is the circumference of the cross-sectional area.

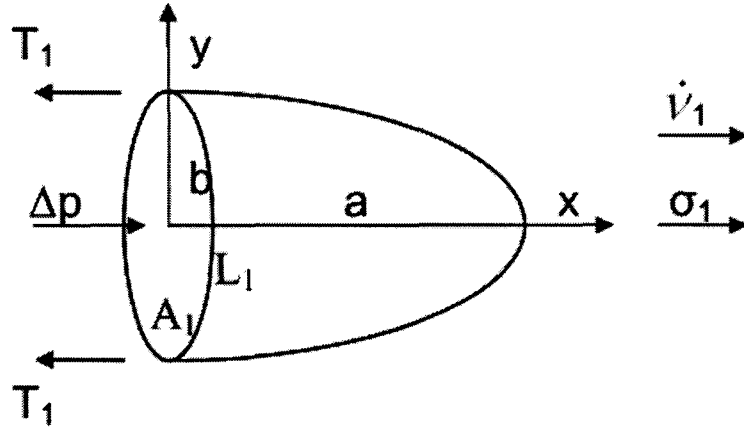


FIGURE 3.15 Free body diagram of the force equilibrium in the x direction

For the half cell, equilibrium in direction 1 is

$$\frac{m\dot{v}_1}{2} = (\sigma_1 + \Delta p) \cdot A_1 - T_1 \cdot L_1 \quad (3.6)$$

where m is the mass of the half cell and \dot{v}_1 is its acceleration in the x direction. By rearranging equation 6, membrane tension in direction 1 can be found as

$$T_1 = (\sigma_1 + \Delta p) \frac{A_1}{L_1} - \frac{m\dot{v}_1}{2L_1} \quad (3.7)$$

In this equilibrium equation, the stress threshold τ_e to reach the isochoric shape (Fig. 3.18) has been ignored, but will be added later.

In most cardiovascular flows, the inertial term is small relative to the membrane tension term. The criterion for neglecting the inertial term can be found with T_1 estimated from the critical membrane tension T_c of around 0.01 N/m, $m \sim 10^{-13}$ kg and $L_1 \sim 20 \mu\text{m}$, which gives $\dot{v}_1 \ll \frac{2T_1L_1}{m} \sim 4 \times 10^6 \text{ m/s}^2$. The maximum acceleration in physiologic cardiovascular flows is limited by the available pressure difference of about 200 mmHg. For inviscid flow, the maximum acceleration scales with $\dot{v}_{\text{max}} \approx \frac{1}{\rho} \frac{\Delta P}{\Delta x} = 27,000 \text{ m/s}^2$, where Δx is estimated as 1 mm. Nonphysiologic and externally driven flows, such as shock wave flow [Lokhandwalla & Sturtevant 2001] may produce higher acceleration. Without the acceleration term, equation 3.7 becomes

$$T_1 = (\sigma_1 + \Delta p) \frac{A_1}{L_1} = (\sigma_1 + \Delta p) \frac{\pi b^2}{2\pi b} = (\sigma_1 + \Delta p) \frac{b}{2} \quad (3.8)$$

To analyze equilibrium in the second and third principle directions, half of a differential slice in the plane of the second and third principle axes was taken from the elongated cell. Fig. 3.16 shows the free body diagram for force equilibrium in the z direction, with dx being the thickness of the differential element. The free body diagram for equilibrium in the y direction is similar.

The balance of forces in the y and z directions for the differential element are

$$2T_2 \cdot dx = (\sigma_2 + \Delta p)2b \cdot dx \quad \text{and} \quad 2T_3 \cdot dx = (\sigma_3 + \Delta p)2b \cdot dx \quad (3.9)$$

which can be simplified to

$$T_2 = (\sigma_2 + \Delta p)b \quad \text{and} \quad T_3 = (\sigma_3 + \Delta p)b \quad (3.10)$$

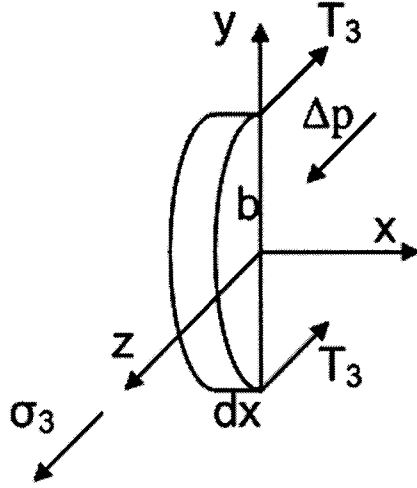


FIGURE 3.16 Free body diagram for the force equilibrium in the z direction

Defining $\xi_2 = \frac{T_2}{T_1}$ and $\xi_3 = \frac{T_3}{T_1}$, and combining equations 3.8 and 3.10 to eliminate Δp gives

$$\frac{2T_1 - T_2}{b} = T_1 \frac{2 - \xi_2}{b} = \sigma_1 - \sigma_2 \quad \text{and} \quad \frac{2T_1 - T_3}{b} = T_1 \frac{2 - \xi_3}{b} = \sigma_1 - \sigma_3 \quad (3.11)$$

Two average membrane tensions are defined as

$$\bar{T}_2 = \frac{T_1 + T_2}{2} \quad \text{and} \quad \bar{T}_3 = \frac{T_1 + T_3}{2} \quad (3.12)$$

which by inserting equation 3.11 can be expressed as

$$\bar{T}_2 = \frac{1 + \xi_2}{2 - \xi_2} \frac{b}{2} (\sigma_1 - \sigma_2) \quad \text{and} \quad \bar{T}_3 = \frac{1 + \xi_3}{2 - \xi_3} \frac{b}{2} (\sigma_1 - \sigma_3) \quad (3.13)$$

This part of the model can now be closed with an estimate for ξ . Ramanujan & Pozrikidis [1998] simulated the deformation of liquid capsules in simple shear flow and found the ratio of the two tensions in the mid-plane was about 3:1 to 4:1 (Fig. 3.17).

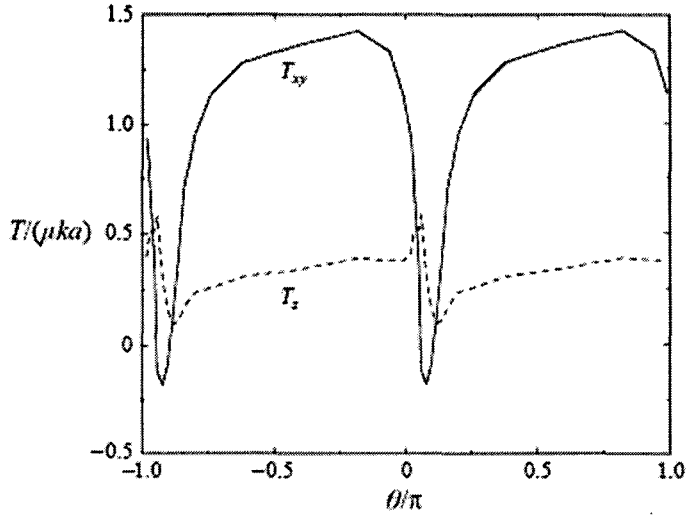


FIGURE 3.17 Membrane tensions of red cell from numerical simulation under simple shear flow [Ramanujan & Pozrikidis 1998] (T_{xy} represents tensions in the (x,y)-plane, and T_z represents tension perpendicular to the plane, along the z-axis)

To simplify the current problem, ξ was taken as $\xi = \xi_2 = \xi_3 \approx \frac{1}{3}$, which provides the two estimates of mean membrane tension

$$\bar{T}_2 = \frac{2b}{5}(\sigma_1 - \sigma_2) \text{ and } \bar{T}_3 = \frac{2b}{5}(\sigma_1 - \sigma_3) \quad (3.14)$$

Because $\sigma_1 \geq \sigma_2 \geq \sigma_3$ by convention, the second equation from 3.14 provides the largest mean membrane stress and therefore, the more conservative relationship for predicting hemolysis. Throughout the rest of the paper, the mean membrane stress will be taken as its maximum value $\bar{T} = \bar{T}_3$. The stress τ_e required to deform the cell to its isochoric ellipsoidal shape (Fig. 3.18) can be regarded as a threshold difference in major and minor axis stress, below which no area dilational stress is produced. By adding this threshold stress, equation 3.14 becomes

$$\bar{T} = \frac{2b}{5}(\sigma_1 - \sigma_3 - \tau_e) \quad (3.15)$$

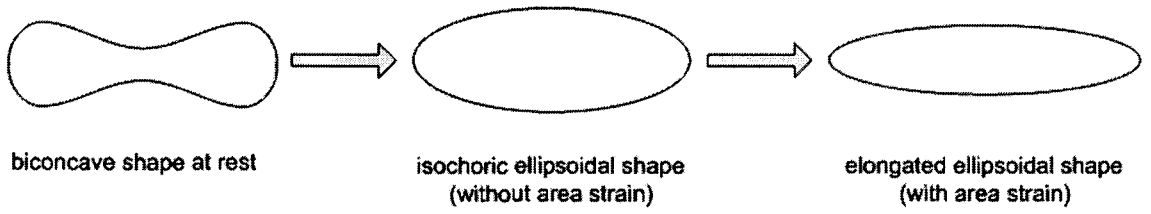


FIGURE 3.18 Schematic of stages of red cell's deformation

The local von Mises stress is given by

$$\tau_{vM} = \sqrt{\frac{(\tau_{x'x'} - \tau_{y'y'})^2 + (\tau_{x'x'} - \tau_{z'z'})^2 + (\tau_{y'y'} - \tau_{z'z'})^2 + 6 \cdot (\tau_{x'y'}^2 + \tau_{y'z'}^2 + \tau_{x'z'}^2)}{2}}, \quad (3.16)$$

$$= \sqrt{\frac{(\sigma_1 - \sigma_2)^2 + (\sigma_1 - \sigma_3)^2 + (\sigma_2 - \sigma_3)^2}{2}}$$

The scalar stress τ_s used in previous literature [Bludszuweit 1995] to model hemolysis is proportional to the von Mises stress, $\tau_s = \tau_{vM} / \sqrt{3}$. For pure shear flow, in which all fluid stresses are zero except for $\tau_{x'y'}$, the principle stresses become $\sigma_1 = \tau_{x'y'}$, $\sigma_2 = 0$, and $\sigma_3 = -\tau_{x'y'}$, and $\frac{\sigma_1 - \sigma_3}{2} = \tau_{x'y'} = \tau_s$. Thus for shear flow equation 3.15 can be written as

$$\bar{T} = \frac{4b}{5} (\tau_s - \tau_e) \quad (3.17)$$

This result allows convenient comparison with previous hemolysis models and applies for $\tau_s - \tau_e \geq 0$ for flows in which $|\sigma_2| \ll |\sigma_1|, |\sigma_3|$.

Starting with average unstressed red cell dimensions of mean volume $96 \mu\text{m}^3$ and mean surface area $130 \mu\text{m}^2$ [Fung 1993], and assuming that the cell is uniformly stretched into a prolate ellipsoid, Rand's [1964] area strain threshold for membrane

rupture of 6.4% is reached when the major radius is $a = 8.1 \mu\text{m}$ and the minor radius is $b = 1.7 \mu\text{m}$ (APPENDIX A).

Membrane constitutive relationship – The biaxial membrane tension causing area dilation has been modeled with a viscoelastic relationship [Evans & Hochmuth 1976 and Hochmuth, *et al.* 1979] $\hat{T} = \frac{T_1 + T_2}{2} - \mu_m \frac{(\lambda_1 - \lambda_2)^2}{4}$ (Chapter II), where \hat{T} was the biaxial tension causing area dilation of a cell surface, T_1 and T_2 are the principal tensions, λ_1 and λ_2 are the principal extension ratios for the deformation, and μ_m is the shear modulus. For the purpose of simplification, this viscous term was ignored. The consequence of this assumption is that biaxial tension may be overestimated in some cases. The remaining term yields a direct relationship between biaxial tension and the average membrane tension, i.e. $\hat{T} \sim \bar{T}$. Inserting this relationship into equation 3.17 gives

$$\hat{T} = \frac{4b}{5}(\tau_s - \tau_e) \quad (3.18)$$

An empirical blood damage model correlating the critical shear stress τ_{sc} with exposure time t was developed by Sharp & Mohammad [1998].

$$t \cdot (\tau_{sc} / 1500 - 1)^2 = 0.01 \quad (3.19)$$

This relationship fits the previous experimental data for the threshold of shear stress for different exposure times at which hemolysis begins. This model, which cannot describe the deformation of the red cell, provides a reference for the strain-based model.

The membrane area response was assumed to be viscoelastic with biaxial tension σ related to the area strain S and time duration t [Rand 1964]

$$\frac{1}{\hat{T}} = \frac{1}{ShY_2} + \frac{1}{ShY_1} \left(1 - \exp \frac{-Y_1}{\eta_1} t \right) + \frac{t}{Sh\eta_2} \quad (3.20)$$

By the same equation, the critical biaxial tension \hat{T}_c is related to the critical strain S_c and time duration t :

$$\frac{1}{\hat{T}_c} = \frac{1}{S_c h Y_2} + \frac{1}{S_c h Y_1} \left(1 - \exp \frac{-Y_1}{\eta_1} t \right) + \frac{t}{S_c h \eta_2} \quad (3.21)$$

where h is the membrane thickness, Y_1 and Y_2 are Young's moduli, and η_1 and η_2 are viscosities. This equation represents a Maxwell-Voigt model of membrane area response, in which the Voigt component - spring Y_1 and parallel dash-pot η_1 - is related to short term strain, and the Maxwell component - spring Y_2 in series with dash-pot η_2 - are related to long time response. The critical biaxial tension \hat{T}_c for lysis depends on time t . If $\hat{T} > \hat{T}_c$ for a particular duration of stress, then rupture of the red cell membrane is predicted.

In Rand's original article, model parameters were found to be $Y_1 \sim 4.3 \times 10^8$ dyn/cm², $Y_2 \sim 4.8 \times 10^8$ dyn/cm², $\eta_1 \sim 5.3 \times 10^7$ dyn·s/cm² and $\eta_2 \sim 1.1 \times 10^{11}$ dyn·s/cm² for an estimated membrane thickness of $h \sim 10^{-6}$ cm. Combining this thickness with the viscosities, $h\eta_1 \sim 53$ dyn·s/cm and $h\eta_2 \sim 1.1 \times 10^5$ dyn·s/cm. Evans and Hochmuth [Evans & Hochmuth 1976 and Hochmuth, *et al.* 1979], however, found the viscosity of the membrane surface to be $\eta_m = (6 \pm 2) \times 10^{-4}$ dyn·s/cm, about five and eight orders of

magnitude smaller than $h\eta_1$ and $h\eta_2$, respectively, and concluded that viscous flow in the membrane could not be responsible for the temporal dependence of membrane response in Rand's experiments.

The reason for the large differences in the viscosities interpreted from the two sets of experiments may lie in the comparison of the protocols. In Rand's experiments, a micropipette was used to aspirate part of the red cell into the bore, with the other part of the cell remaining outside the bore forming a sphere. The exposure time until the cell disappeared into the bore of the micropipette was recorded. In Evans and Hochmuth's experiments [1976], the cell was pulled in opposition by two micropipettes and then released. Cell dimensions and recovery time were measured as the cell returned to its biconcave shape. The recovery of red cell might involve the deformation of red cell without area strain. Sutura and Mehrjardi [1975] observed that cells began to lose their biconcavity at a stress of around 500 dyn/cm^2 and a majority of them became prolate ellipsoidal when the stress exceeded about 1500 dyn/cm^2 for an exposure time of 4 min. These fluid stress levels are associated with the range of membrane tension for which cells are deformed without area strain. The order of the involved membrane tension is estimated by $T \sim \tau \cdot a$, where T is membrane tension, τ is shear stress and a is major radius. Taking $\tau \sim 500 \text{ dyn/cm}^2$ and $a \sim 4 \text{ }\mu\text{m}$, T required to cause area strain is higher than about 0.2 dyn/cm . The recovery time t_c measured in Hochmuth's experiment was about 0.1 s . Therefore, the viscous component of membrane tension is of order $\eta_m/t_c = 6 \times 10^{-4} / 0.1 = 6 \times 10^{-3} \text{ dyn/cm}$, which is much smaller than the membrane tension needed to cause, or to resist recovery from, area strain during the recovery period. Therefore, the viscosity in the Evans and Hochmuth experiments [1976] was actually

related to isochoric deformation of the red cell, and not to the area expansion required to produce lysis.

The Young's moduli Y_1 and Y_2 in Rand's model [Rand 1964] were verified by Evans, *et al.* [1976], who found a simple linear relation between the isotropic tension in the membrane and the area expansion strain $\sigma = K \frac{\Delta A}{A}$, where ΔA is the increase in surface area, A is the original surface area, and K is the area expansion modulus. At room temperature, the value of K was 450dyn/cm with a standard deviation of about $\pm 15\%$ [Waugh & Evens 1979]. Converting to stress units with $hY_2 = K$ gives $Y_2 = 4.5 \times 10^8$ dyn/cm². Y_1 was comparable to Y_2 in Rand's experiments, $Y_1 \sim 4.3 \times 10^8$ dyn/cm², $Y_2 \sim 4.8 \times 10^8$ dyn/cm², and both are close to the Waugh & Evens value.

Hemolysis prediction threshold – Rand's [1964] area strain threshold for cell lysis was adopted. When a cell's area strain exceeded the critical strain S_c , membrane failure was predicted. Equation 3.20 can be rearranged and divided by S_c to solve for the normalized biaxial membrane strain

$$\frac{S}{S_c} = \hat{T} \left[\frac{1}{S_c h Y_2} + \frac{1}{S_c h Y_1} \left(1 - \exp \frac{-Y_1}{\eta_1} t \right) + \frac{t}{S_c h \eta_2} \right] \quad (3.22)$$

where $\frac{1}{S_c h Y_2} = 3.5 \times 10^{-2}$ cm/dyn, $\frac{1}{S_c h Y_1} = 3.9 \times 10^{-2}$ cm/dyn, $\frac{Y_1}{\eta_1} = 8 \text{ sec}^{-1}$, and

$$\frac{1}{S_c h \eta_2} = 1.5 \times 10^{-4} \text{ cm/dyn} \cdot \text{sec}.$$

An empirical constant α was introduced to adjust for several approximations utilized throughout the development of this model. Perhaps most importantly, α provides a means of accounting for minimal release of hemoglobin from cells whose ruptures heal quickly [Blackshears 1987]. The parameter α may also account for approximations in the fluid stress/membrane relationship, for instance the influence of tank-treading membranes, non-ellipsoidal cell shapes and cell orientations differing from the assumptions. Substituting α into equation 3.18, the biaxial membrane tension becomes

$$\hat{T} = \alpha \frac{4}{5} b(\tau_s - \tau_e) \quad (3.23)$$

Substituting equation 3.22 into equation 3.23 finally results in

$$\frac{S}{S_c} = \alpha \frac{4}{5} b(\tau_s - \tau_e) \left[\frac{1}{S_c h Y_2} + \frac{1}{S_c h Y_1} \left(1 - \exp \frac{-Y_1}{\eta_1} t \right) + \frac{t}{S_c h \eta_2} \right] \quad (3.24)$$

A reduced form of equation 3.24 was used for fitting the experimental results

$$\frac{S}{S_c} = \frac{4\alpha b}{5} (\tau_s - \tau_e) [C_0 + C_1(1 - \exp(-C_2 \cdot t)) + C_3 \cdot t] \quad (3.25)$$

where the critical strain S_c was taken as $S_c = 0.064$ [Rand 1964 and Blackshears 1987].

The other coefficients are $C_0 = \frac{1}{S_c h Y_2}$, $C_1 = \frac{1}{S_c h Y_1}$, $C_2 = \frac{Y_1}{\eta_1}$ and $C_3 = \frac{1}{S_c h \eta_2}$. Their

values were: $C_0 = 3.5 \times 10^{-2} \text{ cm/dyn}$, $C_1 = 3.9 \times 10^{-2} \text{ cm/dyn}$, and

$C_3 = 1.5 \times 10^{-4} \text{ cm/dyn} \cdot \text{sec}$. C_2 in original Rand's model was $C_2 = 8 \text{ sec}^{-1}$. But in this

work, α , τ_e and C_2 were used as curve fit parameters whose values were optimized to

fit previous hemolysis threshold data and the microscope images of deformed red cells.

Calibration of the model with images of deformed red cells – Applying the strain-based blood damage model, the predicted area strain S could be obtained from the shear stress τ and the exposure time t . To get a better prediction, the actual measured b value (minor radius) from the microscope image was applied.

In order to get the predicted aspect ratio a/b to compare with the measured aspect ratio a/b , a relationship which connected the area strain S of a red cell with its aspect ratio a/b was needed. Because the cell enclosed incompressible liquid, the cell's volume remained unchanged during the process of deformation. By assuming that the red cell was an ellipsoid shape, the cell's surface area could be calculated from the formula in APPENDIX A.

Given the volume and surface area of a red cell at rest, an excel table was built to show the relationship between ratio a/b and area strain S . For each given minor radius a , minor radius b could be calculated from the volume, and the surface area could be calculated from a and b . The corresponding area strain could be calculated from the surface area at deformation and the surface area at rest with $S = \frac{A - A_0}{A_0}$. Table 3.3 shows the example calculation for a red cell with volume $96 \mu\text{m}^3$ and mean surface area $130 \mu\text{m}^2$, in which area dilation equaled area strain $S + 1$. For mean cell volume of $V = 96 \mu\text{m}^3$ and unstressed surface area of $A_0 = 130 \mu\text{m}^2$ [Fung 1993], the unstressed aspect ratio can be found to be $a/b = 3.85$. For the hemolysis threshold strain of $S_c = 0.064$, the aspect ratio becomes 4.76.

TABLE 3.3 Aspect ratio a/b versus area strain

RBC volume, μm^3			96				
RBC area, μm^2			130				
volume/surface, μm			0.7538				
Prolate ellipsoid							
major radius a	minor radius b	a/b	eccentricity	volume	surface	volume/surface	area dilation (1+S)
7	1.8282	3.829	0.9653	98	129.8	0.7548	0.9987
7.0209	1.8255	3.846	0.9656	98	130	0.7538	1.0000
7.2	1.8026	3.994	0.9682	98	131.4	0.7458	1.0109
7.4	1.7781	4.162	0.9707	98	133	0.7370	1.0229
7.6	1.7545	4.332	0.9730	98	134.5	0.7284	1.0349
7.65	1.7488	4.374	0.9735	98	134.9	0.7263	1.0379
7.68	1.7454	4.4	0.9738	98	135.2	0.7250	1.0397
7.8	1.7319	4.504	0.9750	98	136.1	0.7201	1.0469
8	1.7101	4.678	0.9769	98	137.6	0.7120	1.0588
8.1	1.6995	4.766	0.9777	98	138.4	0.7081	1.0647

For convenience, the relationship between aspect ratio and strain was curve fit with good accuracy (Fig. 3.19).

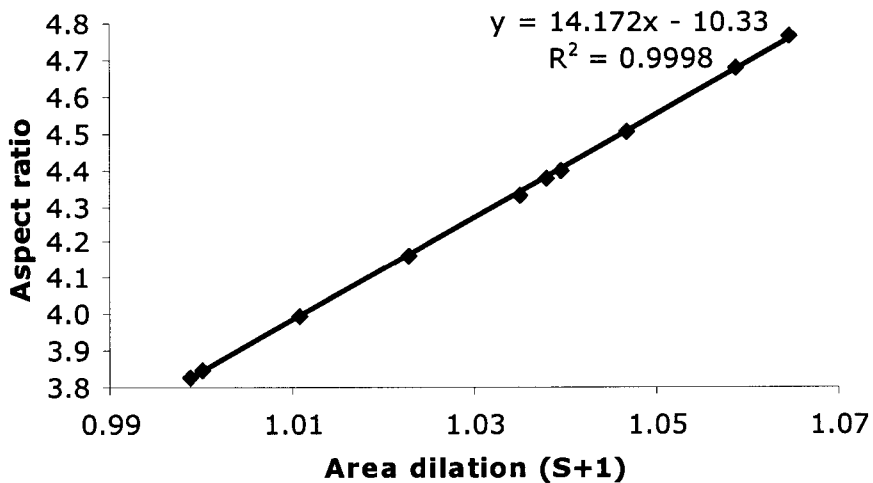


FIGURE 3.19 Aspect ratio a/b versus area strain

Erythrocyte volume and surface area exhibit Gaussian distributions within any given sample of blood [Fung 1993] and may vary among individuals. Moreover, cell dimensions depend on tonicity (osmolarity) [Fung 1993]. For instance, at 300 mosmol,

mean volume is $96 \mu\text{m}^3$ and mean surface area is $130 \mu\text{m}^2$, but at 217 mosmol, mean volume increases to $116 \mu\text{m}^3$ and mean surface area to $135 \mu\text{m}^2$. These differences, which were found to be significant in the blood samples used for these experiments, influence the relationship between aspect ratio and area strain for each cell. Because the experimental protocol did not provide a convenient way to measure unstressed dimensions of the particular cells for which images were captured, this problem was addressed by reducing the set of images analyzed to those of a narrow range of sphericity. Sphericity is defined as the actual surface area of the cell divided by the surface area of a sphere of the same cell volume and has a maximum value 1.0

$$Sph = \frac{4\pi}{(4\pi/3)^{2/3}} \cdot \frac{V^{2/3}}{A} \quad (3.26)$$

The average sphericity of red cells at 300 mosmol, for instance, is 0.79. It was observed that red cells with similar sphericity have similar coefficients in their relationship between a/b and S . The selection procedure for including images in the reduced set for each subject involved estimating unstressed sphericity for each cell imaged and then keeping those images within one standard deviation of the average sphericity. For example for subject S0, the estimated average sphericity of red cells was 0.85 with standard deviation of about 0.03, thus the images with estimated sphericity within the range $0.82 < Sph < 0.88$ were kept. The coefficients for the mean sphericity of 0.85 in the relationship between a/b and S were applied to the whole reduced data set for this subject.

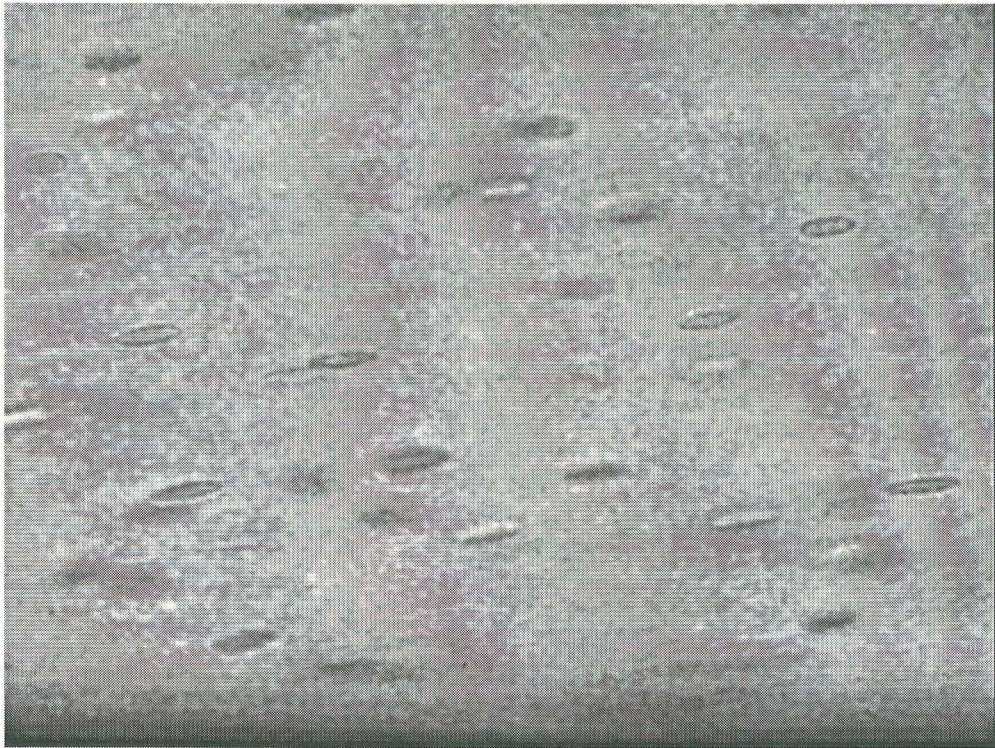
Predicted and measured a/b were compared. The sum of the square of the difference between predicted a/b and experimental a/b was calculated. A Visual Basic

macro program embedded in an excel file was written to do multiple regression to obtain optimum values of α , τ_e and C_2 that enabled the minimum value of the sum of square.

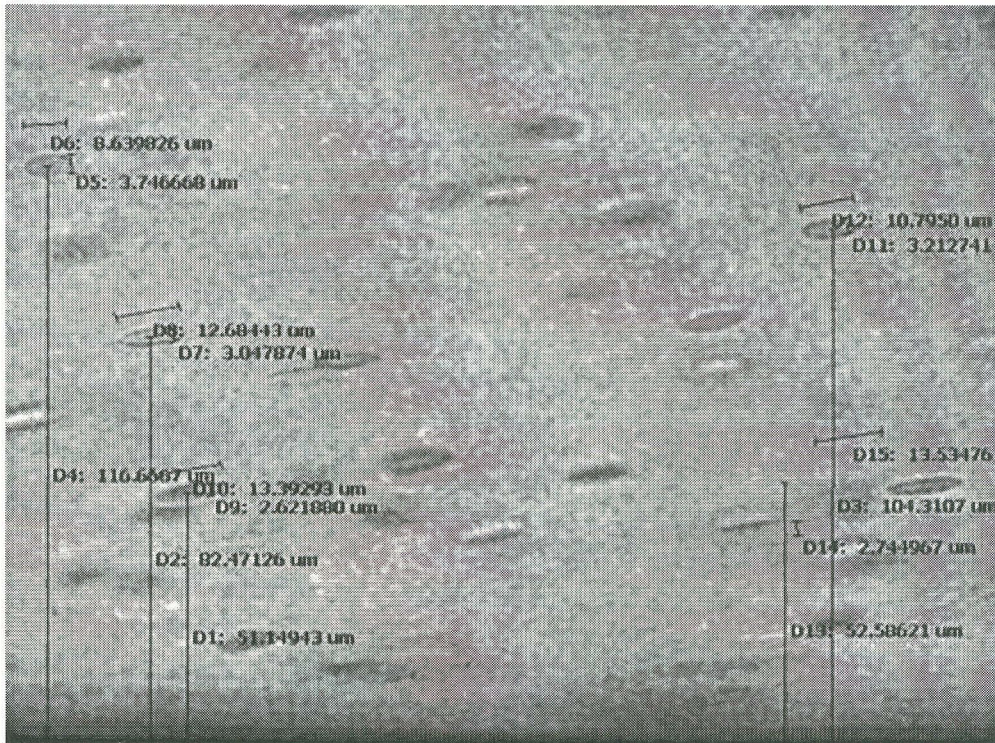
Results and Analysis

Example images are shown in Fig. 3.20. Cells in the focal plane of the objective lens, identifiable by high contrast boundaries, were measured. Fragmented cells, identified as those with abnormally small cross sectional areas, were ignored.

The orientations of the major axes of the elongated cells were different at the entrance region compared to the downstream region (Fig. 3.21). Fig. 3.21a shows that the orientations of cells were widely variable at the entrance. Fig. 3.21b shows that cells in the downstream flow were consistently aligned nearly parallel with the horizontal flow with their downstream ends pointed slightly upward (toward the center of the channel).

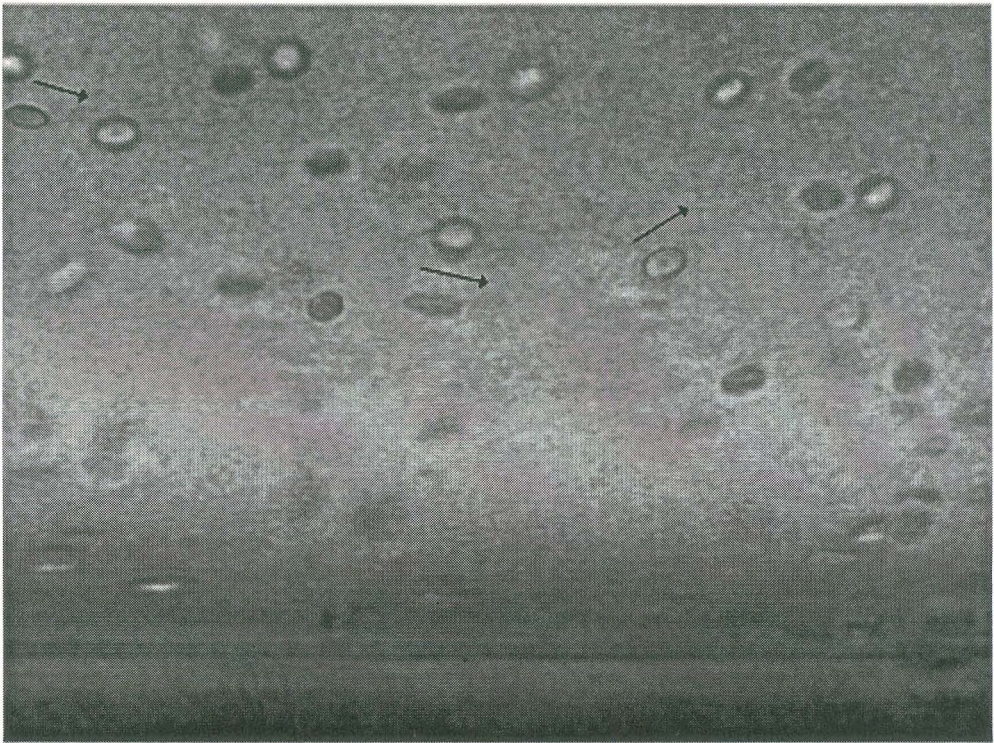


(a) Image of moving cells

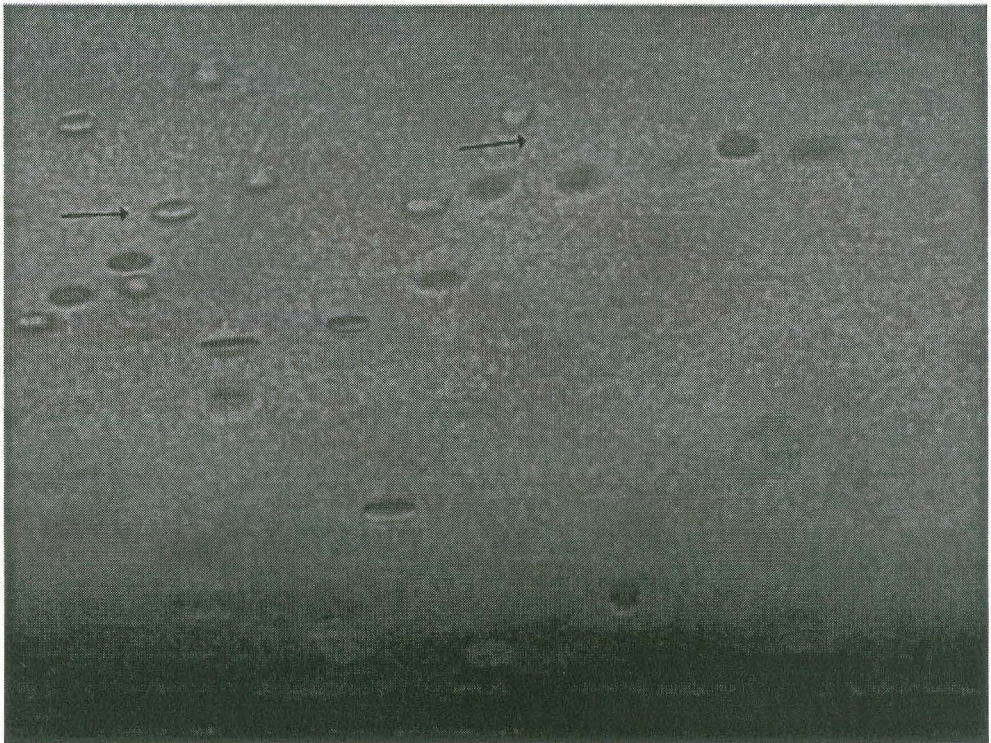


(b) Image of moving cells with scales

Figure 3.20 Picture of moving cells and scale



(a)



(b)

FIGURE 3.21 Orientations of stretched cells (a - orientations of cells in the entrance region, b - orientations of cells in the fully developed region)

The experimental specifications for the seven blood samples are shown in following Table 3.4:

TABLE 3.4 Experimental specifications

Subject	Duration ¹ (days)	Number of Cell Images	Fluid Viscosity (CP)	Average Velocity (m/s)	Field of View Location (mm)	Number of Frames
S0	>42	50	8.0	3.93	37.59	43
S1	24	83	11.1	3.38	36.26	65
S2	19	113	11.1	3.28	36.26	74
S3	18	88	11.1	3.27	36.26	57
S4	17	55	11.1	3.18	36.26	45
S5	17	91	11.1	3.25	36.26	60
S6	17	102	11.1	3.22	36.26	69
Note:	1. Time from collection date to date of experiment, in days.					

The blood sample from subject S0 was expired for clinical use, and was tested more than 42 days after collection. The other blood samples were not expired and were tested 24 days or less after collection. The number of frames chosen with clear cells' images and number of cells measured are also listed.

A 3D plot of aspect ratio versus shear stress and exposure time for subject S0 is shown in Fig. 3.22.

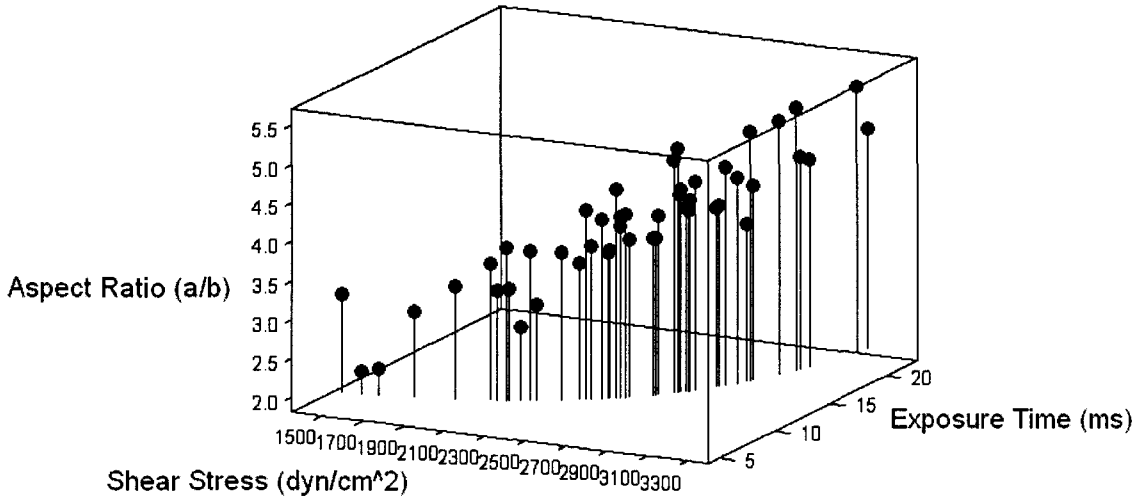


Figure 3.22 3D plot of aspect ratio versus shear stress and exposure time

From the above 3D plot, it is evident that the data points are projected along a diagonal with increasing shear stress and exposure time. The reason is that in this experiment, shear stress τ and exposure time t were not independent.

Rewrite equation 3.4 as $\frac{v}{v_0} = 1 - \left(1 - \frac{y}{h/2}\right)^2$, substitute equation 3.1 into it and

results

$$\frac{v}{v_0} = 1 - \left(\frac{\tau}{\tau_w}\right)^2 \quad (3.27)$$

By inserting equation 3.27 into equation 3.3, the exposure time becomes

$$t = \frac{l}{v_0 \left[1 - \left(\frac{\tau}{\tau_w}\right)^2\right]} = \frac{l}{v_0} \frac{1}{1 - \left(\frac{\tau}{\tau_w}\right)^2} \quad (3.28)$$

If the centerline exposure time is defined as $t_0 = \frac{l}{v_0}$ and substituted it into

equation 3.28, we obtain

$$\frac{\tau}{\tau_w} = \sqrt{1 - \frac{t_0}{t}} \quad (3.29)$$

which explicitly demonstrates the relationship between shear stress and exposure time for this data set.

The comparison between predicted and measured a/b is easier to see in 2D graphs. Figs. 3.23 and 3.24 show the comparison of predicted a/b with three optimized coefficients and experimental a/b . The optimum parameter values from multiple regression of all subject data were $\alpha = 39.01$, $\tau_e = 1200 \text{ dyn/cm}^2$ and $C_2 = 84 \text{ /sec}$. For comparison, a/b was also calculated with the strain-based model with Rand's original value of $C_2 = 8 \text{ /sec}$ and ignoring the threshold fluid stress to deform the red cell to a prolate ellipsoid, $\tau_e = 0 \text{ dyn/cm}^2$. For this model, the only remaining empirical parameter, α , was fit to a critical fluid stress of 1500 dyn/cm^2 for an exposure time of 2 min, which yielded $\alpha = 53$. Figs. 3.25 and 3.26 show the comparison of predicted a/b with the one-parameter model fit to a hemolysis threshold versus experimental a/b .

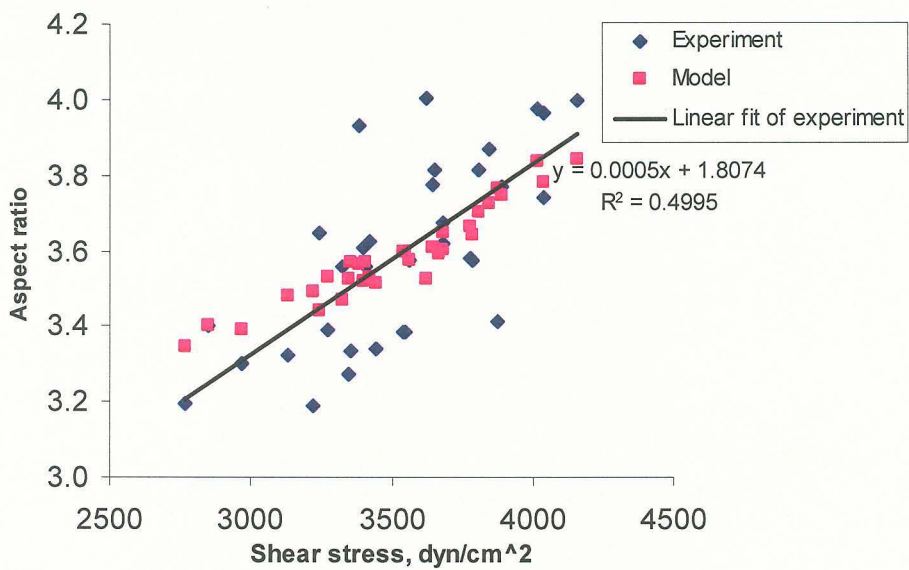


FIGURE 3.23 Comparison of predicted and measured aspect ratio versus shear stress with three optimized parameter values fit to cell image data

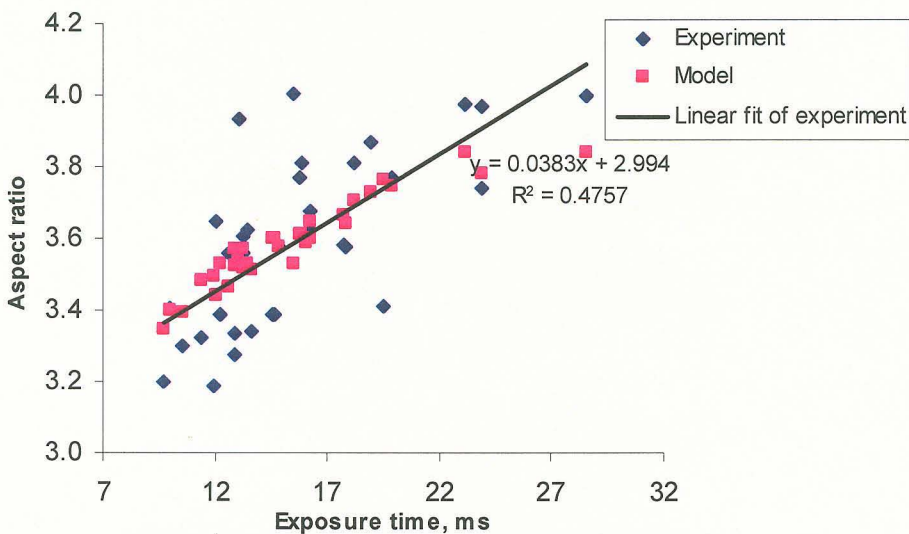


FIGURE 3.24 Comparison of predicted and measured aspect ratio versus exposure time with three optimized parameter values fit to cell image data

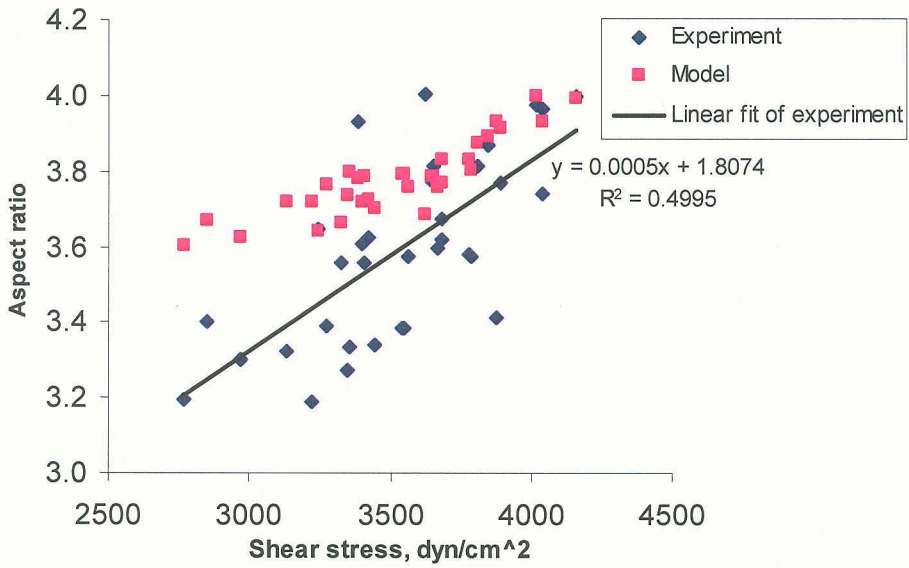


FIGURE 3.25 Comparison of predicted and measured aspect ratio versus shear stress with one parameter value fit to a hemolysis threshold

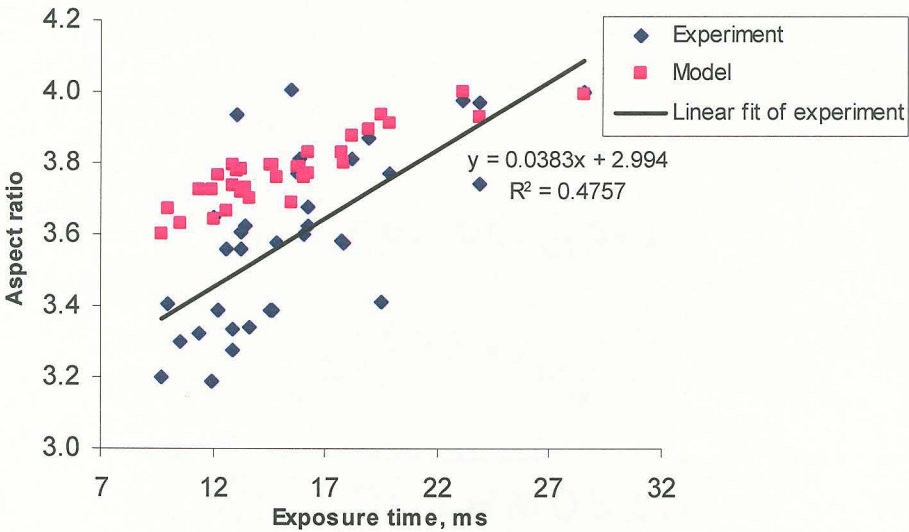


FIGURE 3.26 Comparison of predicted and measured aspect ratio versus exposure time with one parameter value fit to a hemolysis threshold

Fig. 3.27 shows the fit of the Sharp and Mohammad's empirical model [1998] (equation 3.19), the strain-based model (equation 3.25) with $\alpha = 39.01$, $\tau_e = 1200$ dyn/cm² and $C_2 = 84$ /sec and previous hemolysis thresholds. Fig. 3.27 shows that the strain-based model fit well with some previous hemolysis data, but it is obvious that the strain-based model can not be applied to exposure time less than 1 ms, there exists the large difference for exposure time of 10^{-5} s.

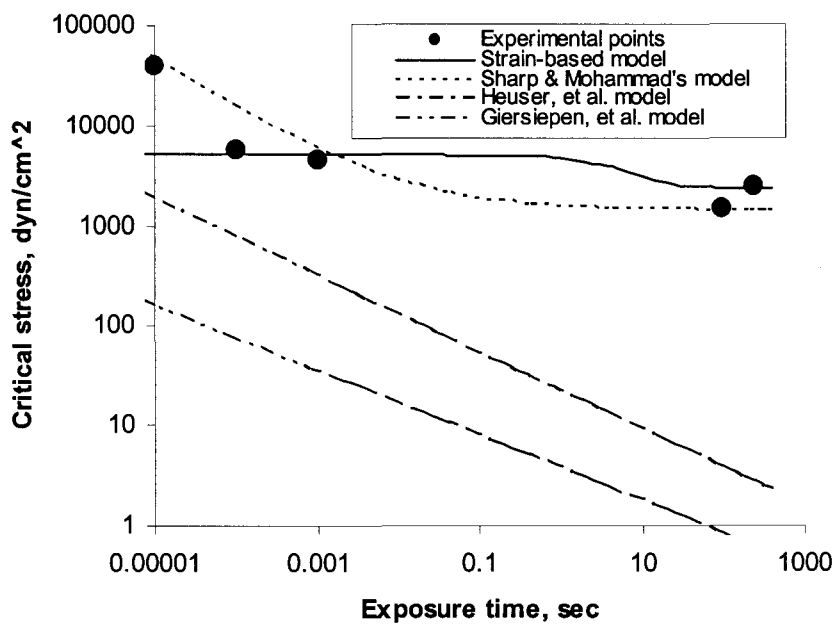


FIGURE 3.27 Comparison of hemolysis threshold models to data. (0.1% hemolysis was used for Heuser, *et al.* and Giersiepen, *et al.* models)

Discussion

The laser-illuminated micro imaging technique provides an effective, non-invasive method to capture and investigate the deformation of red cells by fluid stresses in high-speed flows. The strain-based blood damage model provides an estimate of flow-induced membrane area strain, which facilitates comparison of model predictions with experimental observations. In this study, data analyses of the images of deformed red cells were used to validate and optimize the coefficients of the strain-based blood damage model.

Figs. 3.23 and 3.24 show good fits of model predictions with data from microscope images. Compared to Fig. 3.25 & 3.26, in which the parameter values for the model were fit to previous hemolysis data only, the slope of the model prediction points was improved. The viscous term C_2 determined the characteristics of the fit related to the exposure time, in particular the slope of a/b versus stress and exposure time. The viscosity from Rand [1964] was $h\eta_1 = 53 \text{ dyn}\cdot\text{s}/\text{cm}$, and the viscosity from Hochmuth [1979] was $\eta_m = (6 \pm 2) \times 10^{-4} \text{ dyn}\cdot\text{s}/\text{cm}$, which was related to deformation rate of red cells without area strain. The viscosity from the optimized coefficient of this experiment is $5.05 \text{ dyn}\cdot\text{s}/\text{cm}$, an order of magnitude smaller than Rand's value and five orders of magnitude larger than that of Hochmuth, *et al.*

The C_3 term in the model is only related to long exposure time, and was an insignificant term for these experiments, which had a characteristic duration of 10 ms. This term could be ignored with little impact on the results.

The parameter τ_e has a relatively small influence on the fit, affecting primarily the magnitude of predicted a/b . The optimum value of $\tau_e = 1200 \text{ dyn}/\text{cm}^2$ is close the

threshold value for hemolysis of 1500 dyn/cm^2 for exposure times of 2 min. Compared to data collected from invasively acquired images, for which prolate ellipsoids were observed for shear stress as low as 500 dyn/cm^2 , this value may seem large. Perhaps τ_e may depend on exposure time. τ_e may be large for the short exposure times of these experiments, but smaller for the longer exposure times characteristic of the invasively acquired images.

α for the one-parameter model fit to a hemolysis threshold is close to the same value as that for the three-parameter model fit to images of deformed red cells. This similarity suggests that the mechanistic approach adopted in this study to relate cell membrane failure as a membrane strain limit has some validity.

The current strain-based model, however, does not fit well for short exposure times. In this regard, it is important to remember that Rand's cell membrane model included only springs and dash-pots. For shorter exposure time less than 1ms, a mass term might be necessary and significant. Similarly, the inertial term that was neglected in the equilibrium equations relating membrane tension to fluid stresses may become important for short exposures.

Some improvements that might be considered for future experiments include the following. First, it would be useful to measure unstressed cell surface area, so that the strain predicted by the strain-based model could be compared directly to the experimental measurements. Second, if multiple states of a single cell's deformation could be captured, it would have significant meaning for building future hemolysis prediction models and to the understanding of the stress/strain response of the cell membrane. Ideally, the shape of unstressed cell could be captured, and then the deformed shape of the same cell could be

captured at several later times. One way to implement such an improvement might be to use multiple exposures. However, the repetition rate of the laser pulses would need to be short. For instance, the delay of the second laser pulse would need to be about 0.1 ms to record two images in a field of view of 0.2 mm width for a flow velocity of about 2 m/s. To record multiple images over a distance of more than about 1 mm, multiple objectives and cameras might be necessary, which would increase the complexity and expense of the system, as well as the difficulty of synchronization.

In summary, since the strain-based blood damage model provides reasonable estimates of the deformation of red cells subjected to shear stress for exposure times typical of many cardiovascular flows, the suitability of the model for predicting membrane failure based on a threshold of membrane area strain will be tested in future studies of more complex flows in cardiovascular devices. This model has the potential to reduce the empiricism of hemolysis prediction.

CHAPTER IV

HEMOLYSIS PREDICTION IN THE BLOOD FLOW THROUGH HYPODERMIC NEEDLES

Purpose of Investigation

The membranes of red cells can be ruptured by fluid stresses in flows through hypodermic needles during venipuncture blood draws, hemodialysis and blood transfusions. Plasma-free hemoglobin released from damaged red cells interferes with a number of common clinical assays, causing a need for repeated blood draws to get accurate assays. Such repeated blood draws would increase patient discomfort, cost additional time and resources, and perhaps delay the diagnosis. Of some concern is that rates of significant hemolysis appear to be greater in emergency departments [Raisky, *et al.* 1994], where timely diagnosis can be particularly important. The threat of plasma-free hemoglobin also imposes limits on dialysis and transfusion flow rates. These limits are especially evident in pediatric transfusions, which must be accomplished through small-bore needles.

Experimental evaluation of hemolysis in any new cardiovascular device can require considerable time and resources for construction of prototypes suitable for flowing blood, development of protocols, and set up and execution of the experiments.

Experimental hemolysis testing also typically requires a number of repeated trials with different blood samples to obtain statistically significant results. With the advances in Computational fluid dynamics (CFD) technology and decreasing cost of high speed computing, analysis of flow in complex fluid systems has become feasible and increasingly convenient. Applying CFD technology to the analysis of complex flows has several potential advantages. Device designs could be evaluated and refined based on the computational results before construction of prototypes, thereby potentially reducing the time and cost associated with producing this hardware. In addition, computational techniques provide closed-form solutions that do not require repeated measurements to ensure statistical quality, which may also save time.

Directly simulating the motion and deformation of red cells in suspension is challenging for a number of reasons. First, the cell is influenced by local hydrodynamics, which includes both the external flow and cytoplasmic flow. These flows occur on a much smaller spatial scale than the bulk flow in typical cardiovascular devices, thereby increasing the size of the computational problem beyond what is currently reasonable for a design tool. Second, the cell membrane, which forms the boundary between the cells external and cytoplasmic flow domains, may experience large motion through the bulk flow domain, as well as the large motion and deformation relative to its own centroid by tumbling and tank-treading. Third, the stress/strain response of the membrane is nonlinear (viscoelastic) and is different for uniaxial versus area strain. Fourth, membrane response may be time dependent, associated with sublethal stress-induced damage accumulation similar to fatigue in engineering materials. Fifth, cell-to-cell interactions may be important in determining cell deformation in whole blood, in which the typical

volume fraction of cells is about 40%. Finally, intercellular bonds form red cell aggregates over time when fluid stresses are low, and are broken when stresses increase. Some simpler models that neglect many of these complexities have been studied. For instance, Li, *et al.* [1988] numerically simulated the large axisymmetric deformation of capsules with spherical, oblate, and prolate shapes subject to axisymmetric straining flow. The existence of a critical strain rate above which the capsule continues to elongate without reaching a steady asymptotic shape was established. Leyrat-Maurin & Barthes-Biesel [1994] simulated the motion of spherical capsules suspended on the axis of a hyperbolic constriction. The Mooney-Rivlin model was used to model the membrane of the capsule. Their results showed that the model could predict entrance or exit plugging in agreement with experimental observations when the modeled capsules were rigid enough. But for the motion of red cells, a more accurate constitutive relationship of membrane stress and strain such as that developed by Evans & Hochmuth [1976] may be necessary. Pozrikids [2003] and Ramanujan & Pozrikids [1998] numerically simulated the flow-induced three-dimensional deformation of red cells or other liquid capsules under simple shear flow, in which the red cells were modeled as deformable liquid capsules enclosed by an elastic membrane resistant to shear and bending deformation. The numerical results for the period of overall rotation of capsules showed good agreement with the experimental observations of Goldsmith & Marlow [1972] of red cells suspended in plasma. Li, *et al.* [2005] numerically simulated the 3D whole-cell equilibrium shape and deformation of red cell with spectrin-level energetics. They simulated the direct stretching by optical tweezers of the cell from an initial equilibrium shape. While significant progress has been made in simulating deformation of modeled

cells, considerable work remains to approach fully resolved multi-phase whole blood flows. Therefore, in the interim, continuum-based models of blood damage may be useful.

Several empirical blood damage models have been reported that used CFD-generated fluid stress fields to predict hemolysis. Blood damage models of Heuser, *et al.* [1980] and Giersiepen, *et al.* [1990] were based on a power-law of the form $IH = A\tau\alpha t^\beta$, where IH is the index of hemolysis, τ and t represent shear stress and exposure time, respectively. They are convenient to use, but they remain purely empirical models. The model coefficients are empirically determined by regressing experimental data, which requires that both the shear stress and exposure time be independently controllable in the experiment. The strain-based blood damage model was developed in Chapter III that provides the capability to estimate the strain and deformation of red cells under fluid stress, and is also amenable for use in the CFD analysis of hemolysis.

In experiments conducted at the University of Louisville, new needle designs with modified entrance geometry were evaluated for their potential to reduce flow-induced red cell damage. Hemolysis from three groups of 16 gauge needles – one standard group with sharp entrance, another with beveled entrance and a third with rounded entrance – was compared. Plasma-free hemoglobin was measured with a spectrophotometric method.

In this paper, CFD was used to simulate the flow through three types of 16 gauge needles: a standard needle with sharp entrance, two modified needles with beveled and rounded entrances. The three red blood cell damage models introduced above were then applied to predict hemolysis in the three needle types, and results were compared to

experiments. The analysis process included up to four main steps. The first step was to create solid models of the needles, import the solid models into the pre-processing tool GAMBIT to create the geometry of needle and generate the grids of simulation. The second step was to calculate flow fields with FLUENT. The third step was to extract the stress distribution along sampled streamlines, which was accomplished by releasing virtual tracking particles from points distributed over the outlet of flow in reverse direction to the inlets. Finally the strain-based blood damage model [Chen & Sharp 2006] and the power-law blood damage models of Heuser, *et al.* [1980] and Giersiepen, *et al.* [1990] were applied to the time histories of scalar stress along each streamline to predict the amount of hemolysis for each model.

CFD Simulations

The geometries of three needles were created by 3D CAD tool Solid Edge V13.

Fig. 4.1 shows, for example, the geometry of standard needle.

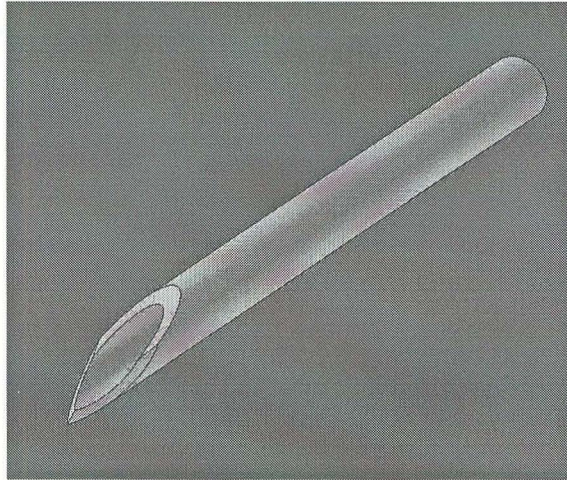
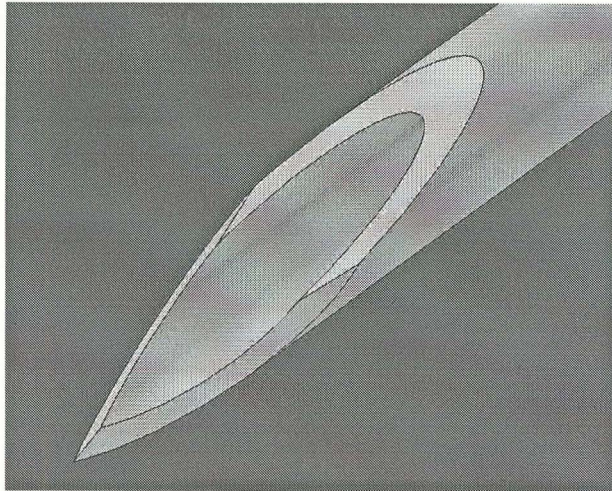
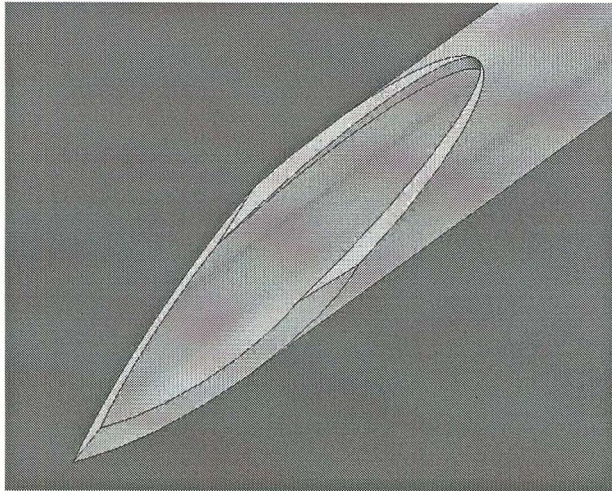


FIGURE 4.1 CAD geometry of standard needle

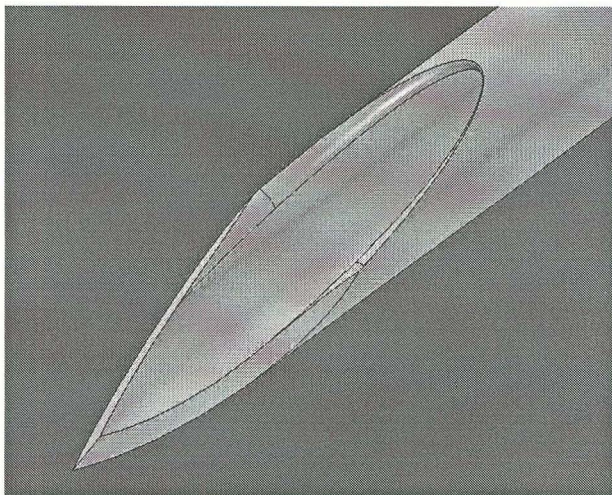
Fig. 4.2 close-ups of the geometries of the tips of the standard, beveled and rounded needles. The standard needle has an opening formed by a primary bevel that defines the angle of the opening with respect to the axis of the bore, and two secondary bevels on the upstream half of the opening for further sharpening the tissue-piercing point. The primary bevel creates a sharp downstream edge that causes high fluid stresses in blood passing by it. The beveled needle is modified with a chamfered edge around the downstream edge of the entrance, and the rounded needle is modified with a rounded downstream edge.



Standard needle



Beveled needle



Rounded needle

FIGURE 4.2 CAD geometries of the tips of 3 needles

All needles are 16 gauge stainless steel needles with inner diameter D_i of 1.219 mm and outer diameter D_o of 1.651 mm. The primary bevel angle was 14° for each. The full length of each needle was 45.19 mm (from the sharp tip to the exit end). The CAD geometries of needles were imported into GAMBIT to generate computational grids. FLUENT v6 was used to simulate the flow field.

A Newtonian fluid of density $\rho = 1050 \text{ kg/m}^3$ and viscosity $\mu = 0.0035105 \text{ kg/m}\cdot\text{s}$ (i.e. 3.51 cP) was drawn through the needles. A pressure drop of 44817.5 Pa (6.5 psi) was applied between the entrance and the exit of the needles. The tip of needle was surrounded by a virtual brick domain of 3 mm x 9 mm x 1.5 mm, in which filled blood flow was drawn into the needle through the entrance of needle. On the faces of the brick domain, pressure inlet conditions were applied. Because the geometry was symmetric about the mid plane, only half of the needle is simulated. Fig. 4.3 shows the schematic of the initial computational domain for the standard needle.

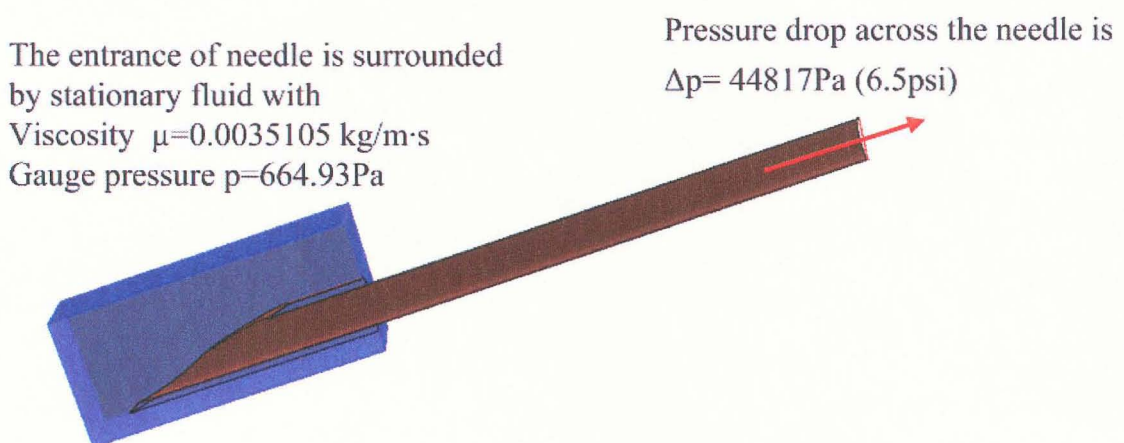


FIGURE 4.3 Schematic of the initial computation domain for the standard needle

Initially, a coarse grid and laminar flow assumption were applied to simulate the full length 45.19 mm of needle to get the average velocity through each type of needle (Table 4.1). The Reynolds number was calculated by $Re = \frac{\rho \bar{V} D_i}{\mu}$. All the Reynolds numbers are less than 2400, verifying the laminar flow assumption. Note that the velocities are slightly higher in the modified needles than the standard needle, reflecting the easing of the transition into the bore of the needle.

TABLE 4.1 Average velocity through the needles

Needle	Average Velocity \bar{V} (m/s)	Reynolds number Re
Standard Needle	3.041	1109.0
Beveled Needle	3.252	1185.8
Rounded Needle	3.343	1219.1

Subsequently, fine grids were used to simulate a shorter 24.88 mm length of needle with a velocity boundary condition at its exit. This length of needle, which was verified to approach fully developed flow at its exit in the preliminary simulations, enabled the application of higher resolution in the remaining grid. About 790,000 cells were used in these simulations. Fig. 4.4 shows the schematic of part of grids of standard needle. Convergent steady solution was obtained when relative errors of pressure and velocity components less than 10^{-7} .

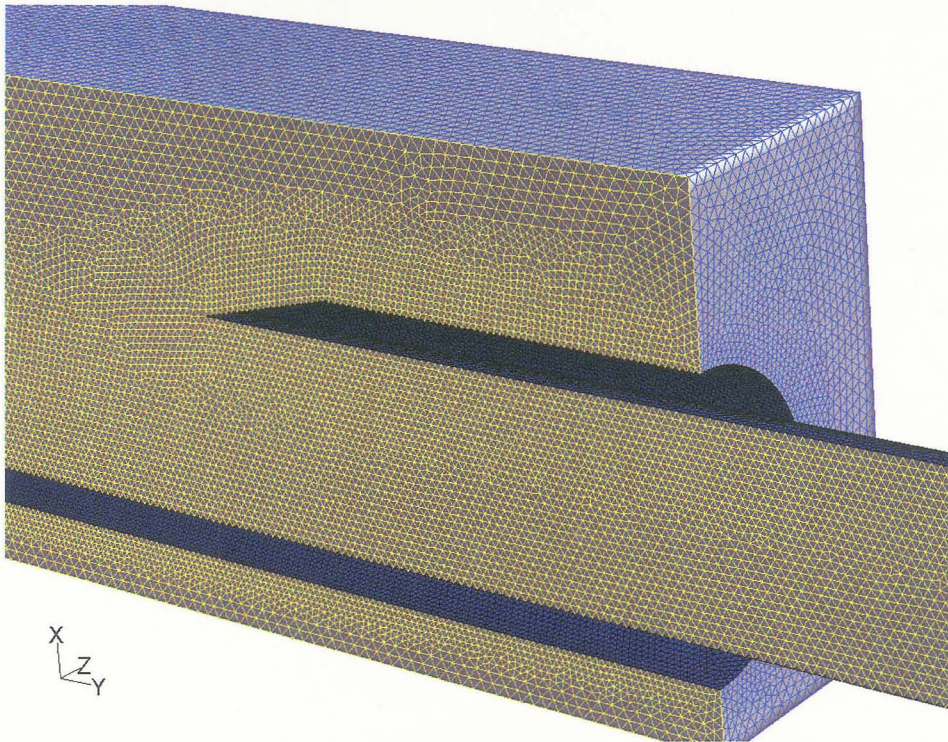


FIGURE 4.4 Schematic of part of the computational grid for standard needle

The incompressible, steady state, Newtonian, laminar flow was solved with 3D Navier-Stokes equations in FLUENT:

$$\frac{\partial u}{\partial x} + \frac{\partial v}{\partial y} + \frac{\partial w}{\partial z} = 0 \quad (4.1)$$

$$\rho \left(u \frac{\partial u}{\partial x} + v \frac{\partial u}{\partial y} + w \frac{\partial u}{\partial z} \right) = -\frac{\partial p}{\partial x} + \mu \left(\frac{\partial^2 u}{\partial x^2} + \frac{\partial^2 u}{\partial y^2} + \frac{\partial^2 u}{\partial z^2} \right) \quad (4.2)$$

$$\rho \left(u \frac{\partial v}{\partial x} + v \frac{\partial v}{\partial y} + w \frac{\partial v}{\partial z} \right) = -\frac{\partial p}{\partial y} + \mu \left(\frac{\partial^2 v}{\partial x^2} + \frac{\partial^2 v}{\partial y^2} + \frac{\partial^2 v}{\partial z^2} \right) \quad (4.3)$$

$$\rho \left(u \frac{\partial w}{\partial x} + v \frac{\partial w}{\partial y} + w \frac{\partial w}{\partial z} \right) = -\frac{\partial p}{\partial z} + \mu \left(\frac{\partial^2 w}{\partial x^2} + \frac{\partial^2 w}{\partial y^2} + \frac{\partial^2 w}{\partial z^2} \right) \quad (4.4)$$

where ρ is density, μ is viscosity, p is pressure, and (u, v, w) are flow velocity components in the three coordinate directions (x, y, z) . The Energy equation was ignored because the temperature was treated as constant.

The three-dimensional resultant stress is characterized by the von Mises stress,

$$\tau_{von} = \sqrt{\frac{(\tau_{xx} - \tau_{yy})^2 + (\tau_{xx} - \tau_{zz})^2 + (\tau_{yy} - \tau_{zz})^2 + 6 \cdot (\tau_{xy}^2 + \tau_{yz}^2 + \tau_{xz}^2)}{2}}, \quad \tau_{xx} = 2\mu \frac{\partial u}{\partial x},$$

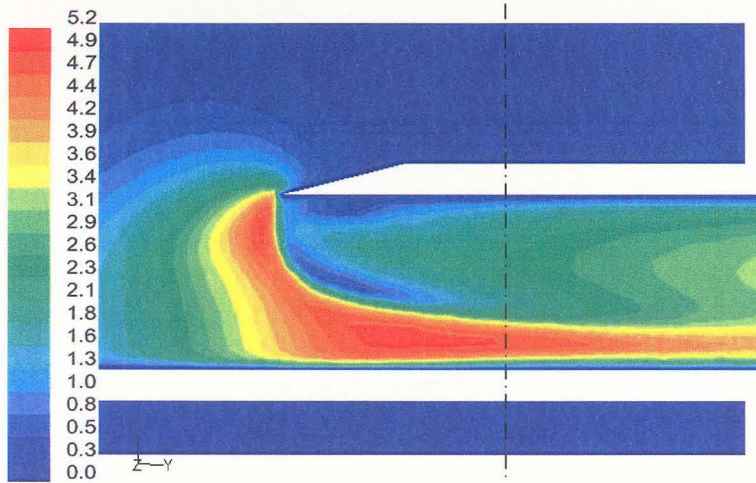
$$\tau_{yy} = 2\mu \frac{\partial v}{\partial y}, \quad \tau_{zz} = 2\mu \frac{\partial w}{\partial z}, \quad \tau_{xy} = \mu \left(\frac{\partial u}{\partial y} + \frac{\partial v}{\partial x} \right), \quad \tau_{yz} = \mu \left(\frac{\partial v}{\partial z} + \frac{\partial w}{\partial y} \right), \quad \tau_{xz} = \mu \left(\frac{\partial u}{\partial z} + \frac{\partial w}{\partial x} \right).$$

The scalar stress τ_s used in previous literature [Bludszuweit, 1995] to model hemolysis is proportional to the von Mises stress, $\tau_s = \tau_{von} / \sqrt{3}$, for pure shear flow, in which all fluid stresses are zero except for $\tau_{x'y'}$, the scalar stress becomes $\tau_s = \tau_{x'y'}$.

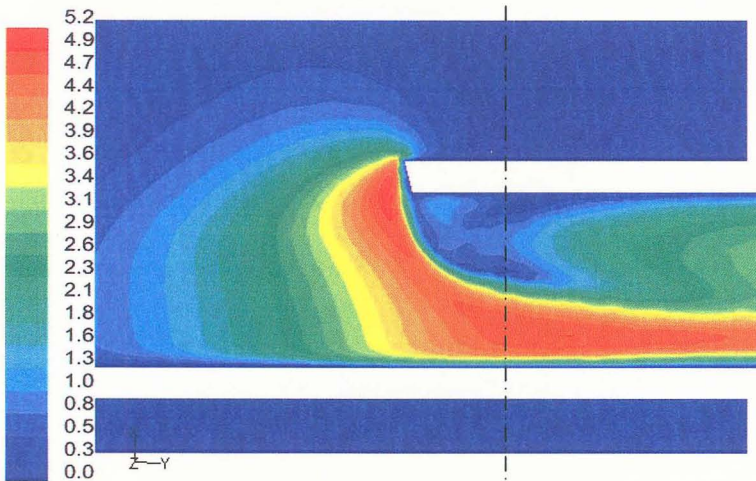
Figures 4.5 and 4.6 show the contour plots of velocity magnitude and scalar stress near the entrance of each of the three types of needles.

The contour plots of velocity magnitude show the differences in the size and location of the vortex near the entrance.

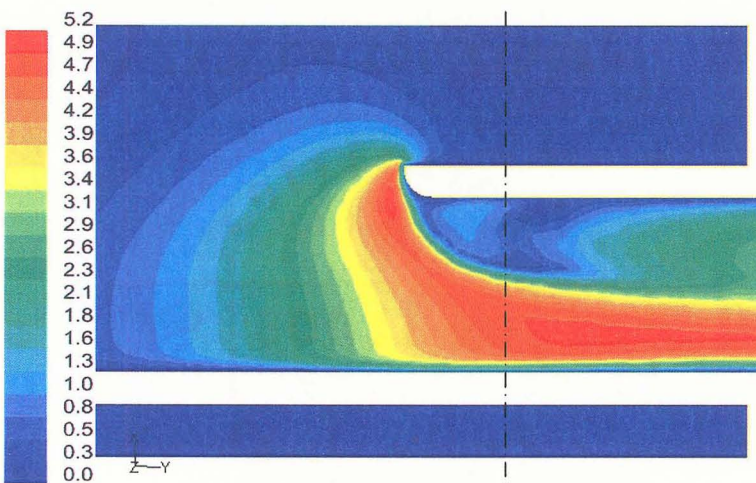
Figures 4.7 and 4.8 show the contour plots of y-velocity and τ_s of the flow on the cross-section plane at 7 mm from the tip for three kinds of needles, which is shown as a dash line in Figure 4.5.



Standard needle

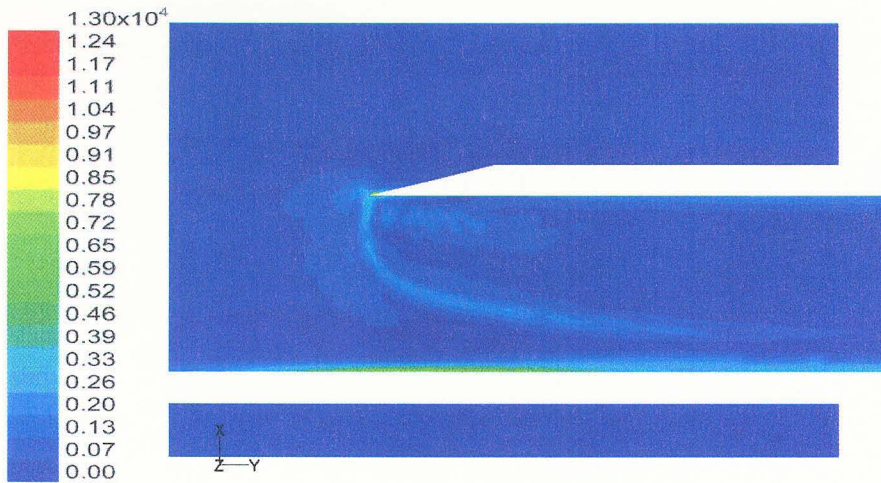


Beveled needle

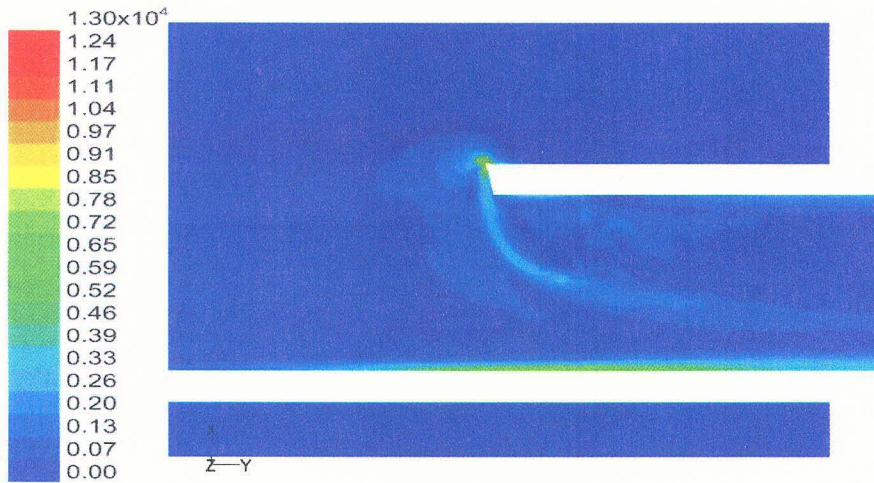


Rounded needle

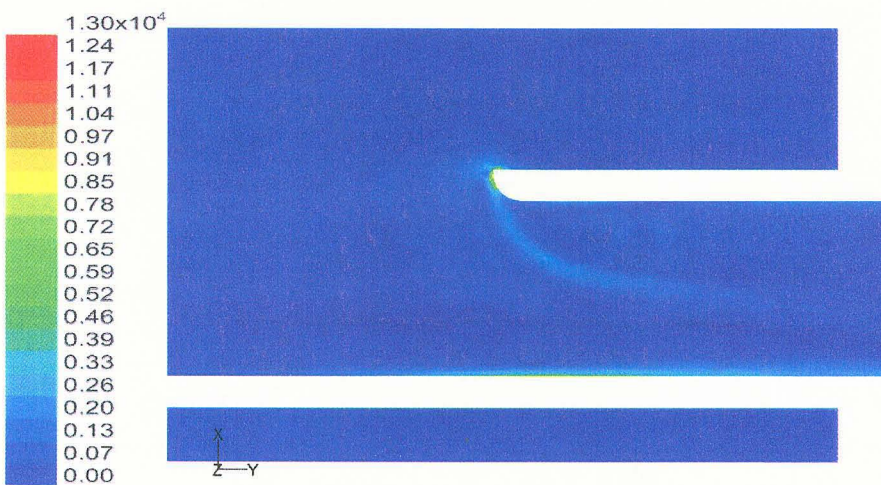
FIGURE 4.5 The contour plots of velocity magnitude (m/s) on the symmetric mid-plane



Standard needle

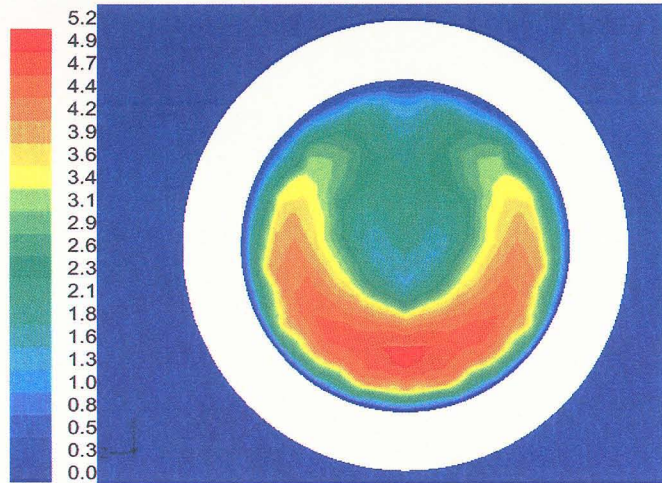


Beveled needle

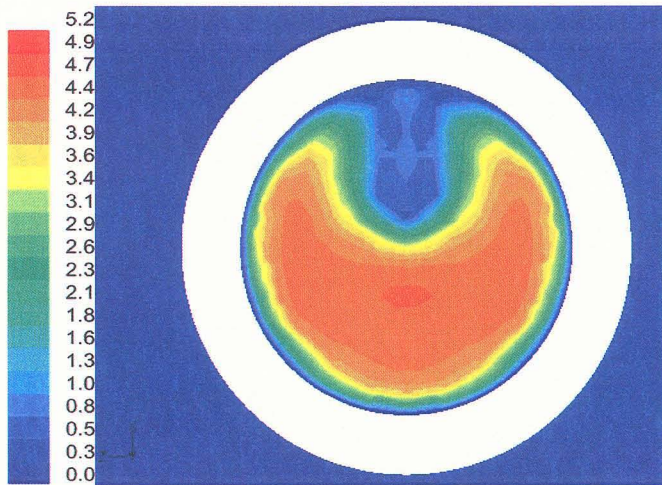


Rounded needle

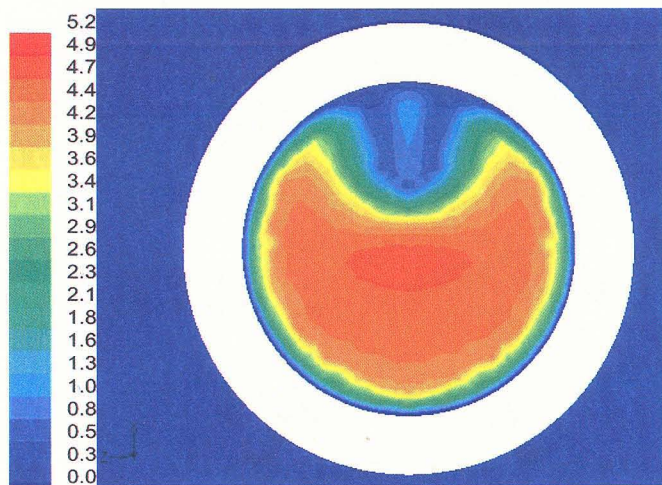
FIGURE 4.6 The contour plots of τ_s (dyn/cm²) on the symmetric mid-plane



Standard needle

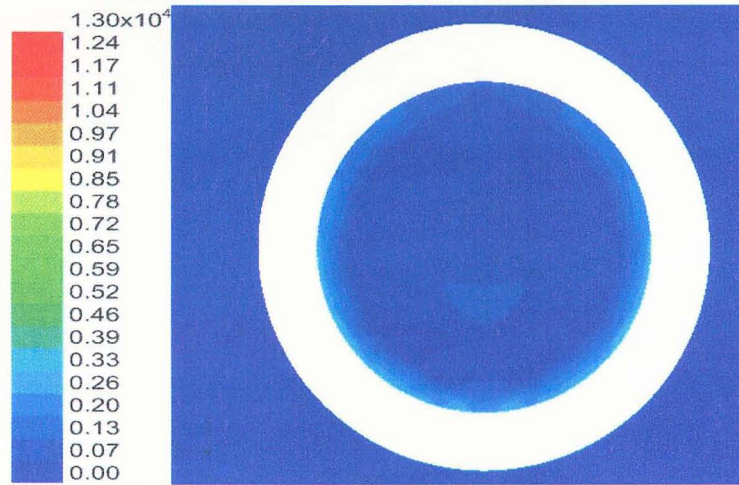


Beveled needle

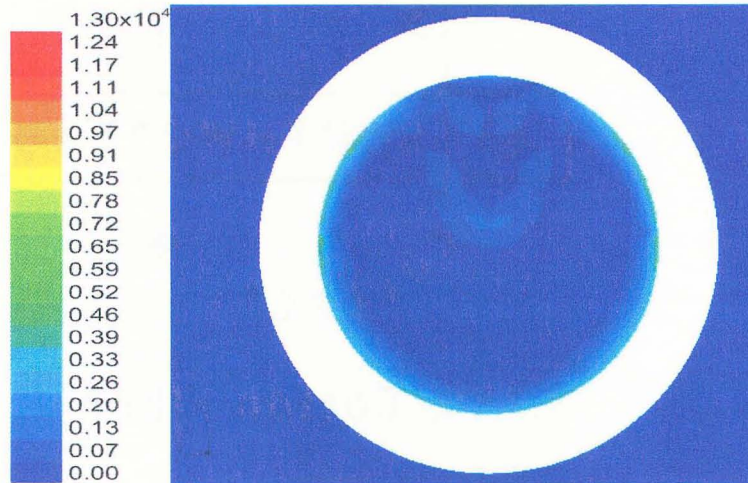


Rounded needle

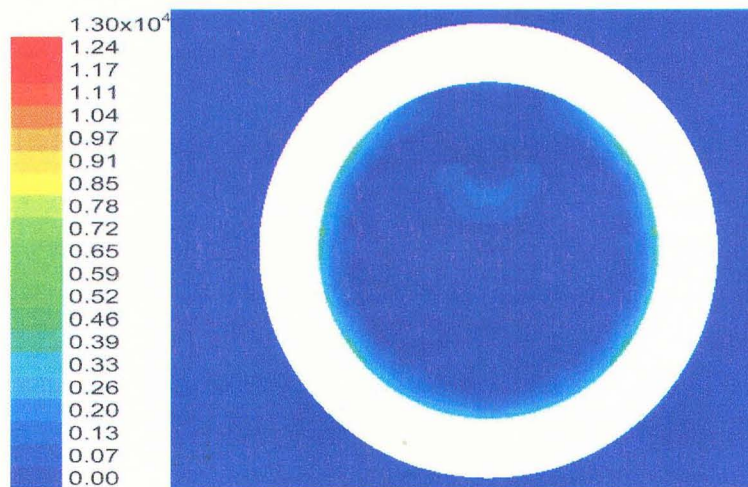
FIGURE 4.7 The contour plots of velocity magnitude (m/s) on cross-section plane



Standard needle



Beveled needle



Rounded needle

FIGURE 4.8 The contour plots of τ_s (dyn/cm²) on cross-section plane

Because the flow is steady, the pathline of an arbitrary particle in the flow is the same as the streamline through the same position. From the CFD solution of the velocity field, a grid of stream-tubes filling the flow cross section was defined and the time histories of τ_s along streamlines central to each streamtube were extracted. To facilitate the sampling process, the starting sample points were located on the circular cross section of the needle exit (Fig. 4.9), and tracked upstream to the entrance.

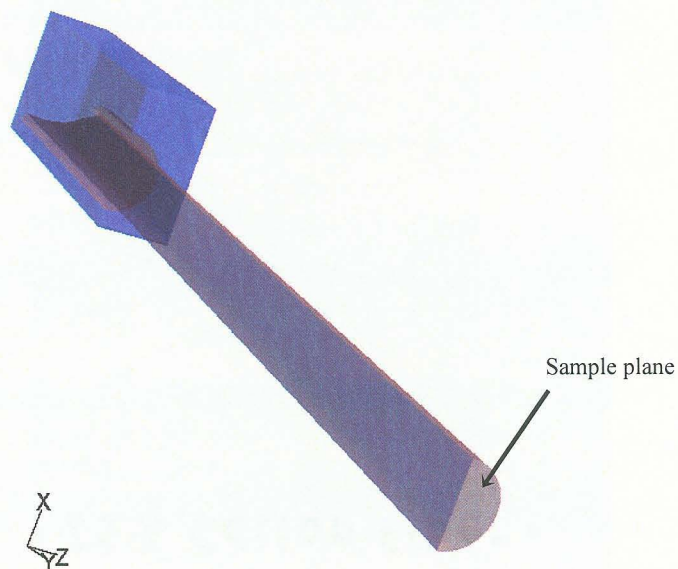


FIGURE 4.9 Schematic of the sample plane

The sample points are uniformly distributed in the x and z directions across the exit flow cross section. Fig. 4.10 shows a schematic of the location of the sample points (not all points are shown), as well as example streamlines. To predict the small value of hemolysis, about 48000 sample points were used inside the half cross section. To evaluate the effect of discretization error, another set of sample streamtube of about 12000 sample points was used for comparison.

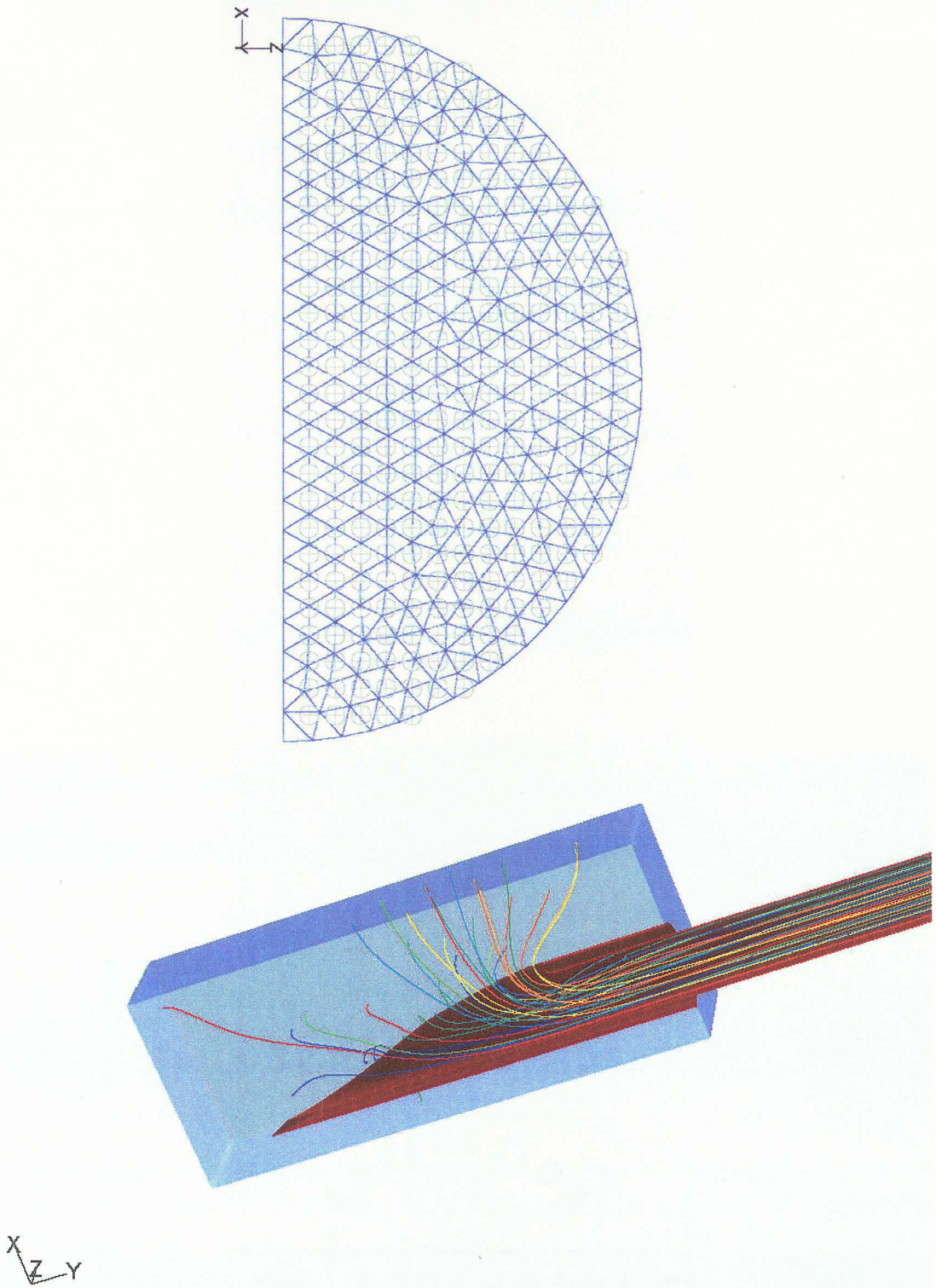


FIGURE 4.10 Schematic of sample points on half plane and the streamlines
(Cross-circle points are sample points)

Along each streamline, the time history of τ_s was extracted for hemolysis analysis. Fig. 4.11 shows an example of the development of τ_s as a function of time.

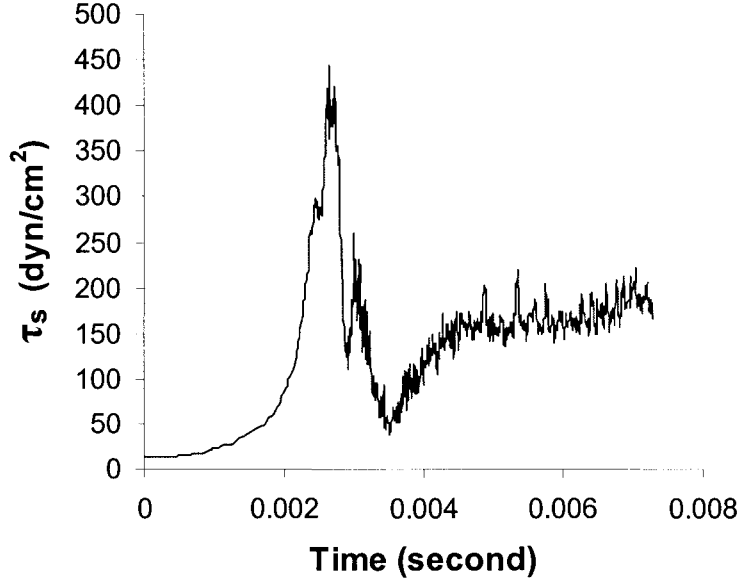


FIGURE 4.11 Time history of τ_s along an example streamline, without smoothing

To reduce numerical noise, a smoothing algorithm was applied:

$$\tau_{s,j}^{n+1} = \frac{(\tau_{s,j-1}^n + \tau_{s,j}^n + \tau_{s,j+1}^n)}{3}, j=1 \sim m \quad (4.5)$$

where m is the end of index of sampling point along streamline, n is iteration index and $n = 0 \sim 20$, $\tau_{s,j}^n$ represents scalar stress τ_s at time t_j . The maximum iteration number is

taken to 20. At the boundaries, use $\tau_{s,1}^{n+1} = \frac{(2 * \tau_{s,1}^n + \tau_{s,2}^n)}{3}$ at $j = 1$ and

$\tau_{s,m}^{n+1} = \frac{(\tau_{s,m-1}^n + 2 * \tau_{s,m}^n)}{3}$ at $j = m$. Fig. 4.12 shows the smoothed time history of τ_s along

the example streamline.

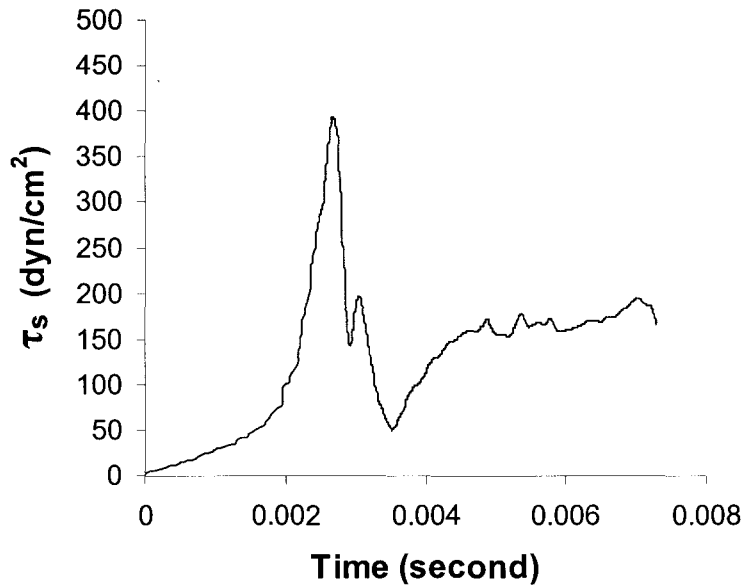


FIGURE 4.12 Time history of τ_s along an example streamline, with smoothing

Because the numerical simulations only cover 24.88 mm of the first (upstream) half of the needle, the time history of τ_s along the downstream half is taken as the constant value for fully developed Poiseuille flow at each sample point on the exit cross section.

For each cell along a particular streamline, the blood damage model is applied to assess whether the cell will be broken, or has a probability of being broken, depending on the blood damage model used. Factor F is used to represent the probability of membrane rupture along a particular streamline. $F = 0$ represents no membrane damage, $F = 1$ represents membrane failure and release of hemoglobin. To estimate the overall percentage of hemolysis for the total blood flow through the needle, the factor F for each streamline is weighted by the flow rate through the surrounding streamtube. The

overall percentage of hemolysis (index of hemolysis) of the blood flow through the needle is calculated by

$$IH = \frac{\sum_i F_i \cdot (\Delta Q)_i}{\sum_i (\Delta Q)_i} = \frac{\sum_i F_i \cdot (\Delta A)_i \cdot V_i}{\sum_i (\Delta A)_i \cdot V_i} = \frac{\sum_i F_i \cdot V_i}{\sum_i V_i} \quad (4.6)$$

Where, $(\Delta Q)_i = (\Delta A)_i \cdot V_i$ is the flow rate through each streamtube, $(\Delta A)_i$ is the cross-sectional area of each streamtube at the sample point, which is a square element. Because the sample points were uniformly distributed on the sample plane, $(\Delta A)_i$ is constant except around the boundary of the needle bore. For simplicity, the irregular areas of boundary streamtubes were ignored.

Blood Damage Models

Three blood damage models were applied to the results of the CFD simulation.

A strain-based blood damage model based on Rand's [1964] viscoelastic membrane model was developed previously in Chapter III.

$$\frac{S}{S_c} = \frac{4\alpha b}{5} (\tau_s - \tau_e) [C_0 + C_1(1 - \exp(-C_2 \cdot t)) + C_3 \cdot t] \quad (4.7)$$

where S is the area strain of the membrane, critical strain S_c for membrane failure is taken as $S_c = 0.064$ [Rand 1964 and Blackshears 1987]. α is an empirical constant, $b = 1.7 \mu\text{m} = 1.7 \times 10^{-4} \text{ cm}$ is the minor radius of deformed red cells. τ_s is the scalar stress, τ_e is the stress required to elongate the cell to an isochoric ellipsoid, and t is exposure time. $C_0 = 3.5 \times 10^{-2} \text{ cm/dyn}$, $C_1 = 3.9 \times 10^{-2} \text{ cm/dyn}$, and $C_3 = 1.5 \times 10^{-4} \text{ cm/dyn}\cdot\text{sec}$. C_0 and C_1 are related to the Young's moduli of the membrane, C_3 is related to the viscosity that

determines the long time characteristic of above model. C_0 , C_1 and C_3 were obtained by Rand's micropipette experiments. $\alpha = 39.01$, $\tau_e = 1200 \text{ dyn/cm}^2$ and $C_2 = 84 \text{ /sec}$ were obtained from optimization based on microscope images of deformed red cells.

For CFD analysis of hemolysis, the numerical integral form of equation 4.7 is applied along each streamline i:

$$\frac{S}{S_c} = \int \frac{dS/S_c}{dt} dt = \int \left(\frac{\partial S/S_c}{\partial \tau_s} \frac{\partial \tau_s}{\partial t} + \frac{\partial S/S_c}{\partial t} \right) dt \quad (4.8)$$

where $\frac{\partial S/S_c}{\partial \tau_s} = \frac{4\alpha b}{5} [C_0 + C_1(1 - \exp(-C_2 \cdot t)) + C_3 \cdot t]$,

$$\frac{\partial S/S_c}{\partial t} = \frac{4\alpha b}{5} (\tau_s - \tau_e) [C_1 \cdot C_2 \cdot \exp(-C_2 \cdot t) + C_3].$$

Therefore,

$$\begin{aligned} \left(\frac{S}{S_c} \right)_i &= \sum_{j=0}^m \frac{4\alpha b}{5} [C_0 + C_1(1 - \exp(-C_2 \cdot t_{i,j})) + C_3 \cdot t_{i,j}] (\tau_{si,j} - \tau_{si,j-1}) \\ &+ \frac{4\alpha b}{5} (\tau_{si,j} - \tau_e) [C_1 \cdot C_2 \cdot \exp(-C_2 \cdot t_{i,j}) + C_3] (t_{i,j} - t_{i,j-1}) \end{aligned} \quad (4.9)$$

where $j = 0$ to m , $j = 0$ is the starting time step when the red cell is near the entrance, $j = m$ is the ending time step when the cell is at the exit. At any point of j , if $(\tau_{si,j} - \tau_e) < 0$,

$(\tau_{si,j} - \tau_e)$ will be set equal to zero. $\left(\frac{S}{S_c} \right)_i$ is the normalized strain value along

streamline i . If along a particular streamline $\left(\frac{S}{S_c}\right)_i > 1$, then the red cells traveling along this streamline i is predicted to rupture.

$$F_i = \begin{cases} 1, & \text{for } \left(\frac{S}{S_c}\right)_i > 1; \\ 0, & \text{for } \left(\frac{S}{S_c}\right)_i \leq 1. \end{cases} \quad (4.10)$$

Above strain-based blood damage model will be applied to the CFD analysis of hemolysis and will be called strain-based model.

Two hemolysis models were included that are based on the empirical power-law equation

$$\Delta Hb / Hb = C \times t^a \times \tau_s^b \quad (4.11)$$

where Hb is total hemoglobin fraction, ΔHb is the released hemoglobin fraction and C is the constant coefficient.

The power-law model proposed by Heuser, *et al.* (1980) is given by

$$\Delta Hb / Hb = 1.8 \times 10^{-6} \times t^{0.765} \times \tau_s^{1.991} \quad (4.12)$$

Numerically integrating this equation along a streamline yields

$$F_i = \sum_{j=0}^m 1.8 \times 10^{-6} \times \tau_{si,j}^{1.991} \times (t_{i,j+1} - t_{i,j})^{0.765} \quad (4.13)$$

where $\tau_{si,j}$ is the scalar stress at step j along streamline i , $(t_{i,j+1} - t_{i,j})$ is the exposure time of the stress $\tau_{si,j}$.

Another power-law model proposed by Giersiepen, *et al.* (1990) is given by

$$\Delta Hb / Hb = 3.62 \times 10^{-5} \times t^{0.785} \times \tau_s^{2.416} \quad (4.14)$$

Numerically integrating along a streamline yields

$$F_i = \sum_{j=0}^m 3.62 \times 10^{-5} \times \tau_{si,j}^{2.416} \times (t_{i,j+1} - t_{i,j})^{0.785} \quad (4.15)$$

For the Heuser *et al.* and Giersiepen *et al.* models, the numerical integration along each streamline predicts some level of hemolysis on every streamline. However, for the strain-based model, the numerical integration along each streamline predicts complete hemolysis on streamlines along which the strain threshold is exceeded, and no hemolysis on the rest streamlines. Therefore, for flows in which high fluid stress is localized, a further discretization criterion is imposed on the spatial resolution of the high stress region, *i.e.*, that the number of streamlines on which lysis is predicted is large enough to accurately resolve the hemolysis fraction. This criterion can be approximated as a requirement that the number of blood-damaging streamlines exceed the reciprocal of the desired accuracy, *e.g.*, for 1 % accuracy, at least 100 hemolytic streamlines should be provided.

Each of the three blood damage models was applied to analyze flow-induced hemolysis for each needle type. Two C++ programs were written to process the streamline data extracted from the FLUENT simulation and to implement the blood damage models to obtain the index of hemolysis. The FLUENT data was exported in TECPLOT format. Two files were exported; they were scalar stress versus time for each streamline and velocity magnitude at the released plane for each streamline, which was

used to calculate the flow rate for each streamtube. The C++ programs were developed and compiled with Dev-C++, which is a free C/C++ tool under GNU General Public License. The first C++ program `dp_str_data.c` was used to analyze the data from these two files, and reverse the time sequence and smooth the curve for each streamline. This program provided the capability to employ MATLAB smooth functions (such as Gaussian smooth function etc.) to smooth the data. A second C++ program `dp_str_hemo.c` was written to implement the blood damage models to predict percentage of hemolysis from processed data provided by `dp_str_data.c`. For each streamline it did numerical integral for each model, summed and weighted the probability of hemolysis along each streamline by flow rate through each streamtube surrounding that particular streamline. All the programs and their input files for FLUENT are listed in APPENDIX D.

Hemolysis predictions from all three models were compared with experimental results, which found that the percentages of plasma-free hemoglobin were $\frac{\Delta Hb}{Hb} \% = 0.029, 0.040, \text{ and } 0.019$ for standard, beveled, and rounded entrances respectively. The experimental results showed that the needle with rounded entrance produced significantly less hemolysis than the standard one, while the one with beveled entrance produce more.

Results and Analysis

Table 4.2 shows the experimental results and predictions of hemolysis for three types of needles. Predicted hemolysis is given for two levels of spatial resolution to assess the discretization error. The percentage of error was calculated by (IH of lower

sample number - IH of higher sample number) / IH of higher sample number * 100% for each set of sample streamtubes. The differences in hemolysis between the two resolution levels are less than 5 % for all cases.

Table 4.3 shows that the number of hemolytic streamlines for the strain-based model exceeds 600 for both levels of spatial resolution, for an approximate accuracy of at least 0.17 %.

TABLE 4.2 Index of hemolysis of experiments and models
(note: *IH* was calculated from equation 4.6)

Needle	Experimental $\frac{\Delta Hb}{Hb}$ (%)	Number of sample streamtubes	Strain-based model		Heuser, et al.'s model		Giersiepen, et al.'s model	
			<i>IH</i> (%)	Error (%)	<i>IH</i> (%)	Error (%)	<i>IH</i> (%)	Error (%)
Standard Needle	0.029	47753	2.995	-4.74	0.1399	0.43	21.061	0.03
		11981	2.853		0.1405		21.068	
Beveled Needle	0.040	47752	3.383	0.65	0.1372	-2.19	21.488	-1.70
		11979	3.405		0.1342		21.122	
Rounded Needle	0.019	47747	2.771	0.51	0.1623	0.74	24.454	1.82
		11980	2.785		0.1635		24.900	

TABLE 4.3 Number of hemolytic streamlines for Strain-based model

Needle	Number of sample streamtubes	Number of hemolytic streamlines
Standard Needle	47753	2622
	11981	643
Beveled Needle	47752	2934
	11979	734
Rounded Needle	47747	2572
	11980	638

The magnitudes of the hemolysis fractions predicted by the models were much larger than the percentages of plasma-free hemoglobin measured in the experiments. The Heuser, *et al.* model produced the closest agreement, but was still roughly an order of magnitude off. The strain-based and Giersiepen, *et al.* models were roughly two and three orders of magnitude in error, respectively.

The empirical models were fit directly to hemolysis results produced by flow fields different from those in the needles in this study, therefore, the errors in their predictions may be related to these flow differences. For the strain-based model, the hemolysis prediction is thus far based on complete release of hemoglobin from all cells whose membranes have been predicted to fail. However, it has been observed that for short exposure to stress, pores created in the membrane may reseal before significant loss of hemoglobin has occurred [Lokhandwalla & Sturtevant 2001]. In addition, when cells elongate in response to longer duration uniaxial stress, their deformation may progress to a dumbbell shape that eventually pinches off in the smaller central section, again with little loss of hemoglobin (Fig. 4.13). Fig. 2.3 shows SEM pictures of red cells sheared between concentric cylinders by Suter & Mehrjardi [1975]. In the images for the higher shear rates, there are dumbbell shapes, remnants of dumbbells, and only a few cell fragments with openings in the membranes. This cell response tends to reduce hemoglobin loss and support lower plasma-free hemoglobin prediction. Furthermore, since the membrane failure threshold in equation 4.9 is proportional to a mean minor diameter b , but cells in whole blood have a distribution of minor diameters, a further reduction in hemolysis prediction is justified for this model.

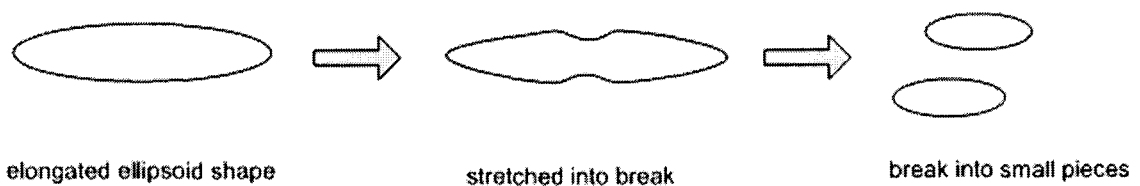


FIGURE 4.13 The Schematic of the cell breaking into small pieces

Mechanistic representations of these factors are reserved for future work. In the interim, an empirical factor of $C_e = 9.68 \times 10^{-3}$ was introduced into the strain-based model (optimized) to match exactly the plasma-free hemoglobin results for the standard needle

$$IH = C_e \frac{\sum_i F_i \cdot (\Delta Q)_i}{\sum_i (\Delta Q)_i} = C_e \frac{\sum_i F_i \cdot (\Delta A)_i \cdot V_i}{\sum_i (\Delta A)_i \cdot V_i} = C_e \frac{\sum_i F_i \cdot V_i}{\sum_i V_i} \quad (4.16)$$

Similar factors are applied to the Heuser, *et al.* and the Giersiepen, *et al.* models to match their predictions to the experimental result for the standard needle. These factors were $C_e = 0.21$ for the Heuser, *et al.* model, and $C_e = 14.08 \times 10^{-3}$ for the Giersiepen, *et al.* model. Hemolysis predictions using these factors were then compared to experimental results for the other two needle types.

Fig. 4.14 shows the experimental results and adjusted prediction results for the higher spatial resolution of about 48000 sample streamtubes. Only the strain-based model correctly predicts increased hemolysis in the beveled needle and decreased hemolysis in the rounded needle. The Giersiepen *et al.* model correctly predicts increased hemolysis in the beveled needle, but the Heuser, *et al.* model predicts a small reduction. Both models incorrectly predict increased hemolysis in the rounded needle.

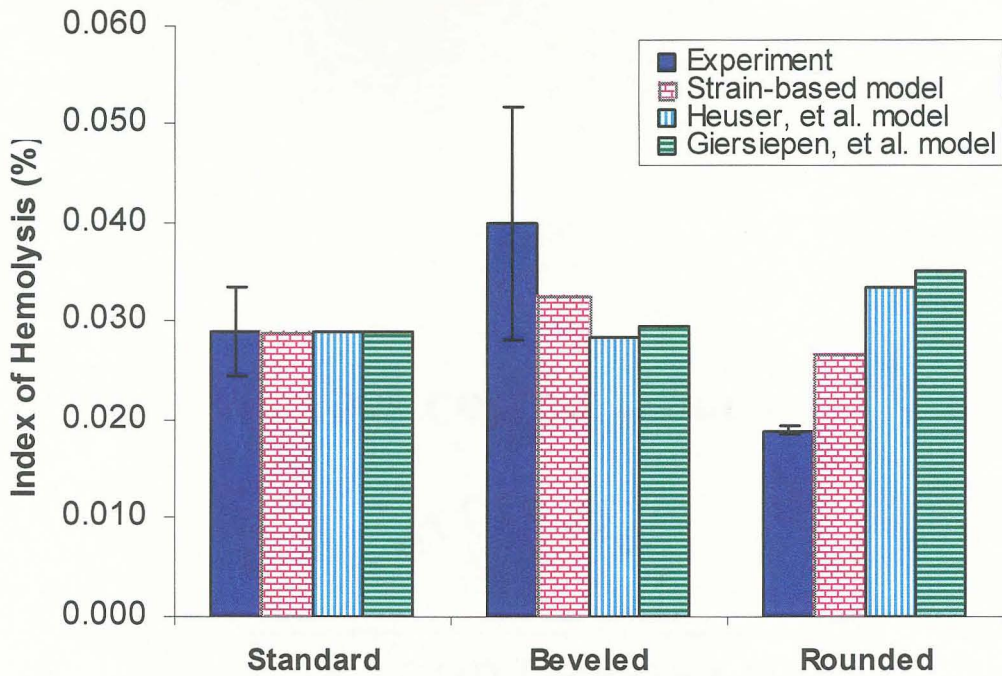


FIGURE 4.14 Index of hemolysis of the needles

Discussion

This test of hemolysis prediction models in the flows in these needles may appear to be a severe one, given that the approximately 10% higher bulk flow rate in the rounded needle (Table 4.1) tends to increase fluid stress across the entire flow cross section. This higher flow rate contributed to incorrect predictions of higher hemolysis by the Giersiepen *et al.* and Heuser *et al.* models. Correctly predicting smaller hemolysis in the rounded needle apparently depends on identification of more subtle local differences in flow patterns. Yet, recognizing such distinctions are of fundamental importance, since the modifications made to the needles are representative of the changes that might be considered in refining cardiovascular devices. Changes in the leading edge of the impeller in a centrifugal blood pump and smoothing of inlet and outlet ports in a

ventricular assist device are examples of design alternatives with analogous local impact on an otherwise similar bulk flow. Keys to the optimization of device design are not only accurate hemolysis results, but also the interpretation of the influence of design changes that CFD and a mechanistic hemolysis model can provide.

In the case of the needle flow, the local flow features contributing to the differences in hemolysis among the needles can be explained in the following figures. Fig. 4.15 shows the scatter plots of the hemolysis produced in each streamtube IH_i on a cross-section plane at 7mm from the tip of each of the three types of needles for the strain-based model, where $IH_i = \frac{F_i \cdot V_i}{\sum_i V_i}$ for each streamtube i . To simplify the calculation, streamtubes are represented as squares of the same dimension as initially specified at the exit of the needle. The center of each square marker corresponds to the central position of the streamtube and its color represents the value of IH_i . Four red groups of approximately 60 streamtubes each appear in the plot for the standard needle, and represent the regions of the flow that contribute most to overall hemolysis. For the beveled needle, two red groups and one large orange group appear higher in the cross section than for the standard needle, and the green regions of moderate hemolysis are slightly more numerous and shift toward the lower wall of the tube. For the rounded needle only two red groups appear still higher in the cross section, and the concentration of green streamtubes near the walls is reduced. These plots confirm that the strongest contributor to hemolysis is the high velocity flow past the distal edge of the needle opening, as suggested by the fluid stress plots in Fig. 4.5.

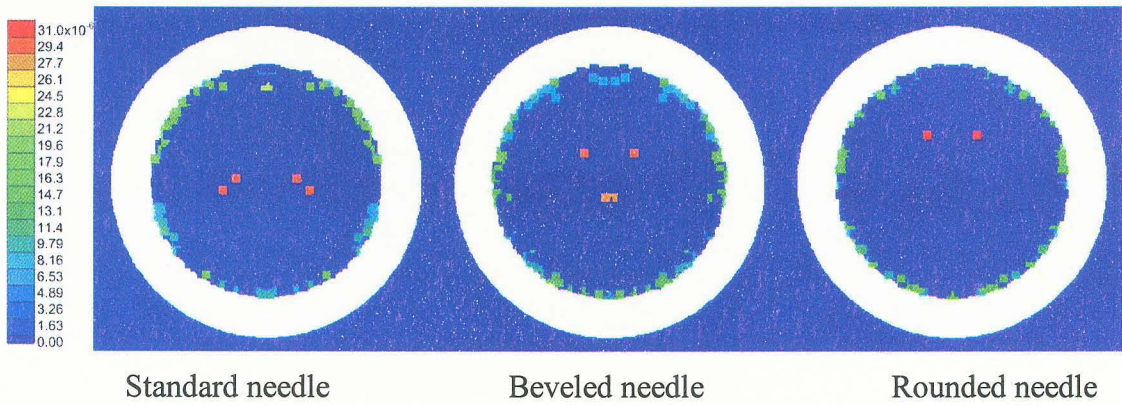
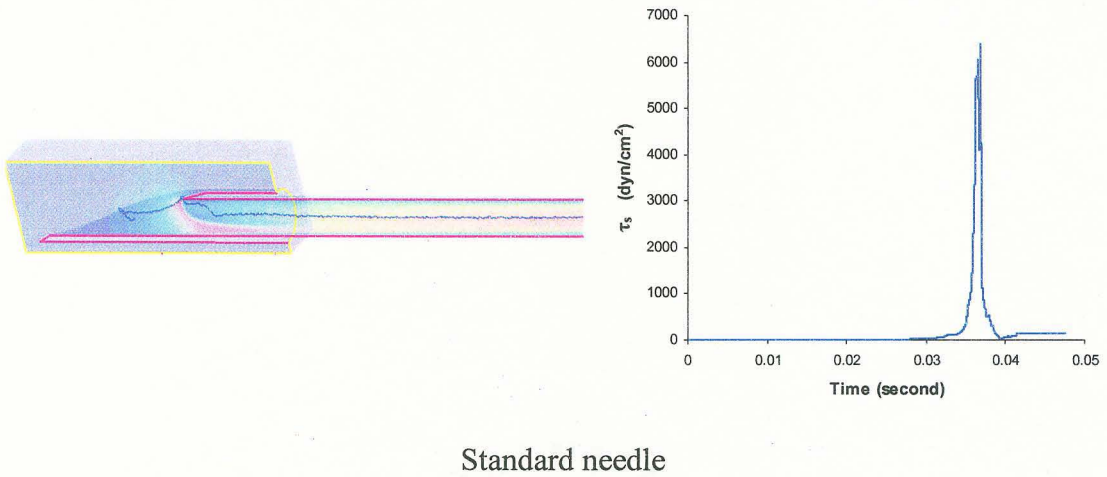
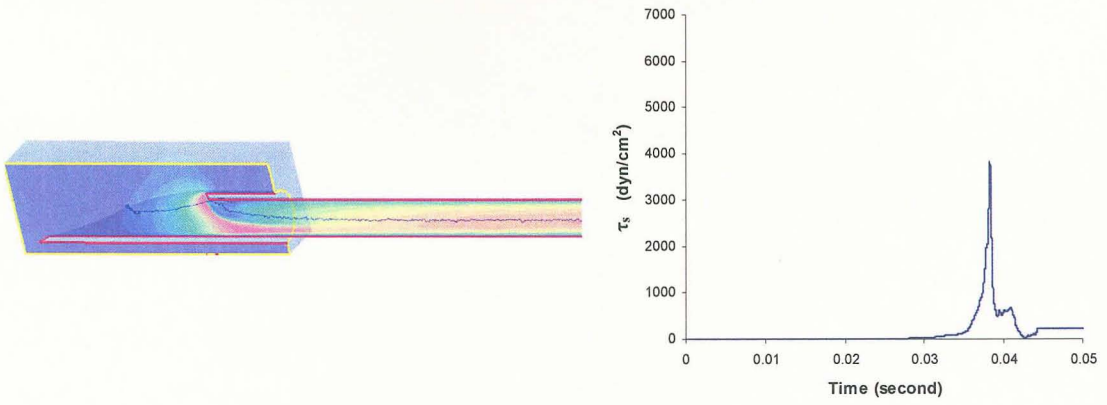


FIGURE 4.15 Scatter plots of IH_i on cross-section plane from strain-based model

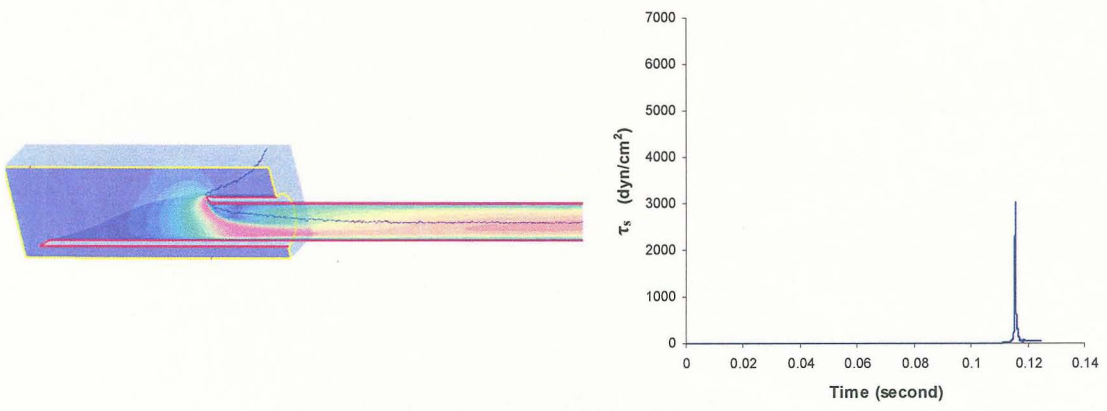
The high hemolysis regions are further compared in Fig. 4.16, which shows 3d plots and time histories of τ_s of streamlines that pass through the upper right red region in Fig. 4.15 for each needle type. For the standard needle, the peak value of τ_s exceeded 6000 dyn/cm². For the beveled needle, the peak value was about 4000 dyn/cm²; and for the rounded needle, the peak value was about 3000 dyn/cm².



Standard needle



Beveled needle



Rounded needle

FIGURE 4.16 Time history of τ_s along streamline with lysis

With the strain-based model and plots of parameter IH_i and τ_s , a developer of cardiovascular devices can evaluate the flow region that is critical to reduce hemolysis. When a modified design for the geometry of cardiovascular device is formulated, these tools can be used to evaluate the resulting index of hemolysis, and explain how the change in flow pattern may help to reduce hemolysis.

The correct prediction of hemolysis trends among the different needle entrance geometries is a significant, though tentative, step toward providing a hemolysis prediction model for complex blood flows. The current strain-based model requires, in

particular, an empirical factor to decrease the hemolysis prediction by about two orders of magnitude. The magnitude of this factor indicates that significant aspects of the mechanics of release of hemoglobin from red cells have not yet been incorporated into the model. Nonetheless, the results shows that the strain-based blood damage model has the potential to be an effective tool in the application of CFD analysis to hemolysis. With further verification in a range of flows, the model will facilitate the development of prototypes of cardiovascular devices for decreased hemolysis with reduced time and cost.

One limitation of this model is that it does not apply well to exposure time less than about 1 ms (Chapter III). For many applications in cardiovascular devices, which have exposure times larger than 1ms, this is not a problem. But for bubble flow and shockwave flow, the inertial effect may be dominant and a mass term may be needed to provide better fits. Therefore, one of the future improvements for this model may be to add a mass term into the current Maxwell/Voigt mechanical model. Another improvement may be to investigate the time dependence of τ_e in the model, which represents the variability of the stress threshold to reach the isochoric shape.

CHAPTER V

SUMMARY AND CONCLUSIONS

The high-speed laser-illuminated micro-imaging experiment presented in this paper provides an effective, non-invasive method to capture and investigate the deformation of red cells under flow stress. It enables the user to capture images of deformed cells with average velocity of up to 4 m/s and a range of fluid stresses up to 5000 dyn/cm². It reveals the genuine behavior of red cells in flow, and will help researchers to understand the mechanism of flow-induced deformation and membrane damage of red cells. In this project, it provides a tool to calibrate the empirical coefficients in the blood damage model.

The CFD analysis of hemolysis for blood flow through needles proved an effective and alternative tool to predict flow-induced hemolysis. The numerical simulation of the needle flow identified the local flow features contributing to the differences in hemolysis among the needles. The CFD tool provides a convenient way to investigate the details inside of the 3-dimensional flow field, and to compare the difference of flow patterns among cardiovascular devices. It will help promote the speed of design for cardiovascular devices and reduce the expense and testing time of prototypes.

Both the micro-imaging experiment and the CFD analysis show that the strain-based blood damage model developed in this paper is an effective blood damage model. The strain-based model provides reasonable estimates of the strain and deformation of red cells under fluid stress, and facilitates comparing the prediction of model with experimental observation. In the micro-imaging experiment, parameter α for the one-parameter model fit to a hemolysis threshold is close to the same value as that for the three-parameter model fit to images of deformed red cells. This similarity suggests that the mechanistic approach adopted in this study to relate cell membrane failure as a membrane strain limit has some validity. In the CFD analysis of needle flow, the strain-based blood damage model predicted the reduced hemolysis by 7.4% in rounded needle and the increased hemolysis by 13% in beveled needle, and agreed with the trend measured by experiments which showed the rounded entrance reduced hemolysis by 34%, but the beveled entrance increased hemolysis by 38%. Both Heuser *et al.* model and Giersiepen *et al.* model predicted increased hemolysis in rounded needle. Therefore, the strain-based model enables the identification of more subtle local differences in flow patterns, and recognizing such distinctions are of fundamental importance for the modifications made to the needles or refining cardiovascular devices.

One limitation of this model is that it can not be applied to exposure time less than 1ms. For most of the applications in cardiovascular devices, which have exposure times larger than 1ms, it is not a problem. But for bubble flow and shockwave flow, the inertial effect will be dominant and the mass term must be included.

One of the future improvements for this model may be to add a mass term into the mechanical model of spring and dash-pot. Another improvement may be to

investigate the time dependence of τ_e in the model, instead of using a constant value.

Recall that τ_e represents the stress threshold to reach the isochoric shape.

A future improvement for the high-speed laser-illuminated micro-imaging experiment is to capture multiple states of a single cell's deformation. It will provide a significant and solid measure to discover the mechanism of red cell (or other biological cell) deformation and membrane rupture, and verify whether membranes reseal again after rupture.

REFERENCES

- Ahmed S., Fumakubo A., Sakuma I Fukui Y. & Dohi T., "Experimental Study on Hemolysis in Centrifugal Blood Pumps: Improvement of Flow Visualization Method", *Artif Organs*, 23(6):542-6, 1999.
- Bacher R.P. & Williams M.C., *J Lab Clin Med*, 76:485, 1970.
- Barthes-Biesel D., "Flow-induced capsule deformation", Modeling and simulation of capsules and biological cells, chapter 1, p1-2, Pozrikids C, eds, CHAPMAN & HALL/CRC, 2003.
- Beissinger R.L. & Laugel J-F., "Low-stress hemolysis in laminar flow: Bulk and surface effects in capillaries", *AIChE J*, 33(1):99-108, 1987.
- Blackshear P.L. "In biomechanics: its foundations and objectives", Y C Fung, N Perrone, and M Anliker, editors, Prentice-Hall, Inc., Englewood Cliffs, N J, 501, 1972.
- Blackshear P.L. & Blackshear G.L., "Mechanical hemolysis", Handbook of Bioengineering, chapter 15, pp15.1-15.9, Skalak R and Chien S, eds, McGraw-Hill, New York, 1987.
- Bludszuweit C., "Model for a general mechanical blood damage prediction", *Artif Organs*, 19(7):583-589, 1995.
- Conrad Pfafferott, Gerard B. Nash & Herbert J. Meiselman, "Red blood cell deformation in shear flow: effects of internal and external phase viscosity and of in vivo aging", *Biophys J*, 47:695-704, 1985.
- Cokelet G.R. & Meiselman H.J., "Rheological comparison of hemoglobin solutions and erythrocyte suspensions", *Science*, 162:275, 1968.
- Evans E.A. & Fung Y.C., "Improved measurements of the erythrocyte geometry", *Microvasc. Res.* 4:337-47, 1972.
- Evans E.A. & Hochmuth R.M., "Membrane viscoelasticity", *Biophys J*, 16:1-10, 1976.
- Evans E.A., Waugh R. & Melnik L., "Elastic area compressibility modulus of red cell membrane", *Biophys J*, 16:585-595, 1976.

- Evans E.A., Waugh R. & Melnik L., "A solid-liquid composite model of the red cell membrane", *The Journal of Membrane Biology*, 30:351-362, 1977.
- Fischer T. & Schmid-Schonbein H., "Tank tread motion of red cell membranes in viscometer flow: Behavior of intracellular and extracellular markers (with film)", *Blood Cells*, 3:351-365, 1977.
- Forstrom R.J., "A new measure of erythrocyte membrane strength: the jet fragility test", PhD thesis, University of Minnesota, Minneapolis, 1969.
- Fung Y.C., "Biomechanics: Mechanical Properties of Living Tissues", 2nd Edition, Springer-Verlag, New York, pp. 116, 1993.
- Fung Y.C., Tsang WCO & Patitucci P., "High-resolution data on the geometry of red blood cells", *Biorheology* 18:369, 1981.
- Giersiepen M., Wurzinger L.J., Optiz R. & Reul H., "Estimation of shear stress-related blood damage in heart valve prostheses: In vitro comparison of 25 aortic valves", *Int J Artif Organs*, 13:300-306, 1990.
- Goldsmith H.L. & Marlow J., "Flow behaviour of erythrocytes. I. Rotation and deformation in dilute suspensions", *Proc. R. Soc. London, Ser. B*, 182:351-384, 1972.
- Hellums J.D. & Hardwick P.A., "Response of platelets to shear stress-A review", A review in: The Rheology of Blood, Blood Vessels and Associated Tissue, edited by Gross and Hwang. Rockville: Sijthoff and Noordhoff, p.160, 1981.
- Heuser G. & Optiz R., "A couette viscometer for short time shearing in blood", *Biorheology*, 17:17-24, 1980.
- Hochmuth R.M, Worthy P.R. & Evans E.A., "Red cell extensional recovery and the determination of membrane viscosity", *Biophys J*, 26:101-114, 1979.
- John Sleep, David Wilson, Robert Simmons & Walter Gratzer, "Elasticity of the red cell membrane and its relation to hemolytic disorder: an optical tweezers study", *Biophys J*, 77:3085-95, 1999.
- Lei Gu & William A. Smith, "Evaluation of Computational Models for Hemolysis Estimation", *ASAIO J*, 51:202-207, 2005.
- Leverett L.B., Hellums J.D., Alfrey C.P. & Lynch E.C., "Red blood cell damage by shear stress," *Biophys J*, 12:257-273, 1972.
- Leyrat-Maurin A. & Barthes-Biesel D., "Motion of a deformable capsule through a hyperbolic constriction", *J. Fluid Mech.*, 279:135-163, 1994.

- Li J., Dai M., Lim C.T. & Suresh S., "Spectrin-level modeling of the cytoskeleton and optical tweezers stretching of the erythrocyte", *Biophys J*, 88:3707-3719, 2005.
- Li X. Z., Barthes-Biesel D. & Helmy A., "Large deformation and burst of a capsule freely suspended in an elongational flow", *J. Fluid Mech.*, 187:179-196, 1988.
- Lokhandwalla M., "Damage mechanism in shock wave lithotripsy", PhD Thesis, California Institute of Technology, Pasadena, CA, 2001.
- Lokhandwalla M. & Sturtevant B., "Mechanical hemolysis in shock wave lithotripsy (SWL): I. analysis of cell deformation due to SWL flow fields", *Physics in Med. & Biol.*, 46(4):413-37, 2001.
- Mohandas N. & Evans E.A., "Mechanical properties of the red cell membrane in relation to molecular structure and genetic defects", *Annu Rev Biophys Biomol Struct*, 23:787, 1994.
- Nobuhisa Honda, Taro Inamoto, Masamichi Nogawa & Setsuo Takatani, "Ultracompact, completely implantable permanent use electromechanical ventricular assist device and total artificial heart", *Artif Organs*, 23(3):253-261, 1999.
- Perry L Blackshear & Gertrude L Blackshear, "Mechanical Hemolysis", Handbook of bioengineering, chapter 15, p15.1-15.9, Skalak R and Chien S, eds, McGraw-Hill, New York, 1987.
- Piccione W., "Bridge to transport with the HeartMate device", *J Card Surg*, 16:272-9, 2001.
- Pozrikidis C., "Numerical simulation of the flow-induced deformation of red blood cells", *Annals of biomedical engineering*, 31:1194-1205, 2003.
- Raisky F., Gauthier C., Marchal A. & Blum D., "Haemolyzed samples responsibility of short catheters", *Ann Biol Clin Paris* 52, 523-527, 1994.
- Ramanujan S. & Pozrikidis C., "Deformation of liquid capsules enclosed by elastic membranes in simple shear flow: large deformations and the effect of fluid viscosities", *J. Fluid Mech.*, 361:117-143, 1998.
- Rand R.P., "Mechanical properties of the red cell membrane: II Viscoelastic breakdown of the membrane", *Biophys J*, 4:303-316, 1964.
- Ronney J.A., 1970, "Hemolysis Near an Ultrasonically Pulsating Gas Bubble", *Science*, 169:869-871, 1970.

- Secomb T.W., “Mechanics of red blood cells and blood flow in narrow tubes”, Modeling and simulation of capsules and biological cells, chapter 4, p168-169, Pozrikids C., eds, CHAPMAN & HALL/CRC, 2003.
- Sharp M.K. & Mohammad S.F., “The scaling of hemolysis in needles and catheters”, *Ann Biomed Eng*, 26(5):788-797, 1998.
- Shigehiro Hashimoto, “Erythrocyte Destruction under Periodically Fluctuating Shear Rate: Comparative Study with Constant Shear Rate”, *Artif Organs*, 13(5):458-463, 1989.
- Sutera S.P. & Mehrjardi M.H., “Deformation and fragmentation of human red blood cells in turbulent shear flow”, *Biophys J*, Vol. 15, pp.1-10, 1975.
- Tran-Son-Tay R., Sutera S.P. & Rao P.R., “Determination of the red blood cell membrane viscosity from rheoscopic observations of tank-treading motion”, *Biophys J*, 46:65-72, 1984.
- Waugh R.E. & Evens E.A., “Thermoelasticity of red blood cell membrane”, *Biophys J*, 26:115-132, 1979.
- Waugh R.E. & Hochmuth R.M., “Mechanics and deformability of hemotocytes”, Biomechanics principles and applications. chapter 15, p227-232, Daniel J Schneck and Joseph D Bronzino, eds, CRC press, 2002.
- Williams A.R., Hughes D.E. & Hyborg W.L., “Hemolysis near a transversely oscillating wire”, *Science*, 169:871-873, 1970.
- Williams A.R., “Viscoelasticity of the human erythrocyte membrane”, *Biorheology*, 10:313-319, 1973.
- Williams J.C., Woodward J.F., Stonehill M.A., Evans A.P. & McAteer J.A., “Cell damage by lithotripter shock waves at high pressure to preclude cavitation”, *Ultrasound Med. Biol.*, 25:1445-1449, 1999.
- Yangsheng Chen, M. Keith Sharp, “A Strain-Based Flow-Induced Hemolysis Prediction Model Calibrated by In-Vitro Erythrocyte Deformation Measurements”, submitted to Annual of Biomedical Engineering, 2006.
- Yangsheng Chen, M. Keith Sharp, “Constitutive Model for Flow-Induced Hemolysis and Experimental Analysis”, Abstract in 5th World Congress of Biomechanics, Munich, Germany, still to come.
- Yangsheng Chen, M. Keith Sharp, “An Experimental System for Investigating Flow-induced Hemolysis”, Abstract in Conference Proceedings and Poster Presentation,

2005 Summer Bioengineering, American Society of Mechanical Engineers (ASME), Vail Cascade Resort & Spa, Vail, Colorado, June 22-26, 2005.

Yangsheng Chen, M. Keith Sharp, "Investigation of the Mechanisms of Flow-induced Hemolysis", Abstract in Conference Proceedings and Poster Presentation, Kentucky Science & Engineering Foundation (KSEF), Hyatt Regency Hotel, Louisville, Kentucky, March 3, 2004.

Yangsheng Chen, M. Keith Sharp, "An Experimental System for Investigating Flow-induced Hemolysis", Abstract in Conference Proceedings and Poster Presentation, Biomedical Engineering Society (BMES), Nashville, Tennessee, October 1-4, 2003.

Yangsheng Chen, M. Keith Sharp, "Investigation of Flow-induced Damage to Red Blood Cells", Poster Presentation, Kentucky Science & Engineering Foundation (KSEF), Hyatt Regency Lexington, Kentucky, March 5, 2003.

Yukio Ohashi, Aron de Andrade & Yuihiko Nose, "Hemolysis in an electromechanical driven pulsatile total artificial heart", *Artif Organs*, 27(12):1089-1093, 2003.

Zhao Y & Sharp MK, "Finite element analysis of the lift on a slightly deformable and freely rotating and translating circular cylinder in two-dimensional channel flow," *J Biomech Eng*, 121:2:148-152, 1999.

APPENDIX A

Ellipsoid Calculation Formula

The volume and surface area of prolate ellipsoid (Figure A.1) are calculated by

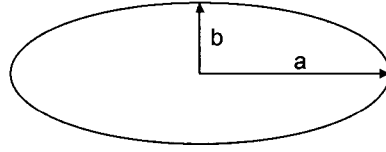


FIGURE A.1 Prolate ellipsoid shape of stretched red cell

$$V = \frac{4}{3}\pi ab^2 \quad (\text{A.1})$$

$$A = 2\pi \left[b^2 + \frac{a^2 b}{\sqrt{a^2 - b^2}} \arcsin \sqrt{1 - \frac{b^2}{a^2}} \right] \quad (\text{A.2})$$

where a is the major radius, b is the minor radius.

Keeping V as constant of $96 \mu\text{m}^3$ and giving value of a , value of b can be calculated by

$$b = \sqrt{\frac{3V}{4\pi a}} \quad (\text{A.3})$$

Then the aspect ratio a/b and surface area A can be obtained. The area strain of a red cell will be calculated by $S = \frac{A - A_0}{A_0}$, where A_0 is the surface area of a non-deformed red cell of $130 \mu\text{m}^2$. The 6.4% area strain will be obtained when the aspect ratio is 4.7 with the major radius $a = 8.1 \mu\text{m}$ and the minor radius $b = 1.7 \mu\text{m}$.

APPENDIX B

NOMENCLATURE

a	major radius of red cells, μm
b	minor radius of red cells, μm
a/b	aspect ratio, dimensionless
D	width of the channel, mm
D_i	inner diameter of the needle, inch
D_o	outer diameter of the needle, inch
Hb	total hemoglobin content, mg/dl
ΔHb	released hemoglobin content, mg/dl
m	mass, kg
p, Δp	pressure and pressure drop, Pa
S	strain of membrane, dimensionless
S_c	critical strain of membrane, dimensionless
Sph	sphericity of red cells, dimensionless
Re	Reynolds number, dimensionless
t	time, s
T	membrane tension, dyn/cm
u	flow velocity component along direction x, m/s
v	flow velocity component along direction y, m/s
v	magnitude of velocity, m/s
\bar{v}	average velocity, m/s
\bar{v}_{max}	maximum velocity, m/s
w	flow velocity component along direction z, m/s
η_m	coefficient of membrane surface viscosity, poise·cm
μ	viscosity of the fluid, CP (centipoises)
μ_m	shear modulus, dyn/cm
ρ	density, kg/m^3
σ	biaxial tension, dyn/cm
σ_c	critical biaxial tension, dyn/cm
$\sigma_1, \sigma_2, \sigma_3$	principal stresses, dyn/cm^2
τ	shear stress, dyn/cm^2
τ_w	shear stress on the wall, dyn/cm^2
τ_{von}	von Mises stress, dyn/cm^2
τ_s	scalar stress, dyn/cm^2

APPENDIX D

List of Programs

FLUENT Files

“stress_define_sh_dyn.dat”: define the scalar stress for post processing for FLUENT.

```
(custom-field-function/define
'(((name tao-xx) (display "2 * viscosity-lam * dx-velocity-dx") (syntax-tree ("*" ("*" 2
"viscosity-lam") "dx-velocity-dx")) (code (field-* (field-* 2 (field-load "viscosity-lam")
(field-load "dx-velocity-dx")))))
((name tao-yy) (display "2 * viscosity-lam * dy-velocity-dy") (syntax-tree ("*" ("*" 2
"viscosity-lam") "dy-velocity-dy")) (code (field-* (field-* 2 (field-load "viscosity-lam")
(field-load "dy-velocity-dy")))))
((name tao-zz) (display "2 * viscosity-lam * dz-velocity-dz") (syntax-tree ("*" ("*" 2
"viscosity-lam") "dz-velocity-dz")) (code (field-* (field-* 2 (field-load "viscosity-lam")
(field-load "dz-velocity-dz")))))
((name tao-xy) (display "viscosity-lam * (dx-velocity-dy + dy-velocity-dx)") (syntax-
tree ("*" "viscosity-lam" ("+" "dx-velocity-dy" "dy-velocity-dx"))) (code (field-* (field-
load "viscosity-lam") (field-+ (field-load "dx-velocity-dy") (field-load "dy-velocity-
dx")))))
((name tao-yz) (display "viscosity-lam * (dy-velocity-dz + dz-velocity-dy)") (syntax-
tree ("*" "viscosity-lam" ("+" "dy-velocity-dz" "dz-velocity-dy"))) (code (field-* (field-
load "viscosity-lam") (field-+ (field-load "dy-velocity-dz") (field-load "dz-velocity-
dy")))))
((name tao-xz) (display "viscosity-lam * (dx-velocity-dz + dz-velocity-dx)") (syntax-
tree ("*" "viscosity-lam" ("+" "dx-velocity-dz" "dz-velocity-dx"))) (code (field-* (field-
load "viscosity-lam") (field-+ (field-load "dx-velocity-dz") (field-load "dz-velocity-
dx")))))
((name tao-von_1) (display "(tao-xx - tao-yy) ^ 2 + (tao-xx - tao-zz) ^ 2 + (tao-yy - tao-
zz) ^ 2") (syntax-tree ("+" ("+" ("**" ("-" "tao-xx" "tao-yy") 2) ("**" ("-" "tao-xx" "tao-
zz") 2)) ("**" ("-" "tao-yy" "tao-zz") 2))) (code (field-+ (field-+ (field-** (field-- (cx-
field-eval "tao-xx") (cx-field-eval "tao-yy")) 2) (field-** (field-- (cx-field-eval "tao-xx")
(cx-field-eval "tao-zz")) 2)) (field-** (field-- (cx-field-eval "tao-yy") (cx-field-eval "tao-
zz")) 2))))
((name tao-von_2) (display "6 * (tao-xy ^ 2 + tao-yz ^ 2 + tao-xz ^ 2)") (syntax-tree
("*" 6 ("+" ("+" ("**" "tao-xy" 2) ("**" "tao-yz" 2)) ("**" "tao-xz" 2)))) (code (field-* 6
```

```
(field-+ (field-+ (field-** (cx-field-eval "tao-xy") 2) (field-** (cx-field-eval "tao-yz") 2))
(field-** (cx-field-eval "tao-xz") 2))))))
((name tao-von) (display "sqrt ((tao-von_1 + tao-von_2) / 2)") (syntax-tree ("sqrt" ("/"
"+" "tao-von_1" "tao-von_2") 2))) (code (field-sqrt (field-/ (field-+ (cx-field-eval "tao-
von_1") (cx-field-eval "tao-von_2")) 2))))
((name tao-von_sh_dyn) (display "10 * tao-von / sqrt (3)") (syntax-tree ("/" ("*" 10
"tao-von") 1.7320508)) (code (field-/ (field-* 10 (cx-field-eval "tao-von")) 1.7320508)))
))
```

C++ Programs

“*dp_str_data.c*”: used to analyze the data files from FLEUNT, and reverse the time sequence and smooth the curve for each streamline.

// the stream line is created reversely, i.e. form the outflow to upward

```
#include <stdio.h>
#include <math.h>
#include <string.h>
#include <time.h>
/*#include "engine.h" // calling MATLAB from a C with MATLAB Engine.
#include "matrix.h" // calling MATLAB from a C with MATLAB Engine. */

// LINBUF is the maximum number of characters in single line
#define LINBUF 400

//// NL is the maximum number of lines
#define NL 80000

// MIU is the coefficient of viscosity (saline water) (unit: kg/m/s=Pa.s)
#define MIU 0.0035105

int main(int argc, char *argv[])
{
//----- define variables for read data

float *data[NL][2]; // 0: X axis
// 1: Y axis

// v0: the velocity magnitude in the release plane of the stream lines
// sy0: the Y-face area of cell in the release plane of the stream lines
// sumsy: the sum of Y-face area of cell in the release plane of the stream lines
```

```

float v0[NL],sy0[NL];
double sumsy;

FILE *fin, *fou, *fou1, *fou2, *fp0;
char argv1[LINBUF],argv2[LINBUF],argv3[LINBUF];

int i,j,k,t0,m;
char tmp0[LINBUF],tmp1[LINBUF];

// nl the the total number of lines
int nl=0;

// np[] the the total number of point for each line
int np[NL];

// flag for each data block
int data_flag=0;          // 0: non data; 1:data

/** MATLAB Engine
Engine *ep;
mxArray *tin=NULL, *tout=NULL, *tout_2p=NULL;
double *tin_pr, *tout_pr, *tout_2p_pr;
//mxClassID class=mxSINGLE_CLASS;
mxClassID class=mxDOUBLE_CLASS; */

// flag for smooth methods
int sm_flag=0;          // 0: simple method (non MATLAB); 1:use MATLAB

//===== read data from file =====
fou=fopen("strf3dn.dat","w");
fou1=fopen("strf3dn_v.dat","w");
fou2=fopen("strf3dn_s.dat","w");
fp0=fopen("tmp.dat","w");

fin=fopen("input_filename.txt","r");
fscanf(fin,"%s\n",argv1);
fscanf(fin,"%s\n",argv2);
fscanf(fin,"%s\n",argv3);
//fgets(argv1,LINBUF,fin);
//fgets(argv2,LINBUF,fin);
//fgets(argv3,LINBUF,fin);
fprintf(fp0,"%s\n",argv1);
fprintf(fp0,"%s\n",argv2);
fprintf(fp0,"%s\n",argv3);
fclose(fin);

```

```
printf("Processing data files: \"%s\" and \"%s\" and \"%s\" : ... \n",argv1,argv2, argv3);
```

```
//fin=fopen("strf3d.dat","r");
```

```
//fin=fopen(argv[1],"r");
```

```
fin=fopen(argv1,"r");
```

```
fprintf(fp0,"%s\n",argv1);
```

```
i=0;
```

```
while(fgets(tmp0,LINBUF,fin)!=NULL) {
```

```
    if(strncmp(tmp0,"(xy/key/label",14)==0) {
```

```
        //fprintf(fou,"%s",tmp0);
```

```
        j=0;
```

```
        data_flag=1;
```

```
        continue;
```

```
    }
```

```
    if(strncmp(tmp0,")",1)==0) {
```

```
        //fprintf(fou,"%s",tmp0);
```

```
        np[i]=j;
```

```
        for(k=0;k<2;k++) {
```

```
            data[i][k]=calloc(np[i],sizeof(float));
```

```
        }
```

```
        i++;
```

```
        data_flag=0;
```

```
        continue;
```

```
    }
```

```
    if(data_flag==1) {
```

```
        //scanf(tmp0,"%f %f",&data[i][0][j],&data[i][1][j]);
```

```
        j++;
```

```
    }
```

```
}
```

```
nl=i;
```

```
//fprintf(fou,"nl=%d\n",nl);
```

```
fclose(fin);
```

```
//fin=fopen("strf3d.dat","r");
```

```
//fin=fopen(argv[1],"r");
```

```
fin=fopen(argv1,"r");
```

```
fprintf(fp0,"%s\n",argv1);
```

```
i=0;
```

```
while(fgets(tmp0,LINBUF,fin)!=NULL) {
```

```
    if(strncmp(tmp0,"(xy/key/label",14)==0) {
```

```
        j=0;
```

```
        data_flag=1;
```

```
        continue;
```

```

}
if(strncmp(tmp0,"",1)==0) {
    //np[i]=j;
    i++;
    data_flag=0;
    continue;
}
if(data_flag==1) {
    sscanf(tmp0,"%f %f",&data[i][0][j],&data[i][1][j]);
    j++;
}
}
fclose(fin);

//fin=fopen(argv[2],"r");
fin=fopen(argv2,"r");
i=0;
while(fgets(tmp0,LINBUF,fin)!=NULL) {
    if(strncmp(tmp0,"(xy/key/label",14)==0) {
        j=0;
        data_flag=1;
        continue;
    }
    if(strncmp(tmp0,"",1)==0) {
        //np[i]=j;
        i++;
        data_flag=0;
        continue;
    }
    if(data_flag==1) {
        if(j==0) sscanf(tmp0,"%*f %f",&v0[i]);
        //sscanf(tmp0,"%f %f",&data[i][0][j],&data[i][1][j]);
        j++;
    }
}
fclose(fin);

//fin=fopen(argv[3],"r");
fin=fopen(argv3,"r");
i=0;
while(fgets(tmp0,LINBUF,fin)!=NULL) {
    if(strncmp(tmp0,"(xy/key/label",14)==0) {
        j=0;
        data_flag=1;
        continue;
    }
}

```

```

if(strcmp(tmp0,"")!=0) {
    //np[i]=j;
    i++;
    data_flag=0;
    continue;
}
if(data_flag==1) {
    if(j==0) sscanf(tmp0,"%*f %f",&sy0[i]);
    //sscanf(tmp0,"%f %f",&data[i][0][j],&data[i][1][j]);
    j++;
}
}
fclose(fin);
//=====
=====

```

end

```

//===== test the read data =====
//for(i=0;i<nl;i++) {
    //fprintf(fp0,"===== particle-%d, np=%d v0=%f\n",i+1,np[i],v0[i]);
    //for(j=0;j<np[i];j++) {
        //fprintf(fp0,"%f %f\n",data[i][0][j],data[i][1][j]);
    //}
    //fprintf(fp0,"=====\n");
//}
//=====
=====

```

end

```

//===== calculate data =====
// --- scale the data: transform the unit of stress Pa into dyn/cm^2. (don't need to scale
for method_4)
//for(i=0;i<nl;i++) {
// for(j=0;j<np[i];j++) {
// // compute the stress from the strain rate and scale it into dyn/cm^2.
// //data[i][1][j]=MIU*data[i][1][j]*10;
// // only scale the stress into dyn/cm^2.
// data[i][1][j]=data[i][1][j]*10;
//}
//}

// --- exchange the time sequence of points on each line (because the stream line is
created reversely).
for(i=0;i<nl;i++) {
    for(j=0;j<np[i];j++) {
        data[i][0][j]=data[i][0][np[i]-1]-data[i][0][j];
    }
}

```



```

}
}

//sm_flag=1; // 1-matlab; 0-simple method
// --- smooth the data to eliminate the numerical noise.
/** --- smooth with MATLAB
if (sm_flag==1) {
// open the MATLAB Engine
if (!(ep=engOpen("\0"))) {
fprintf(stderr, "\nCan't start MATLAB engine\n");
return EXIT_FAILURE;
}
for(i=0;i<nl;i++) {
//for(i=0;i<1;i++) {
tin=mxCreateNumericMatrix(np[i],2,class,mxREAL);
tout=mxCreateNumericMatrix(np[i],2,class,mxREAL);
tout_2p=mxCreateNumericMatrix(np[i],1,class,mxREAL);
tin_pr=calloc(2*np[i],sizeof(double));
tout_pr=calloc(2*np[i],sizeof(double));
tout_2p_pr=calloc(np[i],sizeof(double));
for(j=0;j<np[i];j++) {
tin_pr[j]=data[i][0][j];
}
for(j=0;j<np[i];j++) {
tin_pr[j+np[i]]=data[i][1][j];
}

memcpy(mxGetPr(tin),tin_pr,2*np[i]*sizeof(double));
engPutVariable(ep, "TIN", tin);
//engEvalString(ep, "figure;");
///engEvalString(ep, "subplot(2,1,1);");
//engEvalString(ep, "plot(TIN(:,1),TIN(:,2));");

//// --- simple iteration smooth method
//// --- smooth the stresses: m manipulate the times of smooth
//for(m=1;m<=40;m++) {
//for(j=1;j<np[i];j++) {
//data[i][1][j]=(data[i][1][j-1]+data[i][1][j+1])/2;
//}
//}

//for(j=0;j<np[i];j++) {
//tin_pr[j]=data[i][0][j];
//}

//for(j=0;j<np[i];j++) {
//tin_pr[j+np[i]]=data[i][1][j];
//}

//memcpy(mxGetPr(tin),tin_pr,2*np[i]*sizeof(double));

```

```

//engPutVariable(ep,"TIN_",tin);
//engEvalString(ep,"figure;");
////engEvalString(ep,"subplot(2,1,2);");
//engEvalString(ep,"plot(TIN_(:,1),TIN_(:,2));");

// --- smooth with Gaussian 6
engEvalString(ep,"TON=fit(TIN(:,1),TIN(:,2),'gauss6');");
engEvalString(ep,"TIN_2p=feval(TON,TIN(:,1));");
//engEvalString(ep,"figure;");
//engEvalString(ep,"plot(TIN(:,1),TIN_2p);");
////engEvalString(ep,"cftool(TIN(:,1),TIN(:,2));");

tout_2p=engGetVariable(ep,"TIN_2p");
//tout=engGetVariable(ep,"TIN");

engEvalString(ep,"close all;");
//engEvalString(ep,"clear TIN;");
engEvalString(ep,"clear;");
memcpy(tout_2p_pr,mxGetPr(tout_2p),np[i]*sizeof(double));
//memcpy(tout_pr,mxGetPr(tout),2*np[i]*sizeof(double));
//for(j=0;j<np[i];j++) {
//fprintf(fp0,"%f, %f\n",tout_pr[j],tout_pr[j+np[i]]);
//data[i][0][j]=tout_pr[j];
//}
//for(j=0;j<np[i];j++) {
//data[i][1][j]=tout_pr[j+np[i]];
//}
for(j=0;j<np[i];j++) {
data[i][1][j]=tout_2p_pr[j];
}

free(tin_pr);
free(tout_pr);
free(tout_2p_pr);

mxDestroyArray(tin);
mxDestroyArray(tout);
mxDestroyArray(tout_2p);

printf("\nStream Line %d was done!",i+1);
}

engClose(ep);
} */

// --- smooth with simple method

```

```

if (sm_flag==0) {
  for(m=1;m<=40;m++) {
    for(i=0;i<nl;i++) {
      for(j=1;j<np[i];j++) {
        data[i][1][j]=(data[i][1][j-1]+data[i][1][j+1])/2;
      }
    }
  }
}
//=====

```

```

printf("Outputing data files: \"strf3dn.dat\" and \"strf3dn_v.dat\" and
\"strf3dn_s.dat\" : ... \n");

```

```

//===== write result to file =====
// --- write data as tecplot format
fprintf(fou,"TITLE=\"Multi-Zone XY Plot\"\n");
fprintf(fou,"VARIABLES=\"Time\", \"Von Mises Stresses\"\n");
for(i=0;i<nl;i++) {
  fprintf(fou,"ZONE T=\"Particle-%d\", I=%d\n",i+1,np[i]);
  for(j=0;j<np[i];j++) {
    fprintf(fou,"%f %f\n",data[i][0][j],data[i][1][j]);
  }
  fprintf(fou,"\n");
}
//=====

```

```

//== save velocity magnitude of release plane of the stream lines==
fprintf(fou1,"TITLE=\"Velocity Magnitude of Realease Point\"\n");
fprintf(fou1,"VARIABLES=\"Particle ID\", \"Velocity Magnitude\"\n");
fprintf(fou1,"ZONE I=%d\n",nl);
for(i=0;i<nl;i++) {
  fprintf(fou1,"%d %f\n",i+1,v0[i]);
}
fprintf(fou1,"\n");
//=====

```

```

sumsy=0.0;
for(i=0;i<nl;i++) {
  sumsy=sumsy+sy0[i];
}

```

```

fprintf(fp0,"sumsy=%e\n",sumsy);

//=== save Y face area of cell of release plane of the stream lines===
fprintf(fou2,"TITLE=\"Y-face area ratio of cell of Release Point\"\n");
fprintf(fou2,"VARIABLES=\"Particle ID\", \"Y-face Area\"\n");
fprintf(fou2,"ZONE I=%d\n",nl);
for(i=0;i<nl;i++) {
    //fprintf(fou2,"%d %e\n",i+1,sy0[i]);
    fprintf(fou2,"%d %e\n",i+1,sy0[i]/sumsy);
}
fprintf(fou2,"\n");
//=====
=====

```

end

```

fclose(fou);
fclose(fou1);
fclose(fou2);
fclose(fp0);

printf("Done!\n");

return 0;
}

```

Input file:

c1_path(tao-von_time).dat
c1_path(velocity_time).dat
c1_path(area_time).dat

“*dp_str_hemo.c*”: be used to implement the blood damage models to predict percentage of hemolysis from processed data files provided by *dp_str_data.c*.

// the stream line is created reversely, i.e. form the outflow to upward

```

#include <stdio.h>
#include <math.h>
#include <string.h>
#include <time.h>

```

```

#include "engine.h" // calling MATLAB from a C with MATLAB Engine.
#include "matrix.h" // calling MATLAB from a C with MATLAB Engine.

// LINBUF is the maximum number of characters in single line
#define LINBUF 400

//// NL is the maximum number of lines
#define NL 80000

// TAO_CRIT is the critical stress value which is related to the hemolysis (dyn/cm^2)
#define TAO_CRIT 1500.0

// MIU is the coefficient of viscosity (saline water) (unit: kg/m/s=Pa.s)
#define MIU 0.0035105

int main(int argc, char *argv[])
{
    double tube_stress(float vavg, float v0, float * p_tao_wall);
    double tube_time(float v0);

    double Model_0(float sum_dtime, float tao_avg);
    double Chen(float sum_dtime, float tao_avg, double * p_tao_pre);
    double Song_derv(float dtime, float tao);
    double Rand(float sum_dtime, float tao_avg, double * p_tao_pre);
    double Rand_imp(float S_Sc, float sum_dtime, float dtime, float tao, float d_tao);

    //----- define variables for read data

    float *data[NL][2]; // 0: X axis
                        // 1: Y axis
    float *tmp_data[NL][2];

    // v0: the velocity magnitude in the release plane of the stream lines
    // sy0: the Y-face area of cell in the release plane of the stream lines
    // sumsy: the sum of Y-face area of cell in the release plane of the stream lines
    float v0[NL],sy0[NL];
    double sumsy;

    FILE *fin, *fp0, *fp1;
    char argv1[LINBUF],argv2[LINBUF],argv3[LINBUF];

    int i,j,k,t0;
    char tmp0[LINBUF],tmp1[LINBUF];

    // nl the the total number of lines

```

```

int nl=0;

// np[] the the total number of point for each line
int np[NL];

// flag for each data block
int data_flag=0;          // 0: non data; 1:data

// tao_crit is the critical stress value which is related to the hemolysis
float tao_crit=TAO_CRIT;

// n_hemo is the number of lines which have hemolysis
int n_hemo=0;

// model is to identify different hemolysis models
int model;

double tao_pre;

double sum_f;
float dtime,tao,dtao,d_tao,tmp_sum_f;
    // d_dt_tao is the derivative of tao about time t, d_tao=d_dt_tao*dtime
float per,vmax,vavg,vsum,syvsum,max_time,min_time;
    // per is the percentage of lines occurred hemolysis
    // vmax is the maximum release velocity of all streamlines
    // vavg is the average release velocity of all streamlines
    // vsum is the sum of velocity of each release point
    // syvsum is the sum of Y-face area times velocity of each release point
    // max_time is the maximum exposure time
    // min_time is the minimum exposure time
float sum_tao, sum_dtime, tao_avg, sum_weight, weight;

// values of tube for extended part
float tao_tube, dt_tube, tao_wall;

struct tm* st;
time_t tp;

//===== read data from file =====
fp0=fopen("tmp.dat","w");
fp1=fopen("tmp_1.dat","w");

fin=fopen("input_filename.txt","r");
fscanf(fin,"%s\n",argv1);
fscanf(fin,"%s\n",argv2);
fscanf(fin,"%s\n",argv3);

```

```

//fgets(argv1,LINBUF,fin);
//fgets(argv2,LINBUF,fin);
//fgets(argv3,LINBUF,fin);
//fprintf(fp0,"%s\n",argv1);
//fprintf(fp0,"%s\n",argv2);
//fprintf(fp0,"%s\n",argv3);
fclose(fin);

printf("Processing data files: \"%s\" and \"%s\" and \"%s\" : ... \n",argv1,argv2, argv3);

//fin=fopen("strf3dn.dat","r");
//fin=fopen(argv[1],"r");
fin=fopen(argv1,"r");
i=0;
while(fgets(tmp0,LINBUF,fin)!=NULL) {
    //if(strncmp(tmp0,"ZONE T=",7)==0) {
    if(strncmp(tmp0,"ZONE T=\"Particle-",17)==0) {
        //fprintf(fp0,"%s",tmp0);
        //sscanf(tmp0,"%*17c%*d%*3cI=%d",&np[i]);
        sscanf(tmp0,"%*17c%*d%\"", I=%d",&np[i]);
        //fprintf(fp0,"np[%d]=%d\n",i,np[i]);
        for(k=0;k<2;k++) {
            //data[i][k]=calloc(np[i],sizeof(float));
            data[i][k]=calloc(np[i]+1,sizeof(float));
            tmp_data[i][k]=calloc(np[i]+1,sizeof(float));
        }
        j=0;
        data_flag=1;
        continue;
    }
    if(strncmp(tmp0,"\n",1)==0) {
        //fprintf(fp0,"%s",tmp0);
        i++;
        data_flag=0;
        continue;
    }
    if(data_flag==1) {
        sscanf(tmp0,"%f %f",&data[i][0][j],&data[i][1][j]);
        j++;
    }
}
nl=i;
//fprintf(fp0,"nl=%d\n",nl);

fclose(fin);

```



```

//fin=fopen("strf3dn_v.dat","r");
//fin=fopen(argv[2],"r");
fin=fopen(argv2,"r");
i=0;
while(fgets(tmp0,LINBUF,fin)!=NULL) {
    if(strncmp(tmp0,"ZONE I=",7)==0) {
        //fprintf(fp0,"%s",tmp0);
        j=0;
        data_flag=1;
        continue;
    }
    if(strncmp(tmp0,"\n",1)==0) {
        //fprintf(fp0,"%s",tmp0);
        i++;
        data_flag=0;
        continue;
    }
    if(data_flag==1) {
        //fprintf(fp0,"%s",tmp0);
        sscanf(tmp0,"%*d %f",&v0[j]);
        //fprintf(fp0,"%d %f\n",j,v0[j]);
        j++;
    }
}
fclose(fin);

```

```

//fin=fopen(argv[3],"r");
fin=fopen(argv3,"r");
i=0;
while(fgets(tmp0,LINBUF,fin)!=NULL) {
    if(strncmp(tmp0,"ZONE I=",7)==0) {
        //fprintf(fp0,"%s",tmp0);
        j=0;
        data_flag=1;
        continue;
    }
    if(strncmp(tmp0,"\n",1)==0) {
        //fprintf(fp0,"%s",tmp0);
        i++;
        data_flag=0;
        continue;
    }
    if(data_flag==1) {
        //fprintf(fp0,"%s",tmp0);
        sscanf(tmp0,"%*d %f",&sy0[j]);
        j++;
    }
}

```

```

    //fprintf(fp0,"%d %f\n",j,sy0[j]);
  }
}
fclose(fin);
//=====
//=====

```

end

```

//===== test the read data =====
//for(i=0;i<nl;i++) {
  //fprintf(fp0,"===== particle-%d, np=%d v0=%f\n",i+1,np[i],v0[i]);
  //for(j=0;j<np[i];j++) {
    //fprintf(fp0,"%f %f\n",data[i][0][j],data[i][1][j]);
  //}
  //fprintf(fp0,"=====\n");
//}
//=====
//=====

```

end

```

//for(j=0;j<=np[i]-1;j++) //(0~np[i]-1: total np[i], j=0:exit, j=np[i]-1:entrance)
//===== reverse the sequence =====
//(0~np[i]-1: total np[i], j=0:entrance, j=np[i]-1:exit)
for(i=0;i<nl;i++) {
  for(j=0;j<np[i];j++) {
    tmp_data[i][0][j]=data[i][0][j];
    tmp_data[i][1][j]=data[i][1][j];
  }
}
for(i=0;i<nl;i++) {
  //fprintf(fp0,"===== particle-%d, np=%d v0=%f\n",i+1,np[i],v0[i]);
  for(j=0;j<np[i];j++) {
    data[i][0][j]=tmp_data[i][0][np[i]-1-j];
    data[i][1][j]=tmp_data[i][1][np[i]-1-j];
    //fprintf(fp0,"%f %f\n",data[i][0][j],data[i][1][j]);
  }
  //fprintf(fp0,"=====\n");
}
//=====
//=====

```

end

```

//(0~np[i]-1: total np[i], j=0:entrance, j=np[i]-1:exit)
// np[i]=np[i]+1=>
//(0~np[i]-1: total np[i], j=0:entrance, j=np[i]-2: original exit, j=np[i]-1:extended exit)
//===== add extended part =====
vmax=v0[0]; vavg=0.0; vsum=0.0; sumsy=0.0; syvsum=0.0;

```

```

for(i=0;i<nl;i++) {
  if(v0[i]>vmax) vmax=v0[i];
  vsum=vsum+v0[i];
  sumsy=sumsy+sy0[i];
  syvsum=syvsum+sy0[i]*v0[i];
}
vavg=vsum/nl;
//vavg=syvsum/sumsy;

for(i=0;i<nl;i++) {
  //fprintf(fp0,"===== particle-i=%d, np[i]=%d v0=%f\n",i,np[i],v0[i]);
  // compute the stress from the strain rate and scale it into dyn/cm^2.
  dt_tube=tube_time(v0[i]);
  tao_tube=tube_stress(vavg,v0[i],&tao_wall);
  np[i]=np[i]+1;
  data[i][0][np[i]-1]=data[i][0][np[i]-2]+dt_tube;
  data[i][1][np[i]-1]=data[i][1][np[i]-2];
  //data[i][1][np[i]-1]=2*tao_tube-data[i][1][np[i]-2];
  //fprintf(fp0,"===== particle-i=%d, np[i]-1=%d data[i][0][np[i]-2]=%f
data[i][0][np[i]-1]=%f dt_tube=%f\n",i, np[i]-1,data[i][0][np[i]-2],data[i][0][np[i]-
1],dt_tube);
  //fprintf(fp0,"===== particle-i=%d, np[i]=%d v0=%f data[i][1][np[i]-
2]=%f data[i][1][np[i]-1]=%f tao_tube=%f \n",i,np[i],v0[i],data[i][1][np[i]-2],
data[i][1][np[i]-1],tao_tube);
  //fprintf(fp0,"===== \n");
  //fprintf(fp0,"===== particle-i=%d, np[i]-1=%d data[i][1][np[i]-2]=%f
data[i][1][np[i]-1]=%f\n",i, np[i]-1,data[i][1][np[i]-2],data[i][1][np[i]-1]);
  //fprintf(fp0,"===== particle-i=%d, np[i]-1=%d data[i][0][np[i]-1]=%f
data[i][1][np[i]-1]=%f\n",i, np[i]-1,data[i][0][np[i]-1],data[i][1][np[i]-1]);
}
//=====
//=====

```

end

```
printf("Outputing data files: \"tmp.dat\" and \"tmp_1.dat\" : ... \n");
```

```
//===== calculate the number of lines which hemolysis occurs =====
```

```
// assign the model number
```

```
// model=0 for hemolysis model -0: empirical model
```

```
// model=1 for hemolysis model -1: chen's model
```

```
// model=2 for hemolysis model -2: Song's model
```

```
// model=3 for hemolysis model -3: Rand's model
```

```
// model=4 for hemolysis model -4: Rand_imp's model
```

```
model=4;
```

```
// unit of data file of von Mises stress is dyn/cm^2, and ahead over by sqrt(3).
```

```

per=0.0;
for(i=0;i<nl;i++) {
  sum_f=0.0;
  sum_tao=0.0; sum_dtime=0.0; sum_weight=0.0;
  tmp_sum_f=0.0;
  for(j=0;j<np[i]-1;j++) { // (0~np[i]-1: total np[i], j=0:entrance, j=np[i]-1:exit)
    dtime=data[i][0][j+1]-data[i][0][j];
    tao=(data[i][1][j+1]+data[i][1][j])/2.0;
    //d_dt_tao=(data[i][1][j+1]-data[i][1][j])/dtime;
    d_tao=data[i][1][j+1]-data[i][1][j];
    //fprintf(fp0,"i=%d j=%d dtime=%f d_tao=%f\n",i,j,dtime,d_tao);
    // dtime=data[i][0][j]-data[i][0][j+1];
    // for non-exchange: dtime=data[i][0][j+1]-data[i][0][j];
    if(dtime<0) fprintf(fp0,"warning: dt is <0! dtime=%f j=%d\n",dtime,j);
    //tao=(data[i][1][j+1]+data[i][1][j])/2.0/sqrt(3); // don't need to divide sqrt(3) for
method_4
    //tao=(data[i][1][j+1]+data[i][1][j])/2.0;
    //fprintf(fp0,"i=%d j=%d dtime=%f tao=%f dtao=%f\n",i,j,dtime,tao,dtao);
    if((model==2)||(model==4)) dtao=tao;
    else dtao=tao-tao_crit;
    if(dtao>0) {
      sum_dtime=sum_dtime+dtime;
      // ??????????
      weight=dtime;
      //weight=pow(dtime,0.5); // not the same as same as weight=dtime;
      sum_tao=sum_tao+tao*weight;
      sum_weight=sum_weight+weight;
    }
    if(model==2) sum_f=sum_f + Song_derv(dtime, tao);
    // tmp_sum_f = S_Sc
    if(model==4) {
      tmp_sum_f=Rand_imp(tmp_sum_f, sum_dtime, dtime, tao, d_tao);
      if(tmp_sum_f>=1.0) sum_f=1.0; // or break; ( then, sum_dtime may shorter)
      //sum_f=tmp_sum_f;
    }
  }
  //fprintf(fp0,"i=%d j=%d sum_dtime=%f\n",i,j,sum_dtime);
  if(i>0) {
    if(sum_dtime>max_time) max_time=sum_dtime;
    if(sum_dtime<min_time) min_time=sum_dtime;
  }
  else {
    max_time=sum_dtime;
    min_time=sum_dtime;
  }
  if(sum_weight>0) tao_avg=sum_tao/sum_weight;

```

```

else tao_avg=0.0;
if(sum_dtime<1e-8) continue; // to avoid divided by zero.

// model=0, empirical
if(model==0) sum_f=Model_0(sum_dtime, tao_avg);

// model=1, chen's model
if(model==1) sum_f=Chen(sum_dtime, tao_avg, &tao_pre);

// model=2, Song's model
//if(model==2) sum_f=sum_f;

// model=3, Rand's model
if(model==3) sum_f=Rand(sum_dtime, tao_avg, &tao_pre);

// model=4, Rand_imp's model
//if(model==4) sum_f=Rand_imp(sum_dtime, tao_avg, &tao_pre);

// model=5, Sharp's model
if(model==5) {
    //sum_f=(tao_avg-tao_crit)*pow(sum_dtime,0.25);
    //if(sum_f>=60.4e-2) hemo_flag=1;
}

if(sum_f>=(1.0-1e-6)) n_hemo++;
//if(abs(sum_f-1.0)<1e-6) n_hemo++;
per=per+sum_f*v0[i]/vsum;
//per=per+sy0[i]*v0[i]/syvsum;
//fprintf(fp1,"line          %d,          sum_f=%f,          tao_avg=%f,
sum_time=%f\n",i+1,sum_f,tao_avg,sum_dtime);

    fprintf(fp1,"line %d, sum_time=%f, tao_pre=%f, tao_avg=%f, shear_rate=%f,
sum_f=%f,          v0[i]=%f,          tao_tube=%f,
dt_tube=%f\n",i+1,sum_dtime,tao_pre,tao_avg,tao_avg/10.0/MIU,sum_f,v0[i],tao_tube,d
t_tube);
    //fprintf(fp1,"%f\n",tao_pre);
}

//fprintf(fp0,"\n\n\n");
fprintf(fp1,"\n\n min_time=%f, max_time=%f, sumsy=%f, vavg=%f, vmax=%f,
tao_wall=%f\n",min_time,max_time,sumsy,vavg,vmax,tao_wall);

time(&tp);
st=localtime(&tp);
//fprintf(fp0,"Processing data file: \"%s\" and \"%s\" and \"%s\", \nat time: %d:%d:%d,
%d/%d/%d\n",argv[1],argv[2], argv[3],

```

```

fprintf(fp0,"Processing data file: \"%s\" and \"%s\" and \"%s\", \nat time: %d:%d:%d,
%d/%d/%d \n",argv1,argv2, argv3,
    st->tm_hour,st->tm_min,st->tm_sec,st->tm_mon+1,st->tm_mday,(st->tm_year-
100)+2000);
fprintf(fp0,"number of lines which have hemolysis n_hemo =%d\n",n_hemo);
fprintf(fp0,"number of total lines nl =%d\n",nl);
fprintf(fp0,"percentage of lines which have hemolysis =%f\n",per*100.0);
//=====
=====

```

end

```

fclose(fp0);
fclose(fp1);

printf("Done!\n");

return 0;
}

```

```

// full developed tube flow, (shear stress=von Mises stress/sqrt(3), dyn/cm^2).
double tube_stress(float vavg, float v0, float * p_tao_wall) {
    // shear stress on the wall
    float tao_wall, tao;
    // radius of tube (m)
    float rad=1.2192e-3/2.0;

    tao_wall=4*MIU/rad*vavg;
    // convert N/m^2 into dyn/cm^2
    tao_wall=10*tao_wall;
    *p_tao_wall=tao_wall;
    tao=tao_wall*sqrt(1-v0/(2*vavg));

    return tao;
}

```

```

// full developed tube flow, duration of flow.
double tube_time(float v0) {
    double travel_time;
    // length of tube (m) (1.779"=45.187mm, need to deduct the part of simulated, which is
25.4mm-0.5228mm)
    //float Len=35.71e-3;
    float Len=20.31e-3;

```

```

travel_time=Len/v0;

return travel_time;
}

// model=0, empirical
double Model_0(float sum_dtime, float tao_avg) {
    double hemo_flag=0;
    // for empirical model

    //if((sum_dtime<1e-6)&&(tao_avg>100000)) hemo_flag=1;
    //if((sum_dtime>=1e-6)&&(sum_dtime<1e-5)&&(tao_avg>40000)) hemo_flag=1;
    //if((sum_dtime>=1e-5)&&(sum_dtime<1e-4)&&(tao_avg>6000)) hemo_flag=1;
    //if((sum_dtime>=1e-4)&&(sum_dtime<1e-3)&&(tao_avg>4500)) hemo_flag=1;
    //if((sum_dtime>=1e-3)&&(sum_dtime<1e-1)&&(tao_avg>4000)) hemo_flag=1;
    //if((sum_dtime>=1e-1)&&(sum_dtime<1)&&(tao_avg>3500)) hemo_flag=1;
    //if((sum_dtime>=1)&&(sum_dtime<100)&&(tao_avg>2500)) hemo_flag=1;
    //if((sum_dtime>=100)&&(tao_avg>1500)) hemo_flag=1;

    if((sum_dtime>=1e-6)&&(sum_dtime<1e-5)&&(tao_avg>100000)) hemo_flag=1;
    if((sum_dtime>=1e-5)&&(sum_dtime<1e-4)&&(tao_avg>40000)) hemo_flag=1;
    if((sum_dtime>=1e-4)&&(sum_dtime<1e-3)&&(tao_avg>9000)) hemo_flag=1;
    //if((sum_dtime>=1e-4)&&(sum_dtime<1e-3)&&(tao_avg>6000)) hemo_flag=1;
    //if((sum_dtime>=1e-3)&&(sum_dtime<1e-2)&&(tao_avg>4500)) hemo_flag=1;
    //if((sum_dtime>=1e-3)&&(sum_dtime<1e-2)&&(tao_avg>6000)) hemo_flag=1;
    if((sum_dtime>=1e-3)&&(sum_dtime<1e-2)&&(tao_avg>8000)) hemo_flag=1;
    if((sum_dtime>=1e-2)&&(sum_dtime<1e-1)&&(tao_avg>7000)) hemo_flag=1;
    //if((sum_dtime>=1e-2)&&(sum_dtime<1e-1)&&(tao_avg>4500)) hemo_flag=1;
    //if((sum_dtime>=1e-2)&&(sum_dtime<1e-1)&&(tao_avg>4000)) hemo_flag=1;
    //if((sum_dtime>=1e-1)&&(sum_dtime<1)&&(tao_avg>3500)) hemo_flag=1;
    if((sum_dtime>=1e-1)&&(sum_dtime<1)&&(tao_avg>5000)) hemo_flag=1;
    //if((sum_dtime>=1)&&(sum_dtime<100)&&(tao_avg>2500)) hemo_flag=1;
    if((sum_dtime>=1)&&(sum_dtime<100)&&(tao_avg>3000)) hemo_flag=1;
    if((sum_dtime>=100)&&(tao_avg>1500)) hemo_flag=1;

    return hemo_flag;
}

// model=1, chen's model
double Chen(float sum_dtime, float tao_avg, double * p_tao_pre) {
    double hemo_flag=0;
    // for Chen's model
    double Es, eta, c, dA_A, alpha;

```



```

// for method 1
///eta=2.4e-3;
//eta=1.2e-3;
//alpha=0.5;

// for method 3
//eta=1.0e-3;
//alpha=0.25;

Es=1.2e-3;
eta=1.0e-3;
alpha=0.25;

//Es=1.2e-3;
//eta=1.0e-3;
//alpha=0.3;

//Es=1.0e-3;
c=1.71e-6;
dA_A=0.06;

*p_tao_pre=10*dA_A*3/c*(Es+eta/pow(sum_dtime,alpha));

// either comment or not, no effect on final results
//if(sum_dtime>=1e-4)
  if(tao_avg>(*p_tao_pre)) hemo_flag=1;
//if((sum_dtime>=1e-6)&&(sum_dtime<1e-5)&&(tao_avg>100000)) hemo_flag=1;
//if((sum_dtime>=1e-5)&&(sum_dtime<1e-4)&&(tao_avg>40000)) hemo_flag=1;

return hemo_flag;
}

// model=2, Song's model
double Song_derv(float dtime, float tao) {
  double f=0.0;

  // D1-Giersiepen model
  //f=3.62e-5*pow(tao/10,2.416)*pow(dtime,0.785); // convert the unit of stress
  dyn/cm^2 into Pa
  // D2-Heuser model
  f=1.8e-6*pow(tao/10,1.991)*pow(dtime,0.765); // convert the unit of stress dyn/cm^2
  into Pa

  return f;
}

```

```

// model=3, Rand's model
double Rand(float sum_dtime, float tao_avg, double * p_tao_pre) {
    double hemo_flag=0;
    // for Rand's model
    double C1=3.5e-2, C2=3.9e-2, C3=8.0, C4=1.5e-4, temp0, Tc, b=1.8e-4, alpha;

    // t=10ms, Tao_c = 4000
    alpha=45.69;
    //alpha=40.61;

    // t=240, Tao_c = 3500 --- too big.
    //alpha=18.04;

    // unit of tao_pre is dyn/cm^2
    temp0=C1+C2*(1.0-exp(-1.0*C3*sum_dtime))+C4*sum_dtime;
    Tc=1.0/temp0;
    *p_tao_pre=Tc/(alpha*4.0/5.0*b);
    // apply regression model
    //if((sum_dtime>=10e-3)&&(sum_dtime<20e-3))
    // *p_tao_pre=(4.7-1.703-0.00599*sum_dtime*1000)/0.000734;

    // either comment or not, no effect on final results
    //if(sum_dtime>=1e-3)
        if(tao_avg>(*p_tao_pre)) hemo_flag=1;
        //if(tao_avg>(*p_tao_pre)) hemo_flag=1;
        //else hemo_flag=tao_avg/(*p_tao_pre);
    //if((sum_dtime>=1e-6)&&(sum_dtime<1e-5)&&(tao_avg>100000)) hemo_flag=1;
    //if((sum_dtime>=1e-5)&&(sum_dtime<1e-4)&&(tao_avg>40000)) hemo_flag=1;
    //if((sum_dtime>=1e-4)&&(sum_dtime<1e-3)&&(tao_avg>5600)) hemo_flag=1;

    return hemo_flag;
}

// model=4, Rand_imp's model
double Rand_imp(float pre_S_Sc, float sum_dtime, float dtime, float tao, float d_tao) {

    double Rand_derv(float pre_S_Sc, float sum_dtime, float dtime, float tao, float d_tao);
    //double hemo_flag=0;
    double next_S_Sc;
    // for Rand's model
    // critical strain
    //double Sc=0.06;

```

```

double d_S_Sc;

d_S_Sc=Rand_derv(pre_S_Sc, sum_dtime, dtime, tao, d_tao);
next_S_Sc=pre_S_Sc+d_S_Sc;

if(next_S_Sc<0.0) next_S_Sc=0.0;
//if(S_Sc>=1.0) hemo_flag=1;

//return hemo_flag;
return next_S_Sc;
}

double Rand_derv(float pre_S_Sc, float sum_dtime, float dtime, float tao, float d_tao) {
// for original Rand's model
//double C0=3.5e-2, C1=3.9e-2, C2=8.0, C3=1.5e-4, b=1.8e-4, alpha;
// for tried Rand's model
//double C0=2.5e-2, C1=3.9e-2, C2=40, C3=1.5e-4, b=1.8e-4, alpha;
// for tried Rand's model (with tao_e)
//double C0=3.5e-2, C1=3.9e-2, C2=40, C3=1.5e-4, b=1.8e-4, alpha;
//double tao_e=750; //750 dyn/cm^2
// for optimized Rand's model (with tao_e)
double C0=3.5e-2, C1=3.9e-2, C2=84, C3=1.5e-4, b=1.5e-4, alpha;
double tao_e=1200; //1200 dyn/cm^2
//double C0=8.68e-2, C1=3.9e-2, C2=39, C3=1.5e-4, b=1.8e-4, alpha;
//double tao_e=2130;
// for new reg
//double C0=3.5e-2, C1=5.9e-1, C2=8.0, C3=1.5e-4, b=1.8e-4, alpha, C4=2.5e3,
C5=6.90;
// T: tension force (dyn/cm)
double T;
//double a_at_T, a_at_S_Sc, d_dt_S_Sc, temp0;
double d_T, a_at_S_Sc, temp0, temp1, add_term, a_at_temp0, a_at_temp1,
a_at_add_term;
double d_S_Sc; // d_S_Sc=d_dt_S_Sc*dtime
double S_Sc; // S_Sc (S/Sc)

// t=10ms, Tao_c = 4000
//alpha=45.69;
alpha=39.01;

// unit of tao is dyn/cm^2
// sum_dtime = t
//T=(alpha*4.0/5.0*b)*tao;
// apply b=b(S/Sc) from V=98um^3, A=130um^2
//b=-0.125*S_Sc+1.829;
//b=b*1e-4; // convert um into m

```

```

T=(alpha*4.0/5.0*b)*(tao-tao_e);

temp0=C0+C1*(1.0-exp(-1.0*C2*sum_dtime))+C3*sum_dtime; // original formula
//temp1=1.0/(1.0/temp0+1.0/(C4*sum_dtime)+C5); // new regression formula
//add_term=-1.2e-2/pow(sum_dtime,2);
add_term=0;
temp1=temp0+add_term; // new try formula

//S_Sc=alpha*4.0/5.0*b*tao*temp1; // new formula (for refernce only, not actually use)
//d_S_Sc=S_Sc-pre_S_Sc; // not good

d_T=(alpha*4.0/5.0*b)*d_tao;
a_at_temp0=C1*C2*exp(-1.0*C2*sum_dtime)+C3;
//a_at_temp1=(a_at_temp0/pow(temp0,2)+1.0/(C4*pow(sum_dtime,2)))/pow(temp1,2);
// new regression formula
//a_at_add_term=2.4e-2/pow(sum_dtime,3);
a_at_add_term=0;
a_at_temp1=a_at_temp0+a_at_add_term; // new try formula
a_at_S_Sc=T*a_at_temp1; // derive for new regression formula
//d_S_Sc=temp0*d_T+a_at_S_Sc*dtime;
d_S_Sc=temp1*d_T+a_at_S_Sc*dtime;

return d_S_Sc;
}

//a_at_T=(alpha*4.0/5.0*b)*d_dt_tao;
//d_T=a_at_T*dtime; // d_tao=d_dt_tao*dtime

// a_at_S_Sc=T*a_at_temp0; // derive for original formula
//d_dt_S_Sc=temp0*a_at_T+a_at_S_Sc;
//d_S_Sc=d_dt_S_Sc*dtime;

```

Input file:

strf3dn_c1.dat
strf3dn_v_c1.dat
strf3dn_s_c1.dat

CURRICULUM VITAE

NAME: Yangsheng Chen

ADDRESS: Department of Mechanical Engineering
University of Louisville
Louisville, KY 40292

DOB: Hubei, P. R. China - May 20, 1969

EDUCATION & TRAINING:

B.S., Mechanics
University of Science and Technology of China
1987-1992

M.Eng., Mechanical Engineering
China Aerodynamics Research and Development Center
1992-1995

M.S., Computer Science
University of Louisville
2001-2003